Micromechanical Modeling of the Toughening Mechanisms in Particle-Modified Semicrystalline Polymers
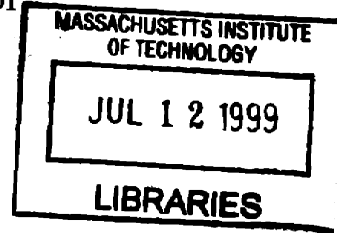
by

Panagiota A. Tzika

Submitted to the Department of Mechanical Engineering
in partial fulfillment of the requirements for the degree of

Master of Science in Mechanical Engineering

at the

MASSACHUSETTS INSTITUTE OF TECHNOLOGY

May 1999

© Massachusetts Institute of Technology 1999. All rights reserved.

Author . . . .
Department of Mechanical Engineering
May, 1999

Certified by. . . . .
Mary C. Boyce
Professor
Thesis Supervisor

Certified by. . . . .
David M. Parks
Professor
Thesis Supervisor

Accepted by . . . .
Professor Ain A. Sonin, Chairman
Departmental Committee on Graduate Students

Micromechanical Modeling of the Toughening Mechanisms in Particle-Modified Semicrystalline Polymers

by

Panagiota A. Tzika

Abstract

It is now well appreciated that a number of semicrystalline polymers can be effectively toughened by the addition of a well-dispersed secondary phase. In particular, when the average interparticle matrix ligament thickness, Λ, of the blend is reduced below a critical length parameter, Λ_c, dramatic jumps in toughness levels are observed. This critical parameter is a specific material characteristic of the base polymer and can be achieved by various combinations of filler particle volume fraction and particle size. Recently, the significant improvements in toughness achieved when $\Lambda \leq \Lambda_c$ were attributed to a morphological transition taking place when interface-induced crystallization of characteristic thickness, $\Lambda_c/2$, successfully percolates through the primary phase. These transcrystallized layers are highly anisotropic in their mechanical response and, as a result, change the preferred modes of plastic deformation in the material, enabling the large plastic strains, which provide the high toughness. This study aims to elucidate the micromechanics and micromechanisms responsible for the high toughness exhibited by these morphologically altered heterogeneous material systems via a series of micromechanical models. The case of polyamide-6 modified with spherical elastomeric particles was modeled. The finite element method was employed to conduct a parametric study on the deformation of these systems. It was found that the mechanical response and local modes of plastic deformation of rubber-modified polyamide-6 depend strongly on the assumed particle distribution, the morphology of the primary phase, the volume fraction of filler particles and the level of applied stress triaxiality. In particular it is shown, that in the case where transcrystallized material spans the interparticle ligaments, the unique morphology of the matrix impedes dilatational expansion of the material, while promoting extensive yielding under conditions of global stress triaxiality. Concluding, an important toughening mechanism is identified.

Thesis Supervisor: David M. Parks
Title: Professor

Acknowledgments

Contents

List of Figures

10

List of Tables

Chapter 1

Introduction

Polyamides (PAs), commonly referred to as nylons [1], are important engineering thermoplastics. While first introduced in 1938 in fibrous form as monofilament bristles and textile yarns, their range of applications has expanded considerably since that time. In addition to fibers, they can now be found in the form of films, extrusions, moldings, castings and modifiers in a variety of different applications, such as automotive and structural. Ease of processing, abrasion and wear resistance, cost and weight reduction, are some of the advantages PAs have to offer in engineering applications. Their limitations lie primarily in their mechanical properties and, in particular, in their well-known sensitivity to stress triaxiality or notch brittleness. Notch brittleness is the condition whereby the material exhibits brittle failure in regions of a structure containing sudden geometry changes that raise the local stress triaxiality (i.e. notches, sharp corners). Clearly, this is an important limiting condition and, as a result, much academic and industrial research has gone into designing materials with enhanced resistance to stress triaxiality.

A commonly-employed practice in designing such materials is blending with a well-dispersed rubbery phase. When properly controlled, this secondary phase may impart significant levels of toughness to the base polymer even in the presence of high triaxiality. For instance, the addition of 20 wt. % rubber in PA-6,6 increases

---

[1] Registered trademark of du Pont.

12
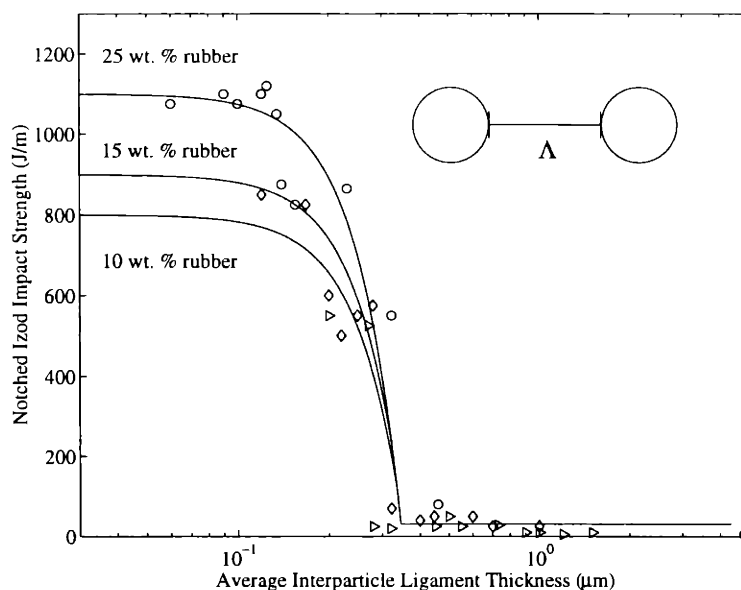
Figure 1-1: Notched Izod impact strength of PA-6,6/rubber blends vs. average inter-particle matrix ligament thickness, Λ (data after Wu (1985)).

its notched Izod strength 30-fold when the particle size is properly controlled (Wu, 1985). Although the effectiveness of these blending practices has been recognized for quite a long time, it wasn't until recently that a toughening criterion became available for semicrystalline polymers. Namely, in 1985 Wu was able to show that the brittle/tough transition in rubber-modified PA-6,6 strongly correlates with the average interparticle matrix ligament thickness, Λ, of the blend. The effect of this length parameter in PA-6,6/rubber blends is illustrated in Fig. 1, where a dramatic jump in toughness is shown to take place when Λ is reduced below a critical value, $\Lambda_c \approx 0.3\,\mu\text{m}$, independently of rubber volume fraction and particle size. Following Wu, a number of investigators verified his observations regarding the existence of Λ_c and extended them to a number of different systems where a semicrystalline polymer comprises the primary phase. Thus, Borggreve et al. (1987) studied PA-6/EPDM rubber blends and concluded that the critical length parameter determined by Wu is indeed the controlling parameter in the toughening of these systems, while Wu et al. (1991) reported similar findings for isotactic polypropylene (iPP). More recently,

Bartczak and co-workers showed that high density polyethylene (HDPE) is effectively toughened by the dispersion of either rubber or calcium carbonate ($CaCO_3$) particles (Bartczak et al., 1999a; Bartczak et al., 1999b). In the Bartczak studies, the authors measured Λ_c to be equal to 0.6 μm for HDPE, demonstrating further that Λ_c is a specific material property of the matrix and does not depend on the nature of the modifying particles. Concluding, it is becoming apparent that Λ_c is the single controlling parameter that determines the onset of the brittle/tough transition in most semicrystalline polymers. Moreover, it is specific to the base polymer and independent of the nature of filler particles, filler content and particle size.

To explain the existence of Λ_c many investigators offered arguments based on stress-field theories, suggesting that stress-field overlap and/or a transition from locally plane strain to plane stress conditions in the matrix was responsible for the toughness jumps (Wu, 1985; Margolina and Wu, 1988). In addition, several studies attempted to demonstrate these premises in terms of finite element micromechanical models. Thus, Fukui et al. (1991) developed a two-dimensional multi-inclusion model and studied the interaction of closely-spaced octahedral rod inclusions in a body-centered cubic (BCC) type of packing. They attributed particle toughening to massive shear deformation of the matrix resulting from overlapping particle stress-fields. In a similar analysis, Dijkstra and Bolscher (1994) considered the same particle distribution under triaxial loading conditions in order to simulate the state of stress ahead of a crack tip. They, too, attributed toughening to extensive plastic deformation of the matrix triggered by stress-field overlap. While matrix yielding is a significant source of energy dissipation and therefore toughness, the works of Fukui et al. and Dijkstra and Bolscher merely begin to identify critical issues regarding the effect of volume fraction in toughening but are unable to capture the effect of a length scale. In other words, both models and field-notions in general are dimensionless in the sense that the ratio of particle diameter to particle-to-particle ligament thickness used in most cases to characterize the onset of stress-field overlap is dimensionless and as such can not correlate with an absolute physical dimension, such as Λ_c. Instead, the dramatic effect of Λ_c must be a consequence of a specific material characteristic

of the matrix.

Muratoglu et al. (1995a, 1995b), were the first to tie the existence of Λ_c to such a material characteristic. They identified a morphological transition to take place in the matrix material when Λ is reduced below Λ_c. Specifically, they showed that in the proximity of a second phase, only the α crystal form of PA-6 is present (Muratoglu et al., 1995a). This crystal form is characterized by the vertical stacking of planar zig-zags of the macromolecular chain, also known as hydrogen-bonded planes. When near a second phase, these planes are found to preferentially align themselves with the interface (Keller, 1959; Muratoglu et al., 1995a). As a result, the normally spherulitic structure of the bulk polymer is replaced by crystalline lamellae growing parallel to each other and perpendicular to the second phase. This preferred crystallization, also known as transcrystallization (Schonhorn, 1967; Fitchmun and Newman, 1969), does not extend more than a well-defined distance into the primary phase. Muratoglu et al. (1995a) determined that in PA-6 the crystal texture resulting from transcrystallization has a thickness, $\approx \Lambda_c/2$. Since significant improvements in toughness are achieved only when the average thickness of interparticle matrix ligaments becomes smaller than the critical dimension, Λ_c, the authors attributed the observed jumps in toughness to the morphological transition taking place when transcrystallized material spans the interparticle distances and successfully percolates through the matrix. This transition in matrix morphology is schematically depicted in Fig. 1-2 in terms of two blends having the same volume fraction of modifier, one with $\Lambda \gg \Lambda_c$, and one with $\Lambda \le \Lambda_c$ [2].

Muratoglu et al. (1995b) went on to postulate a toughening mechanism, whereby the primary toughening role of the rubber particles is to provide an appropriate density of interfaces for transcrystallization to take place in the matrix material. It is then critical that the particles cavitate, early on in the deformation, to relieve constraints on the deforming matrix. In the resulting cavitated system, the crystalline

---

[2]Several authors before Muratoglu et al. reported morphological differences in the matrix material of brittle and tough blends (Gähde et al., 1977; Flexman, 1979; Chacko et al., 1982). However, Muratoglu et al. were the first to relate them to the mechanical properties of the blends, and in particular, their toughness, in a comprehensive way.
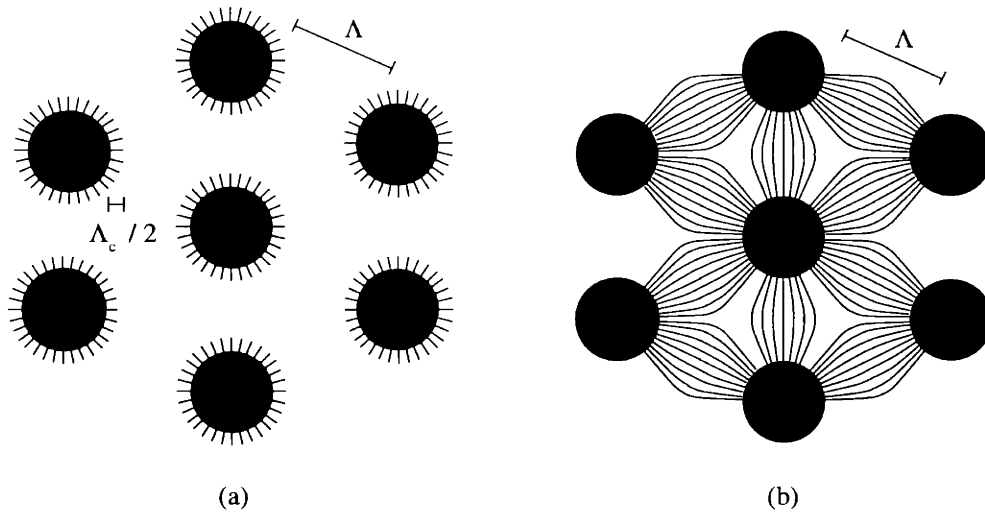
Figure 1-2: Schematic matrix morphology of: (a) brittle blends, $\Lambda \gg \Lambda_c$; (b) tough blends, $\Lambda \leq \Lambda_c$ (projecting lines indicate lamellar growth directions).

component of the PA contains only the α crystal form. In this crystal form, adjacent sheets of folded chains interact with weak van der Waals forces, that readily allow shearing of the crystal along the hydrogen-bonded planes. As a result, chain slip along these planes comprises the deformation mode with the lowest resistance to shear (Lin and Argon, 1992), and consequently, plastic deformation of the material is controlled by the relative orientation of these slip systems with respect to the applied deformation. Specifically, owing to the preferential orientation of the hydrogen-bonded planes parallel to the interface, the sectors of the matrix parallel and perpendicular to the loading direction will resist deformation, while the sectors oriented at roughly 45° will deform readily, facilitating large plastic deformation and toughness. While a combination of different events may ultimately be responsible for the toughness jumps [3], it is the ability of these materials to undergo extensive plastic deformation that provides the toughness. Concluding, this thesis focuses on understanding how the local morphology promotes plastic deformation and toughness.

---

[3]For instance, in addition to providing sites for early yield to take place, the refinement of the local microstructure resulting from transcrystallization acts to eliminate defect structures, such as spherulite boundaries, which promote brittle response under high triaxiality.

Chapter 2

Description of micromechanical models

In order to understand the underlying mechanisms that impart toughness to the unmodified semicrystalline polymer, micromechanical models were constructed that permitted the study of the influence of particle distribution, matrix morphology, volume fraction of modifier and triaxial loading on the composite material behavior. In the sections to follow, these models are discussed in terms of: (1) the geometric description of a Representative Volume Element (RVE), which embodies the microstructure of the model material; (2) the constitutive description of the matrix material behavior as tied to the underlying morphology of the blend modeled; and (3) the description of loading conditions. The case of PA-6 modified with spherical rubber particles is presented. Based on the results of a related study, which demonstrated that the cavitation event itself does not significantly contribute to the toughening of PAs, as long as it occurs sufficiently early on in the deformation (Baumann, 1998), the rubber particles were modeled here to be pre-cavitated (i.e. as voids), and are thus not discussed any further.

2.1 Representative Volume Element (RVE) geometry

The first step in micromechanical modeling is to determine a Representative Volume Element (RVE), which adequately captures essential features of the underlying microstructural geometry and deformation modes. A particle-toughened polymer consists of a well-dispersed but random distribution of a given volume fraction of particles in a matrix. In the case of rubber particles, the particles are nearly spherical, having some distribution in size. In this study, the particles were idealized as being spherical and of equal size. Moreover, two simplified RVE models of polymers filled with: (1) a stacked hexagonal array of particles, to be termed here the Regular Array (RA), and (2) a more realistic Staggered Array (SA) of particles were considered. The RVE models for both particle distributions are mathematically described below, where notation is based on the following conventions. Scalars are in italics (a, A), vectors are in lower-case boldface $(\mathbf{a})$, second-order tensors are in upper-case boldface $(\mathbf{A})$ and macroscopic quantities are in barred characters $(\overline{\mathbf{A}})$. The second-order identity tensor is denoted by $(\mathbf{I})$. Components of tensor and vector quantities are expressed in cylindrical coordinates, where r represents the radial direction, z represents the axial direction and θ represents the circumferential angle. Tensor (dyadic) products are indicated by $(\otimes)$ and tensor scalar products of appropriate order by a raised dot $(\cdot)$.

2.1.1 Regular Array (RA) model

The RA model is a simplified representation of the idealized periodic microstructure depicted in Fig. 2-1; i.e., in 12 and 23-orthographic views of the model material, the second phase particles are arranged in regular arrays, while in the 13-orthographic view they are closely packed. Traditionally, such periodic structure is divided into stacked hexagonal cells, centered on each particle, that behave identically when the system is subjected to far-field normal loads. That is, the lateral faces of each cell remain planar with zero shear traction and average normal stress equal to the macro-

scopically applied transverse stresses, while the top and bottom faces also remain planar with zero shear traction and average normal stress equal to the macroscopically applied axial stress. Since the deformation of each of these cells is identical to that of its neighbors, only one cell, referred to as the Representative Volume Element (RVE) of the model material, needs to be considered, provided that appropriate boundary conditions are specified. To simplify the problem further, the space-filling hexagonal cells are approximated as cylindrically-shaped cells at the appropriate volume fraction. The advantage of the cylinder approximation is that the solution to the deformation problem becomes independent of the circumferential angle, θ, and consequently, only a two-dimensional structure needs to be analyzed. Finally, since the z-plane is a symmetry plane, the region of interest reduces to the hatched region of Fig. 2-1 (d).

In this study, the transverse and axial spacing of voids in the model material was chosen so that the initial radius of the RVE, R_0, was equal to the initial length, L_0 (see Fig. 2-2 (a)). The initial porosity, f_0, was estimated from: $f_0 = 2 R_v^3 / 3 R_0^2 L_0$, where R_v is the initial radius of the void. The two-dimensional domain of interest was discretized using 8-node full-integration quadratic axisymmetric elements, and was deformed subject to periodic boundary conditions embodying compatibility and traction continuity in the model material (see Fig. 2-2 (b)). In particular, the lateral boundary of the RVE was constrained to remain cylindrical during the deformation, while its top and bottom surfaces were constrained to remain planar. These symmetry conditions were enforced in the finite element model via the following constraints:

$$
\begin{aligned}
u_z|_{BC} &= u_z|_B, \\
u_r|_{CD} &= u_r|_D, \\
u_z|_{ED} &= 0, \\
u_r|_{AB} &= 0,
\end{aligned}
\tag{2.1}
$$

where for example, $u_z|_{BC}$ is the displacement in the z-direction of radial segment BC, while $u_z|_B$ is the displacement in the z-direction of point B.
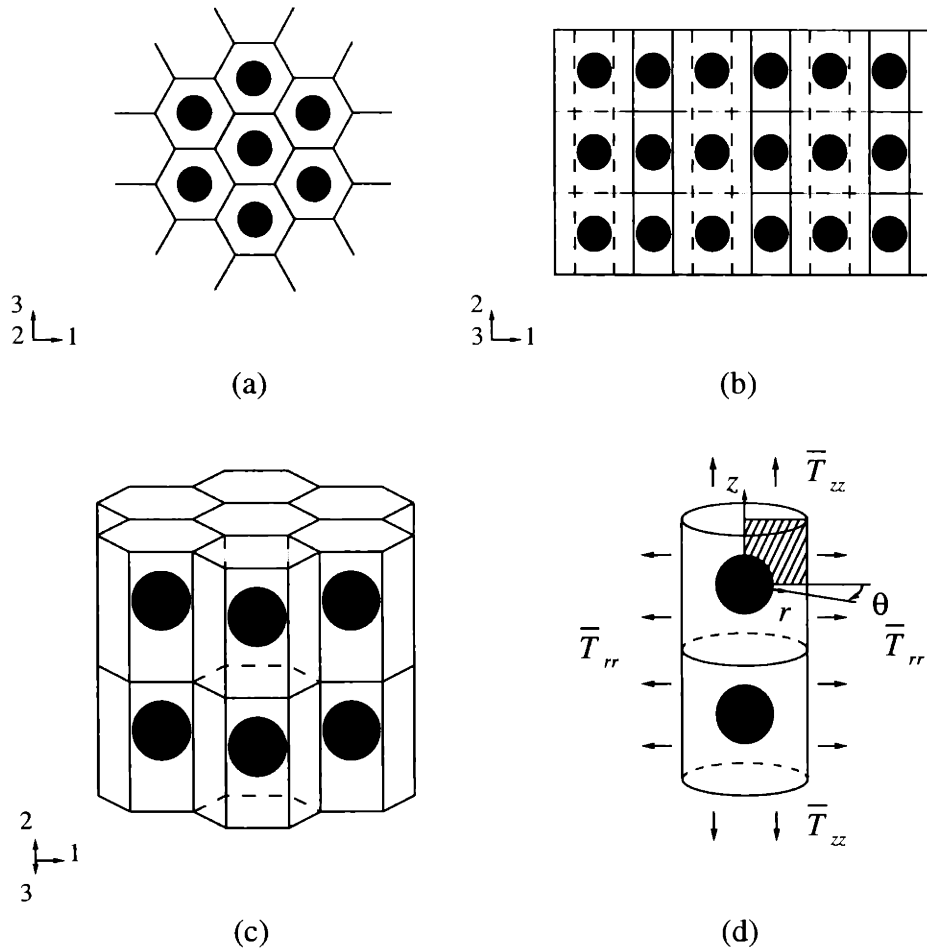
Figure 2-1: Motivation for RA model: (a) 13-orthographic view; (b) 12 and 23-orthographic views; (c) stacked hexagonal RVEs; (d) axisymmetric RVEs.

2.1.2 Staggered Array (SA) model

While RA models have been used extensively in the study of heterogeneous materials (see for example, Tvergaard (1982), Bao et al. (1991), Steenbrink et al. (1997)), they assume a rather unrealistic particle distribution. As a result, desired modes of deformation such as interparticle matrix shear are restricted. Several authors recognized this weakness of the RA model and have proposed alternative micromechanical models of particle-filled materials. Thus, Huang and Kinloch (1992) used a plane strain RVE model of a nested two-dimensional particle distribution and showed that this new model predicted patterns of matrix deformation fundamentally different from the
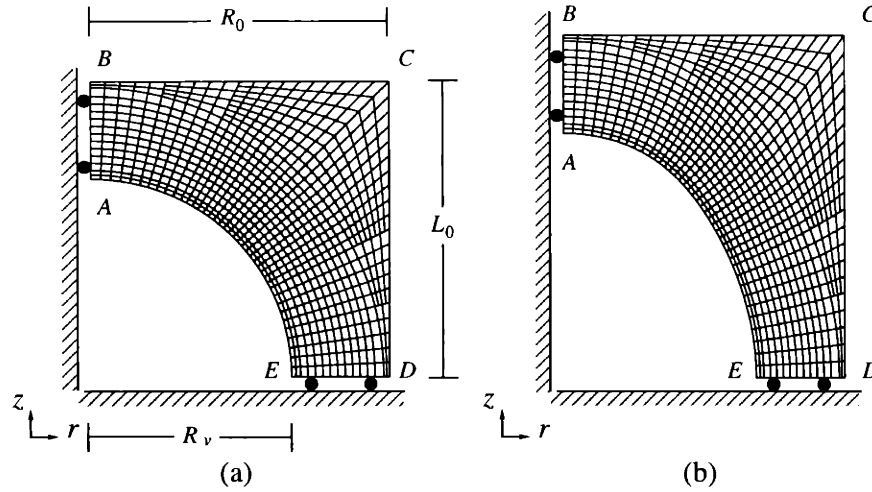
Figure 2-2: Finite element model of RA particle distribution: (a) sample undeformed mesh, $f_0 = 20\%$; (b) sample deformed mesh, $f_0 = 20\%$.

RA approach. In a more detailed study, Smit et al. (1999) considered various random two-dimensional particle distributions, also in terms of plane strain RVE models. They too emphasized the important role of particle distribution in the progression of plastic deformation in heterogeneous material systems. More recently, Socrate and Boyce (1999) modeled a three-dimensional staggered particle distribution using an approach whereby the RVE geometry can be simplified to one similar to that of the RA model. Their model captures the interaction of particles in a more realistic staggered arrangement, while maintaining the axisymmetric simplicity of the RA model. An axisymmetric RVE model of a three-dimensional staggered array of particles (SA model), was also adopted in this study and is briefly discussed below. This model will be shown to be particularly important in the study of this thesis, where special features of the matrix morphology and resulting constitutive behavior promote significant changes in the preferred modes of plastic deformation in the matrix that may be inhibited by the constraints of the more traditional RA model.

The heterogeneous material considered in the SA approach models the periodic distribution of spherical particles shown in Fig. 2-3; i.e., in the 13-orthographic view, the modifying particles form a square array, while in 12 and 23-orthographic views

they are arranged in a staggered fashion. As in Sec. 2.1.1, the assumed periodic microstructure is divided into unit cells that behave identically under macroscopically applied normal loads. In this case, the axisymmetric RVE is introduced as an approximation to the cubic unit cell of Fig. 2-3 [1]. Owing to symmetries similar to the ones considered previously, the axisymmetric SA model is defined on a two-dimensional domain identical to the one analyzed in the RA approach. However, the structure now deforms subject to very different lateral boundary conditions in order to properly capture the influence of neighboring particles. More specifically, since in the SA ap-
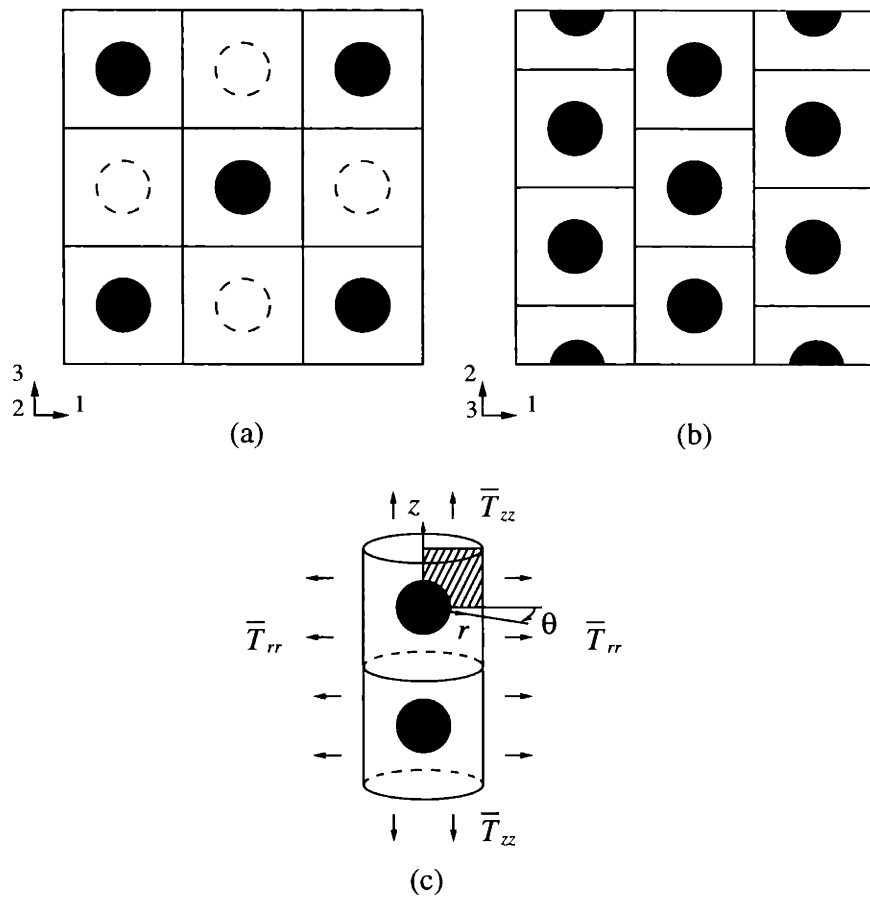
Figure 2-3: Motivation for SA model: (a) 13-orthographic view; (b) 12 and 23-orthographic views; (c) axisymmetric RVEs.

---

[1]Note that the cubic cell used to divide the model material is not the only repetitive cell geometry possible. The effect of using an alternative cell geometry is discussed in the following section.

proach eight nearest neighbors are located diagonally above and below the equator of a particular particle, the lateral boundary of the RVE is expected to curve during the deformation. This special feature of the SA model is more easily understood when the RVE is considered together with a neighboring cell. As shown schematically in Fig. 2-4, such neighboring cell is identical to the RVE analyzed, only rotated by 180°. In this anti-parallel cell arrangement, axial compatibility requires that the top and
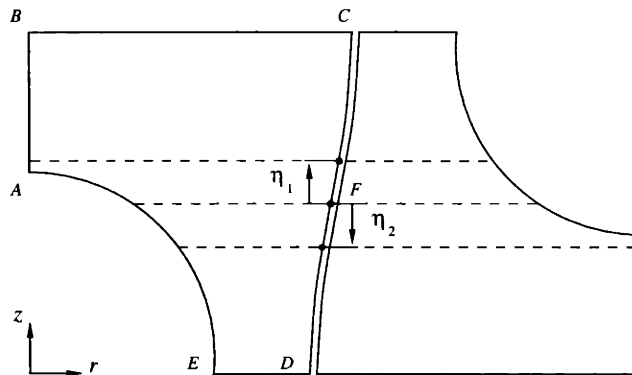
Figure 2-4: Schematic of anti-parallel cell arrangement considered by the SA model.

bottom of the RVE remain planar throughout the deformation. Moreover, points along the lateral boundary move such that,

$$u_z(\eta_1) + u_z(\eta_2) = 2u_z|_F, \text{ for } \eta_1 = \eta_2, \qquad (2.2)$$

where $u_z(\eta_1)$ and $u_z(\eta_2)$ are the displacements in the z-direction of points located axial distances η_1 and η_2 from point F. Point F is the mid-point of the initially straight and axially-oriented boundary CD and moves such that,

$$2u_z|_F = u_z|_B, \qquad (2.3)$$

where $u_z|_B$ is the axial displacement of the top boundary. In addition, radial compatibility requires the total cross-sectional area of an infinite array of cells to be independent of the axial coordinate position. Consequently, the displacement in the radial direction of points along the lateral boundary must satisfy the following con-

23

dition,

$$[R_0 + u_r(\eta_1)]^2 + [R_0 + u_r(\eta_2)]^2 = 2[R_0 + u_r|_F]^2, \text{ for } \eta_1 = \eta_2, \qquad (2.4)$$

where R_0 is the initial radius of the RVE, while $\pi\{[R_0 + u_r(\eta_1)]^2 + [R_0 + u_r(\eta_2)]^2\}$ and $2\pi[R_0 + u_r|_F]^2$ are the cross-sectional areas of two cells at an axial distance η_1 (or η_2) from point F, and at point F, respectively, in the deformed configuration. Finally, symmetry with respect to the z-axis and the z-plane requires that,

$$u_r|_{AB} = 0 \text{ and } u_z|_{DE} = 0. \qquad (2.5)$$

A sample of the discretized structure deformed subject to these special lateral boundary conditions is depicted in Fig.2-5 (b). The user subroutine used to implement these constraints in ABAQUS is included in Appendix C.1.
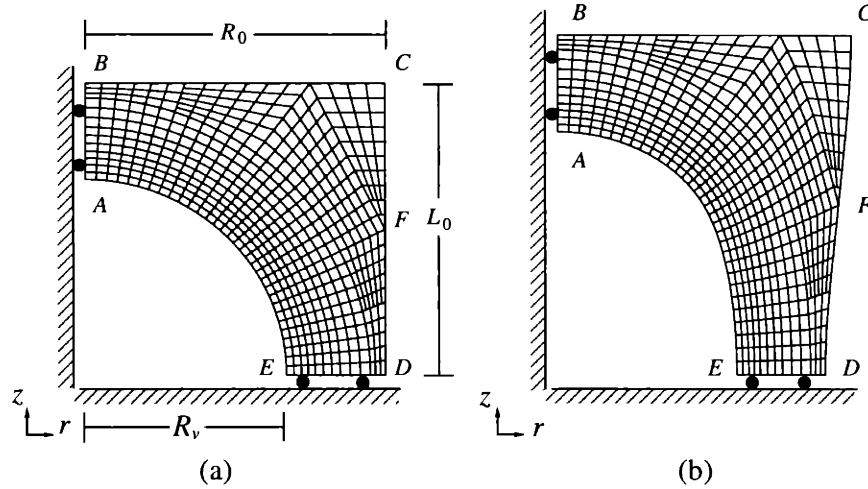
Figure 2-5: Finite element model of SA particle distribution: (a) sample undeformed mesh, $f_0 = 20\%$; (b) sample deformed mesh, $f_0 = 20\%$.

Note that these boundary conditions were originally proposed and used by Tvergaard in a study of cavity growth and the interaction between small and large voids (Tvergaard, 1996; Tvergaard, 1998). However, the phenomenon explored by Tvergaard differs substantially from that discussed here, as well as from that presented in

Socrate and Boyce (1999). More specifically, since the Tvergaard RVE maintained a large axial spacing between large voids, matrix deformation localized at the void equators and, consequently, the Tvergaard study did not detect the significant changes in particle interactions discussed here.

2.1.3   Alternative Staggered Array (SAb) model

Alternatively, the axisymmetric cell generated by the revolution of plane $BCDGH$ in Fig. 2-6, around the z-axis can be used to represent the SA model material [2]. When the symmetry of the underlying microstructure is taken under consideration,
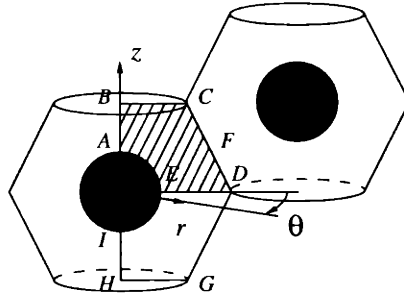
Figure 2-6: Motivation for the alternative SA model.

this axisymmetric RVE reduces to the two-dimensional domain $ABCDE$. This alternative model, termed hereafter (SAb), deforms subject to identical constraints with the SA model (i.e. subject to constraints (2.2)-(2.5)); where in the actual model, boundary CD is modified to satisfy constraint (2.4) in the reference configuration, while deviating minimally from a straight line (see Fig. 2-7)

Although none of the axisymmetric RVE models of the SA microstructure is space-filling, it will be shown that both models predict very similar deformation patterns locally and macroscopically. This result justifies the assumptions made in reducing the three-dimensional SA microstructure to the two-dimensional domains analyzed.

---

[2]To create plane $BCDGH$, line CD is drawn perpendicular to the line connecting the centers of nearest neighboring particles and passes through its mid-point, point F.
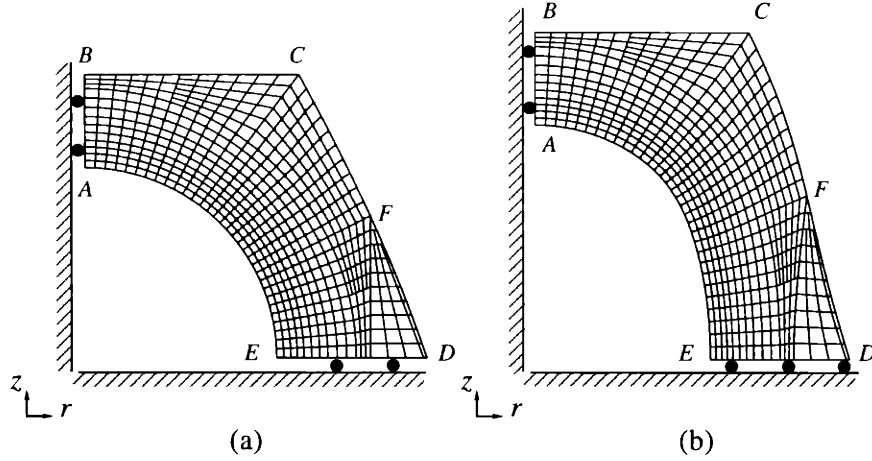
Figure 2-7: Alternative finite element model of SA particle distribution: (a) sample undeformed mesh, $f_0 = 20\%$; (b) sample deformed mesh, $f_0 = 20\%$.

2.1.4 Macroscopic cell response

To calculate the overall mechanical response of the RVE models, it is taken into account that stress continuity in the model material demands the cell volume-averaged stress, $\mathbf{T}_{RVE}$, to be equal to the macroscopically applied stress, $\overline{\mathbf{T}}$. Namely that,

$$\overline{\mathbf{T}} = \mathbf{T}_{RVE} = \frac{1}{V_{RVE}} \int_{V_{RVE}} \mathbf{T}(\mathbf{x})\, dV, \tag{2.6}$$

where $\mathbf{x}$ is the position vector of an arbitrary point in the deformed configuration, $\mathbf{T}(\mathbf{x})$ is the Cauchy stress tensor at that point and V_{RVE} is the deformed volume of the RVE. Since $\operatorname{div} \mathbf{T} = \mathbf{0}$ from equilibrium and $\operatorname{grad} \mathbf{x} = \mathbf{I}$, the Cauchy stress tensor can be written as

$$\begin{aligned}
\mathbf{T}(\mathbf{x}) &= \operatorname{sym}\left[(\operatorname{div}\mathbf{T}) \otimes \mathbf{x} + \mathbf{T}(\operatorname{grad}\mathbf{x})\right] \\
&= \operatorname{sym}\left[\operatorname{grad}(\mathbf{T}\mathbf{x})\right].
\end{aligned} \tag{2.7}$$

Utilizing this relation and the divergence theorem, the volume integral of eqn (2.6) becomes the surface integral:

$$\mathbf{T}_{RVE} = \frac{1}{2V_{RVE}} \int_S (\mathbf{x} \otimes \mathbf{t} + \mathbf{t} \otimes \mathbf{x}) \, \mathrm{d}S, \tag{2.8}$$

where $\mathbf{t} = \mathbf{T}\,\mathbf{n}$ is the traction vector applied at an arbitrary point $\mathbf{x}$ on the RVE outer boundary and S is the bounding surface of the RVE in the deformed configuration. Moreover, the deformed volume of the RVE is given by

$$V_{RVE} = \frac{1}{3} \int_S \mathbf{x} \cdot \mathbf{n} \, \mathrm{d}S, \tag{2.9}$$

where $\mathbf{n}$ is the outward normal of area segment $\mathrm{d}S$. Concluding, the far-field stresses can be simply calculated using eqn (2.8) from the reaction forces at nodes along the cell's boundary.

Similarly, the macroscopic deformation gradient, $\overline{\mathbf{F}}$, is found from

$$\overline{\mathbf{F}} = \overline{\mathbf{R}}\,\overline{\mathbf{U}} = \overline{\mathbf{V}}\,\overline{\mathbf{R}}$$

$$= \mathbf{I} + \frac{1}{V_0} \int_{V_0} \mathrm{Grad}\,\mathbf{u}(\mathbf{y}) \, \mathrm{d}V_0 \tag{2.10}$$

$$= \mathbf{I} + \frac{1}{V_0} \int_{S_0} \mathbf{u} \otimes \mathbf{n}_0 \, \mathrm{d}S_0,$$

where $\mathbf{y}$ is the position vector of an arbitrary point in the reference configuration, $\mathbf{u}(\mathbf{y})$ is the displacement of that point, V_0 is the undeformed volume of the RVE, S_0 is the undeformed bounding surface of the RVE, and $\mathbf{n}_0$ is the outward normal of the area segment $\mathrm{d}S_0$. Finally, the macroscopically applied logarithmic strain, $\overline{\mathbf{E}}$, can be calculated from

$$\overline{\mathbf{E}} = \ln \overline{\mathbf{U}} = \ln \overline{\mathbf{V}}, \tag{2.11}$$

where for the deformations studied, $\overline{\mathbf{F}} = \overline{\mathbf{U}} = \overline{\mathbf{V}}$, i.e. $\overline{\mathbf{R}} = \mathbf{I}$.

2.2 Matrix constitutive behavior

The primary focus of this study is to investigate changes in the deformation behavior of rubber-modified PA-6 ensuing from changes in its matrix morphology. To simulate these changes, the matrix material of the RVE models, was divided into two regions. As illustrated in Fig. 2-8, the region of radial extent not more than $\Lambda_c/2$, immediately surrounding the particle, represents the transcrystallized portion of the matrix, while the rest of the RVE matrix material represents the bulk material of random orientation. The relative extent of each region depends on the interparticle distance, Λ, being modeled. In the extreme case where the simulated spacing is smaller than Λ_c, the oriented material percolates through the matrix. However, when $\Lambda \gg \Lambda_c$, the extent of oriented growth becomes negligible, and randomly-oriented isotropic material effectively occupies the entire matrix. The two limiting cases of $\Lambda \leq \Lambda_c$ and $\Lambda \gg \Lambda_c$ were studied in detail, where the influence of matrix morphology was captured by the constitutive model of the matrix material. In the limit of $\Lambda \gg \Lambda_c$, the matrix was taken to be isotropic and was modeled using a constitutive model for polymeric materials as described below, while for $\Lambda \leq \Lambda_c$, the matrix was taken to be highly anisotropic in both elastic and plastic behavior. In incorporating the anisotropic behavior, the textured material was taken to be transversely isotropic about the lamellar growth direction of crystallization. A set of Cartesian basis vectors, $\{m_1, m_2, m_3\}$, was consequently chosen to coincide with the principal axes of anisotropy, at each position y in the reference configuration. Specifically, base vector $m_1(y)$ was taken to be the growth direction. At the initiation of crystallization, this direction coincides with the radial normal to the particle-matrix interface as shown in Fig. 2-8 (b). Base vector $m_3(y)$ was chosen to coincide with the circumferential basis vector, e_θ, of the axisymmetric cell [3] and base vector $m_2(y)$ was taken to be mutually orthogonal to $m_1(y)$ and $m_3(y)$. Finally, a third cell morphology was studied in which both constitutive behaviors were present. In this case, the transition in

---

[3]Note that by selecting e_θ to be a principal material direction, the validity of the axisymmetric assumption of the RVE models is sustained.

28

matrix texture (and therefore constitutive behavior) was modeled to take place in a stepwise fashion; where mechanical tests of Muratoglu et al. (1995a) on partially and fully transcrystallized thin films support this assumption.

(a)
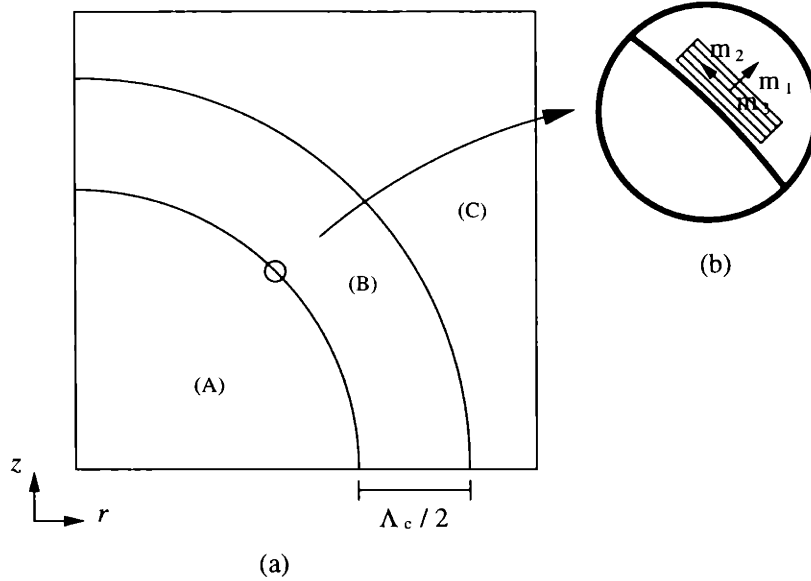
Figure 2-8: (a) Schematic of proposed material modeling of computational domain, consisting of particle (A); transcrystallized matrix domain (B); and randomly-oriented isotropic matrix domain (C); (b) local material directions near the particle-matrix interface (parallel lines indicate the orientation of the hydrogen-bonded planes with respect to the interface).

2.2.1 Constitutive modeling of the isotropic matrix material $(\Lambda \gg \Lambda_c)$

Semicrystalline polymers are heterogeneous solids consisting of amorphous and crystalline components. Understanding their large-strain deformation behavior requires a sufficient knowledge of their underlying morphology and local deformation modes (for a review see: Bowden and Young (1974), Lin and Argon (1994)). When crystallized from a melt, most semicrystalline polymers form spherulites. In a spherulite, the ribbon-like crystals (lamellae) of the polymer grow radially from a common center, with amorphous material filling the inter-lamellar regions. Although the crystallites

29

themselves are highly anisotropic, their random positioning in a spherulitic structure, coupled with the isotropic behavior of amorphous regions, gives rise to an overall mechanical response that is essentially isotropic at scales larger than the spherulite diameter. For large monotonically applied loading, the main features of this response include: linear elastic behavior, followed by a gradual roll-over of the stress-strain curve corresponding to yield, followed by gradual monotonic hardening of the stress-strain response, followed by dramatic hardening at large strains. While these general trends in behavior are very similar to those observed in glassy polymers, it is still a somewhat open question as to which phase of the semicrystalline polymers dominates their mechanical response.

One attempt at answering this question has been made by Lee and co-workers (1993), who took into account the micro-composite morphology of semicrystalline polymers in terms of an inclusion consisting of a crystalline lamellae and its corresponding amorphous layer. In this model, the two components of the composite lamellar inclusion were assumed to deform homogeneously, obeying a Sachs-like aggregate interaction law. The visco-plastic behavior of the crystalline component was modeled taking into account the kinematic deficiencies discussed by Parks and Ahzi (1990), while the constitutive behavior of the amorphous component was modeled by introducing a back-stress tensor in the flow rule to account for orientation-induced hardening, similar to the developments of Boyce et al. (1988). Lee et al. applied their model to the deformation of initially isotropic HDPE and obtained stress-strain and texture evolution results in reasonably good agreement with experiment. In terms of the relative contributions of each phase to the shape of the stress-strain curve, the authors found that while the initial yield behavior of the polymer was a result of overcoming resistances in both crystalline and amorphous domains, the post-yield strain hardening of the material was dominated by the deformation of amorphous domains up to the point of the very highest strains. Based on these results and the fact that the amorphous content of PA-6 (60 %) is much higher than that of HDPE (10-25 %), it is proposed that a modified version of the Arruda and Boyce (1993) model for glassy polymers is used to capture the mechanical response of isotropic

30
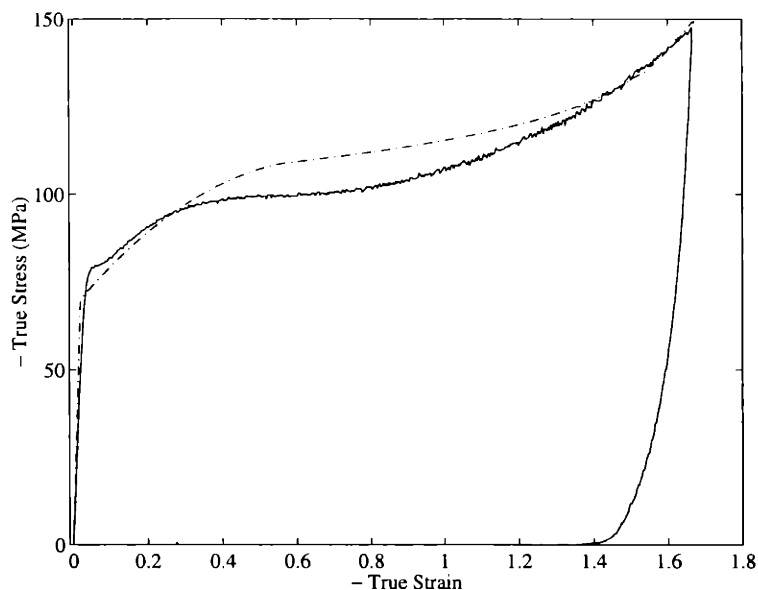
Figure 2-9: Uniaxial compression of initially isotropic PA-6 ($\dot{\epsilon} = 0.01$ sec^{-1}): (—) experimental data; (– ·) model predictions.

PA-6. Details of this model are included in Chapter 3, while Fig. 2-9 illustrates how the model predictions compare to an actual uniaxial compression test. The model accurately captures the initially linear elastic response of the material and most of its post-yield behavior. Moreover, the predicted behavior in simple tension is in good agreement with experimental data obtained by G'Sell and Jonas (1981). Thus, even though much of the detail regarding the local modes of deformation and morphology of the material is omitted, the Arruda-Boyce model sufficiently captures important features of the mechanical response of isotropic PA-6.

2.2.2 Constitutive modeling of the anisotropic matrix material ($\Lambda \leq \Lambda_c$)

Two different forms of PA-6 crystals normally coexist in the crystalline component of the bulk material, at roughly equal proportion: monoclinic α and monoclinic γ (Galeski et al., 1987). The differences between the two forms are in the lattice parameters and in the position of the hydrogen bonds between the N–H and the C=O

31

groups. Specifically, in the γ form the hydrogen bonds bridge parallel macromolecular chains across fold planes, while in the α form they bridge anti-parallel chains in a given fold plane. In other words, the γ form requires a twist of each chain away from its fold plane and is thus characterized by a three-dimensional network of hydrogen bonds, while the α form requires no such twist and is therefore characterized by sheets of hydrogen bonding. While in characterizing the mechanical behavior of such crystalline structures it is desirable to experiment on single crystals, the small size of polymer crystals prohibits this kind of work. Rather, highly-textured materials that macroscopically resemble single crystals ("quasi-single" crystal), are produced by compressing the bulk material in a channel die. Lin and Argon (1992) developed such "quasi-single" crystal PA-6 samples containing both α and γ crystal forms and used them to study the mechanical anisotropy of the crystalline component of bulk PA-6. They established that its plastic deformation is primarily derived from three crystallographic slip processes consisting of the (001)[010] and (100)[010] chain slip systems, and the (001)[100] transverse slip system. Moreover, they determined that the easiest slip process occurs along the hydrogen-bonded planes, i.e., the {001} crystallographic planes and in the direction of the chain, i.e., the ⟨010⟩ crystallographic direction. This slip process has a resistance to shear, $g_0 = 16$ MPa, while the other two resistances are almost equivalent, having a shear strength, $\approx 1.5\,g_0$. This substantial difference in resistance to shear, as well as the insufficient number of slip systems to accommodate arbitrary plastic deformation of the crystal, make the PA-6 crystallites highly anisotropic in their mechanical response. In the bulk material, this strong mechanical anisotropy of the crystalline component is evened out by random spherulitic texture, making the contribution of this component to the overall mechanical response of the material secondary. However, in the presence of crystallographic orientation the role of the crystalline component is governing. Since the material of interest here is highly-textured, it can be assumed that its mechanical anisotropy is primarily derived from its crystalline component, and thus, the material can be idealized as being 100 % crystalline. Specifically, its elastic anisotropy can be determined using experimental data obtained by Lin and Argon (1992) for "quasi-single" crystal

PA-6, and its plastic anisotropy by numerically simulating the plastic deformation of an aggregate of PA-6 crystallites. While the accuracy of the determined anisotropy is difficult to assess, it will provide a sufficiently representative material behavior for comparison to the bulk isotropic behavior introduced in the previous section.

Anisotropic elasticity

The large strain, plane strain compression of bulk PA-6 produces a material that macroscopically mimics a single crystal (Lin and Argon, 1992). More specifically, during the deformation the macromolecular chains align with the flow direction, while the hydrogen-bonded planes orient perpendicular to the loading direction. Since both α and γ crystal forms are present in the bulk material, plane strain compression results in a dual orientation of the $\{100\}$ planes with respect to the loading axis, and consequently, in orthotropic symmetry. Therefore nine independent constants are required to completely characterize the elastic behavior of "quasi-single" crystal PA-6. For convenience, these constants were used as a guide in modeling the elastic response of the material crystallized near a second phase. Thus the Young's modulus of the transcrystallized material along the direction normal to the hydrogen-bonded planes, E_1, was taken as the modulus of the "quasi-single" crystal material along the loading direction. Moreover, the moduli along the transverse directions, $E_2 = E_3$, were taken to be sufficiently lower than the modulus of the "quasi-single" material in the flow direction to account for the radial orientation of chains about the normals to the hydrogen-bonded planes in the actual material. Since the Poisson's ratios, $\nu_{23} = \nu_{32}$, represent the plane of transverse isotropy of the textured material, they were taken to be equal to the Poisson's ratio of bulk isotropic PA-6. Finally, the values for $\nu_{21} = \nu_{31}$ and shear moduli, $G_{21} = G_{31}$ were taken directly from Lin and Argon. A summary of the values used to characterize the elastic response of transversely isotropic PA-6 expressed in the reference frame of Fig. 2-8 (b) is given in the table below.

E_1 (GPa)	$E_2 = E_3$ (GPa)	$G_{21} = G_{31}$ (GPa)	$\nu_{21} = \nu_{31}$	$\nu_{23} = \nu_{32}$
3.460	4.5	0.4	0.53	0.33

Table 2.1: Elastic constants determined for transversely isotropic PA-6.

Anisotropy of yield

The plastic response of the oriented material was modeled in terms of the anisotropic yield criterion developed by Hill (1947) for metals of orthotropic symmetry. In a Cartesian frame of reference locally aligned with the principal axes of anisotropy, the Hill yield surface takes the form:

$$\left(F(T_{22} - T_{33})^2 + G(T_{33} - T_{11})^2 + H(T_{11} - T_{22})^2 + 2LT_{23}^2 + 2MT_{31}^2 + 2NT_{12}^2\right)^{\frac{1}{2}} - \sigma_{BY} = 0,$$

(2.12)

where F, G, H, L, M, N are constants characteristic of the state of anisotropy given by the following relations:

$$F = \frac{1}{2}\left(\frac{1}{R_{22}^2} + \frac{1}{R_{33}^2} - \frac{1}{R_{11}^2}\right),$$

$$G = \frac{1}{2}\left(\frac{1}{R_{33}^2} + \frac{1}{R_{11}^2} - \frac{1}{R_{22}^2}\right),$$

$$H = \frac{1}{2}\left(\frac{1}{R_{11}^2} + \frac{1}{R_{22}^2} - \frac{1}{R_{33}^2}\right),$$

(2.13)

$$L = \frac{3}{2R_{23}^2},$$

$$M = \frac{3}{2R_{13}^2},$$

$$N = \frac{3}{2R_{12}^2},$$

34

and R_{11}, R_{22}, and R_{33} are ratios of the tensile yield strengths of the textured material in different directions to the tensile yield strength of the bulk isotropic material, σ_{BY} = 70 MPa. Similarly, the constants R_{12}, R_{13} and R_{23} are ratios of the yield strengths in shear to the shear yield strength of the bulk isotropic material, $\tau_{BY} = \sigma_{BY}/\sqrt{3}$. Owing to the transverse isotropy of the oriented material, only four of these ratios need to be determined. Ideally they should be measured experimentally and allowed to vary with strain. However, since the transcrystallized material can only be formed in thin film conditions, mechanical tests required to determine its strength in different directions are very difficult or even impossible to perform. While some attempts have been made, only a limited amount of data is available in the literature. For instance, Muratoglu et al. (1995a) were able to prepare thin films of the desired texture and test them in tension. They determined that the tensile strength of the textured material was about 1.8 times that of the bulk isotropic material, indicating the pronounced mechanical anisotropy of the transcrystallized material.

While this result confirms the expected trend in behavior, the absolute value of the ratio determined by Muratoglu is still open to question, given the immense difficulty of mechanical tests performed on free-standing films of sub-micron thickness. Alternatively, a complete set of parameters can easily be obtained numerically as is proposed here. Since the mechanical anisotropy of the textured material is primarily derived from its crystalline component, the material can be idealized as being 100 % crystalline, and a polycrystal plasticity model specifically designed for low symmetry crystals can be used to simulate its plastic deformation. For this purpose, the Constrained Hybrid (CH) model, as initially proposed by Parks and Ahzi (1990) and later modified by Lee et al. (1994, 1995) for polymer crystals of lower symmetry was employed. Details of the CH model are included in Chapter 3, while the following paragraphs outline the method used to assess the anisotropy of yield of transversely isotropic PA-6. Initially an important implication of the geometry of the slip process, the re-orientation of a crystal lattice undergoing slip relative to the stress axis, is exploited in order to construct the desired textures, while subsequently, the developed textures are probed for their strengths in different directions.

It is well-known that in a crystal lattice deforming under uniaxial compression by a single slip process, the normal to the slip plane rotates towards the loading axis. This phenomenon is also observed in crystal aggregates where the deformation process is dominated by one preferred slip system. In the case of PA-6, deformation is dominated by slip occurring on the hydrogen-bonded planes and along the direction of the chain. Thus, uniaxial compression of an initially random texture results in a highly-textured material, where the hydrogen-bonded planes are oriented perpendicular to the compression axis, and the chains are oriented radially about that axis. In taking advantage of this process, different amounts of texture can be accomplished by simply compressing a crystal aggregate of initially random texture to different compression ratios. Figure 2-10 depicts such a texturing process in terms of pole figures of the normals to the hydrogen-bonded planes, $\{001\}$, and of the chain direction, $\langle 010 \rangle$, at different compression ratios. The mechanical response of the aggregate is also depicted, in terms of an aggregate-averaged true stress vs. true strain curve, where the stress is normalized by the easiest chain-slip strength, g_0. As expected, with increasing deformation in the simulation, the normals to the hydrogen-bonded planes begin to align with the loading axis, while the chains start to re-orient radially about that axis. A sudden hardening in the aggregate macroscopic mechanical response also manifests this sharpening of texture, i.e., as fewer and fewer slip systems remain favorably oriented to accommodate the deformation, compressing the aggregate further becomes increasingly difficult.

Several different textures (A)-(E), were obtained by this process and were tested for mechanical anisotropy. Although simulations of the type performed here can easily determine the strain dependence of yield, in this study attention is confined to the initial yield behavior of the textured material. Figure 2-11 summarizes the initial ratios required by the Hill criterion as a function of texture. As can be seen, these ratios start at unity for texture (A), indicating an initially isotropic material, but start to differentiate with increasing crystallographic orientation. Thus, all ratios related to tensile loading indicate monotonically increasing yield strengths of the material with sharpening texture. For reasons mentioned above, this hardening phenomenon is more

{001}   <010>

(A)

(B)

(C)

(D)

(E)

(a)

(b)
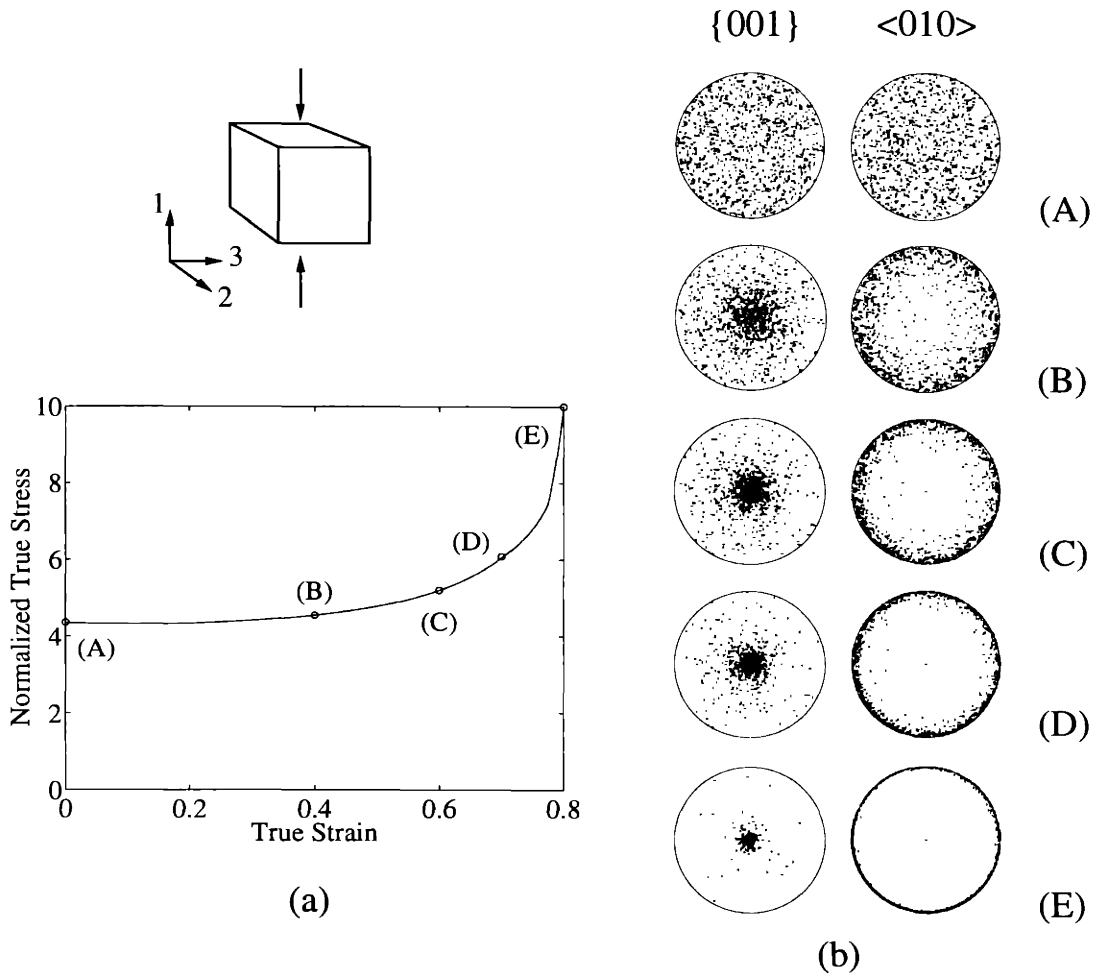
Figure 2-10: Numerical construction of textures: (a) simulated stress-strain behavior in uniaxial compression of an initially isotropic crystal aggregate; (b) evolution of {001} and ⟨010⟩ pole figures with increasing deformation (poles are shown looking down the loading axis).
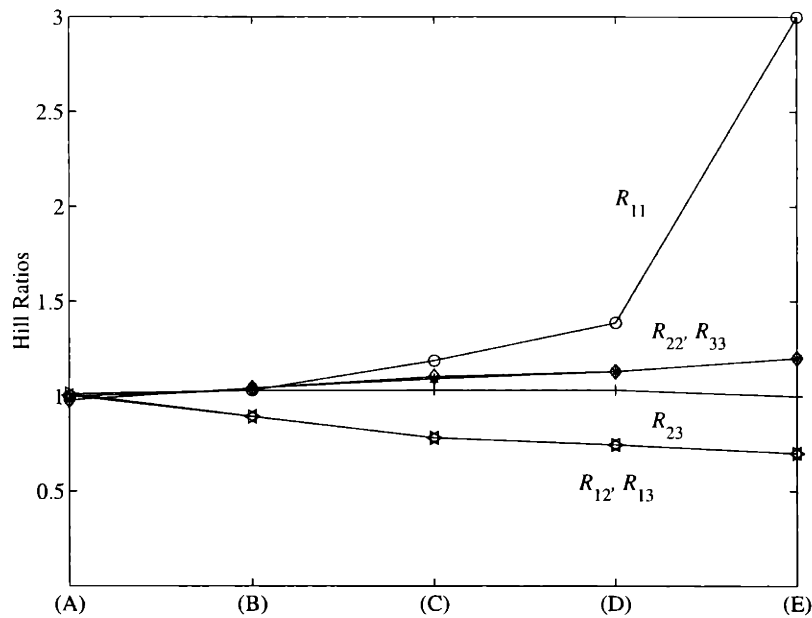
Figure 2-11: Computed Hill ratios vs. texture.

pronounced in the 1-direction, while the transverse isotropy suggested by the nature of the developing textures is verified by the fact that the two flow-directions remain equivalent at all textures. Moreover, the ratios related to shear loading indicate that the strength of the material under 12 and 13 imposed shears decreases monotonically with texture sharpening, reaching a computed value of 0.7. The reason for this decrease is the favorable orientation of the "easy-shear" slip systems with respect to the applied deformation. Finally, the strength of the material under 23 imposed shear is nearly unaffected by texture. The Hill ratios for the sharpest texture, texture (E), are summarized in the table below. As can be seen, even for the sharpest texture the predicted value for $R_{22} = R_{33}$, roughly 1.2, is much lower than that determined by Muratoglu et al. (1995a) experimentally. While as mentioned above, the accuracy of the experimental value (1.8) is uncertain, the one determined by the CH model is admittedly too low [4]. Consequently, a compromise between the two values (1.6) was used in the simulations to follow. Moreover, given the fact that hydrogen-bonding

---

[4]Due to the approximations made in estimating the constrained stress components in the CH model, the results tend to underestimate the strength of the highly textured material.

in the α crystal form results in planar conformations of the chain rather than three-dimensional networks, g_0 in a material containing only α crystals is expected to be lower than that determined for a material containing both α and γ crystal forms. Thus, rather than 0.7 a value of 0.5 for $R_{12} = R_{13}$ was used [5]. The effect of each parameter on the macroscopic mechanical response of the models is separately studied in Sec. 4.2.3

	R_{11}	$R_{22} = R_{33}$	$R_{12} = R_{13}$	R_{23}
(a)	3.0	1.2	0.7	1.0
(b)	3.0	1.6	0.5	1.0

Table 2.2: Hill ratios: (a) obtained by the CH model for texture (E); (b) used in the simulations.

Local material directions

As formulated in the previous sections, the constitutive description of the anisotropic matrix material requires a Cartesian set of basis vectors, $\{\mathbf{m}_1, \mathbf{m}_2, \mathbf{m}_3\}$, locally aligned with the principal axes of anisotropy. Since the axis of transverse isotropy (base vector $\mathbf{m}_1(\mathbf{y})$) coincides everywhere with the direction of lamellar growth, its orientation with respect to the global set of axes, $\{r, z, \theta\}$, depends on the underlying texture of the matrix and, in the case of $\Lambda \leq \Lambda_c$, the periodicity of the assumed particle distribution. More specifically, when $\Lambda > \Lambda_c$, $\mathbf{m}_1(\mathbf{y})$ follows the direction of lamellae oriented perpendicular to the particle-matrix interface. However, when $\Lambda \leq \Lambda_c$ the periodicity of the assumed microstructures dictates that the crystalline lamellae emanating radially from one particle rotate gradually, away from the interface to meet lamellae emanating from a nearest neighbor without forming orientation kinks, and consequently, $\mathbf{m}_1(\mathbf{y})$ changes direction accordingly. Figure 2-12 schematically illustrates such textures for both RA and SA particle distributions. As can be seen, the periodicity of the RA model dictates that the normals to the hydrogen-bonded planes

---

[5]Clearly, the α monoclinic crystal form is much more anisotropic than the equivalent orthotropic material comprising both α and γ crystal forms.
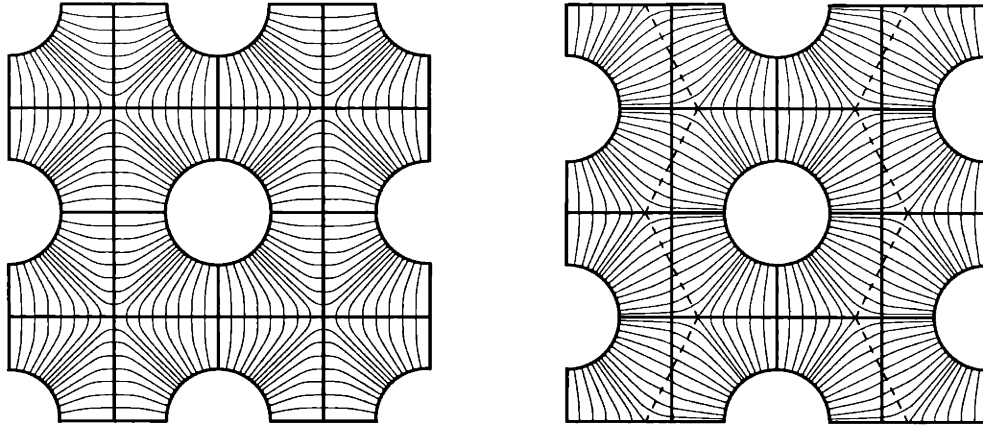
Figure 2-12: Schematic of assumed texture for $\Lambda \leq \Lambda_c$ in: (a) the RA model; (b) the SA model. Thick lines represent RVE boundaries, while thin lines represent lamellar growth directions, i.e., lines tangent to the local $\mathbf{m}_1$ direction.

rotate near the outer boundaries of the RVE in order to meet them perpendicularly. In addition, symmetry with respect to the z-plane and axisymmetry about the z-axis dictate that they orient along radial directions near the equator and parallel to the axis near the pole of the particle. As a result, only a small portion of the matrix material remains favorably oriented to accommodate axial deformation. On the other hand, in the SA model, preferentially-oriented material spans the entire interparticle regions. This difference of texture in the two models will be shown to have a substantial influence on the propagation of plasticity in the matrix, as well as on the overall mechanical response of the material. Note that in this study the definition of the local reference frame, $\{\mathbf{m}_1, \mathbf{m}_2, \mathbf{m}_3\}$, within each individual element, was accomplished by carrying out a heat transfer analysis. The idea is to use the same mesh for both heat transfer and stress analyses and to take base vector, $\mathbf{m}_1(\mathbf{y})$, to be parallel to the heat flux vector at each integration point. The details of this procedure are discussed in Appendix A. In the deformation simulations to follow, $\{\mathbf{m}_1, \mathbf{m}_2, \mathbf{m}_3\}$ at each integration point, is taken to rotate with the average rigid body motion of the material point, and that is the only evolution in anisotropy considered.

2.3   Loading conditions

Boundary conditions on the RVE models simulated both uniaxial tension and axisymmetric triaxial conditions. In applying triaxial loading, the triaxiality parameter, Σ, given by the ratio of the cell-averaged hydrostatic stress, $1/3\ \overline{T}_{kk}$, to the cell-averaged equivalent stress, $\overline{T}_{eq}$,

$$\Sigma = \frac{\overline{T}_{kk}}{3\ \overline{T}_{eq}} = \frac{(2\ \overline{T}_{rr} + \overline{T}_{zz})}{3\ |\overline{T}_{zz} - \overline{T}_{rr}|} \qquad (2.14)$$

was kept constant by means of a user-element, further defined in Appendix B, that monitors the level of applied axial stress and calculates the appropriate radial traction, which is then applied to the lateral boundary of the RVE. For simplicity, uniaxial tension was also applied using the same user-element, where Σ was specified to be equal to 1/3.

Chapter 3

Material models

In modeling the macroscopic mechanical behavior of semicrystalline polymers, one must be able to relate the deformation of spherulitic structures to the deformation of lamellar crystals and amorphous layers. The principal mechanisms involved in the deformation of both phases are well understood, albeit very complex when considered in the context of the local morphology. Like most inorganic crystals, the crystalline component of semicrystalline polymers deforms plastically by slip, twinning, and stress-induced martensitic transformations. Crystallographic slip is considered as the most important deformation mechanism since it is generally easier to activate and is capable of producing larger plastic strains than the other two. Intercrystalline deformation of amorphous regions takes place predominantly by simple shear, while the mechanical coupling between the two phases depends on the nature of the interface and density of tie molecules.

Earlier models on the deformation behavior of semicrystalline polymers confined attention to the deformation of spherulites (for a review of the most important such models see Lin and Argon (1994)). Although models of this type indeed shed light on the complex deformation processes taking place at the spherulite level, it is ultimately desirable to follow the deformation of the material on a macro-scale, and relate these physically-based microstructural theories to continuum theory. In the case of polycrystal metals, this transition was made with crystal plasticity models, such as the Taylor model, which assumes uniform deformation within a crystal aggre-

gate. The Taylor assumption has proved to be successful in the case of metal crystals, which possess a sufficient number of slip systems to accommodate arbitrary plastic deformation. However, in the case of polymer crystals, the number of independent modes of deformation is usually less than the five required for a general homogeneous deformation, making the Taylor estimate of aggregate stress to become unbounded. Therefore, modifications on existing crystal plasticity models are required before they can be applied to crystalline polymers.

Parks and Ahzi (1990), were the first to relate the local modes of deformation in semicrystalline polymers to continuum plasticity theory. In their so-called Constrained Hybrid (CH) model, they idealized bulk semicrystalline polymers as being 100 % crystalline and modeled the lack of full kinematic freedom of polymer crystals in terms of kinematic constraints. Following the insight of the Taylor model of crystal plasticity, they specified the local deformation rate of each crystal to deviate minimally from the macroscopically applied one, so that it satisfies the kinematic constraints. Parks and Ahzi applied their model to the deformation of HDPE, and obtained good qualitative agreement with experimental results in terms of the predicted evolution of texture and mechanical behavior. A more refined version of the CH model was proposed recently by Lee et al. (1995) in which the kinematic constraints associated with each crystal, need not be identified explicitly. This reformulation of the CH model facilitates its application to the deformation of materials with lower symmetry crystals in which the kinematic constraints are hard to identify. Lee et al. (1993) also developed a more elaborate model where both phases of semicrystalline polymers are taken into account. While undoubtedly the most complete model to date, the amount of detail incorporated in this model is beyond the scope of this study. Rather, the Arruda and Boyce (1993) model for amorphous polymers was used to capture the deformation behavior of isotropic PA-6 and the modified CH model (Lee et al., 1995) to mimic the mechanical response of transversely isotropic PA-6. Both models are further discussed in the sections to follow. Notation used in the previous chapter is carried through here, while additional conventions needed for the formulations to follow are given below. Fourth-order tensors are in upper-case calligraphics ($\mathcal{A}$). The

fourth-order identity tensor is denoted by $\mathcal{I}$. The prefixes, "det" and "tr" indicate the determinant and the trace respectively, a superscript $(\cdot)^T$ the transpose, a prime $(\cdot)'$ the deviatoric part of a tensor, a superscript $(\cdot)^{-1}$ the inverse of a tensor, and a superimposed dot the material time derivative unless otherwise stated. Finally, a quantity in angular brackets, $\langle \cdot \rangle$, represents the volume average of that quantity over an aggregate of crystals.

3.1 Arruda-Boyce model for amorphous polymers

Three constitutive elements enter the model formulation. A linear spring is used to characterize the initial elastic response of the material. A visco-plastic dashpot is used to capture the rate and temperature-dependence of yield, and a non-linear rubber elasticity spring is used to account for the anisotropic resistance to chain alignment that develops with plastic strain. The constitutive description of each element is summarized below within the context of a general finite strain deformation framework.

3.1.1 The kinematics of finite strain deformation

The deformation gradient, $\mathbf{F}$, is assumed to be represented by a multiplicative decomposition into an elastic and a plastic part:

$$\mathbf{F} = \mathbf{F}^e \mathbf{F}^p. \tag{3.1}$$

The elastic part of the deformation gradient, $\mathbf{F}^e$, is restricted to be a stretch only, $\mathbf{F}^e = \mathbf{V}^e = \mathbf{U}^e$, without loss of generality (Boyce et al., 1989). The plastic part, $\mathbf{F}^p$, is taken as the deformation gradient of a relaxed configuration obtained by elastically unloading to a stress-free state via $(\mathbf{F}^e)^{-1}$. The velocity gradient of that relaxed configuration, $\mathbf{L}^p = \dot{\mathbf{F}}^p(\mathbf{F}^p)^{-1}$, is then decomposed into symmetric and skew symmetric parts:

$$\mathbf{L}^p = \mathbf{D}^p + \mathbf{W}^p. \tag{3.2}$$

The skew-symmetric part, $\mathbf{W}^p$, represents the spin and is algebraically prescribed as a result of the imposed symmetry on the elastic deformation gradient. The symmetric part, $\mathbf{D}^p$, is the rate of shape change and is constitutively prescribed in Sec. 3.1.2.

3.1.2 Constitutive relations

A fourth-order isotropic elastic modulus tensor, $\mathcal{L}^e$, with Cartesian components given by

$$\mathcal{L}^e_{ijkl} = \frac{E}{2(1+\nu)} \left[(\delta_{ik}\delta_{ji} + \delta_{il}\delta_{jk}) + \frac{2\nu}{1-2\nu}\delta_{ij}\delta_{kl} \right], \tag{3.3}$$

constitutively characterizes the elastic element as follows

$$\mathbf{T} = \frac{1}{J}\mathcal{L}^e[\ln \mathbf{V}^e]. \tag{3.4}$$

Here $\mathbf{T}$ is the Cauchy stress, $\ln \mathbf{V}^e$ is the Hencky strain and $J = \det \mathbf{V}^e$. The plastic shear strain rate, $\dot{\gamma}^p$, is described by a thermally activated process according to:

$$\dot{\gamma}^p = \dot{\gamma}_o \exp\left\{ -\frac{\Delta G}{\kappa\Theta} \left[1 + \frac{\tau}{s}\right] \right\}, \tag{3.5}$$

where $\dot{\gamma}_o$ and ΔG are material parameters, τ is the equivalent shear stress (defined further below), κ is the Boltzmann's constant, Θ is the absolute temperature and s is the athermal shear strength.

The effect of pressure, $p = -\text{tr } \mathbf{T}$ on plastic flow is incorporated by adding the product αp to the shear strength, where α is the pressure sensitivity coefficient of the material. The initial strain hardening stage observed in PAs, is modeled by taking s to evolve from initial value, s_0, to a saturation value, s_{ss}, in a manner similar to Boyce et al. (1988):

$$\dot{s} = h \left(1 - \frac{s}{s_{ss}}\right)^{\frac{1}{2}} \dot{\gamma}^p \tag{3.6}$$

where h, the hardening slope, is an additional material parameter.

The driving stress, $\mathbf{T}^*$, which continues to activate plastic flow, is given by

$$\mathbf{T}^* = \mathbf{T} - \frac{1}{J}\mathbf{F}^e\mathbf{T}^N(\mathbf{F}^e)^T, \tag{3.7}$$

where $\mathbf{T}^N$ is a network stress tensor that captures the effect of orientation-induced strain hardening. The description of strain hardening in amorphous polymers, due to the stretching of the underlying entangled molecular network, makes use of the analogy with the stretching of the cross-linked network in rubbers. Thus the network stress tensor, $\mathbf{T}^N$, is modeled using the Arruda and Boyce (1993) eight-chain model of rubber elasticity expression:

$$\mathbf{T}^N = \mu_R \frac{\sqrt{N}}{\lambda_{chain}} \mathcal{L}^{-1}\left(\frac{\lambda_{chain}}{\sqrt{N}}\right)[\mathbf{B} - \lambda_{chain}^2 \mathbf{I}]. \tag{3.8}$$

Here $\mathbf{B} = \mathbf{F}^p(\mathbf{F}^p)^T$ and $\lambda_{chain} = \left[\frac{1}{3}\operatorname{tr}\mathbf{B}\right]^{\frac{1}{2}}$ is the stretch of each chain in the model eight-chain network. In analogy to number of cross-links in rubbers, N here represents the number of rigid molecular units between physical entanglements, while μ_R is proportional to the initial stiffness. The Langevin function $\mathcal{L}$ is given by

$$\mathcal{L}(\beta) = \coth\beta - \frac{1}{\beta}; \quad \beta = \mathcal{L}^{-1}\left(\frac{\lambda_{chain}}{\sqrt{N}}\right), \tag{3.9}$$

where its inverse provides the functionality that as the chain stretches and λ_{chain} approaches its limiting extensibility, $\sqrt{N}$, the network stress increases dramatically.

The deviatoric part of the driving stress is used to define the equivalent shear driving stress by

$$\tau = \left(\frac{1}{2}\mathbf{T}^{*\prime} \cdot \mathbf{T}^{*\prime}\right)^{\frac{1}{2}}, \tag{3.10}$$

while finally the rate of shape change, $\mathbf{D}^p$, is constitutively prescribed by

$$\mathbf{D}^p = \frac{\dot{\gamma}^p}{\sqrt{2}\tau}\mathbf{T}^{*\prime}. \tag{3.11}$$

Table 3.1 lists the material parameters required by the model, as determined for isotropic PA-6 using experimental data presented in Chapter 2 as well as published results.

Elastic		Visco-plastic		Hardening		Orientation Hardening		
E (MPa)	ν	$\dot{\gamma}_0$ (s^{-1})	ΔG (J)	h (MPa)	s_0	s_{ss}	μ_R (MPa)	N
3500	0.33	5.4 (10^7)	2.5 (10^{-19})	150	65	95	3	4.5

Table 3.1: Material properties of isotropic PA-6.

3.2 Constrained Hybrid (CH) model

3.2.1 Single crystal rigid/visco-plasticity

First consider a low symmetry single crystal having $N \leq 5$ physically distinct and independent slip systems. The αth slip system in that crystal is defined by the normal to its slip plane, $\mathbf{n}^\alpha$, the slip direction, $\mathbf{s}^\alpha$, and a shear resistance, g^α, which is the value of the resolved shear stress on the slip plane in the slip direction that must be reached before shear can take place. The symmetric part of the traceless Schmid tensor associated with that slip system, $\mathbf{R}^\alpha$, is given by

$$\mathbf{R}^\alpha = \frac{1}{2} \left(\mathbf{s}^\alpha \otimes \mathbf{n}^\alpha + \mathbf{n}^\alpha \otimes \mathbf{s}^\alpha \right). \tag{3.12}$$

Moreover, the skew symmetric part, $\mathbf{A}^\alpha$, is given by

$$\mathbf{A}^\alpha = \frac{1}{2} \left(\mathbf{s}^\alpha \otimes \mathbf{n}^\alpha - \mathbf{n}^\alpha \otimes \mathbf{s}^\alpha \right). \tag{3.13}$$

To model crystallographic slip, a rate-dependent power law is used to relate the shear rate on slip system α, $\dot{\gamma}^\alpha$, and its corresponding resolved shear stress, τ^α,

$$\dot{\gamma}^\alpha = \dot{\gamma}_0 \frac{\tau^\alpha}{g^\alpha} \left| \frac{\tau^\alpha}{g^\alpha} \right|^{n-1}, \tag{3.14}$$

where $\dot{\gamma}_0$ represents a reference strain rate and $n \gg 1$ the rate exponent. For a single crystal subject to a uniform deviatoric Cauchy stress, $\mathbf{S}$, the resolved shear stress on

the αth slip system can be defined as

$$\tau^\alpha = \mathbf{S}^* \cdot \mathbf{R}^\alpha, \tag{3.15}$$

where $\mathbf{S}^*$ is a subspace specific modification of the deviatoric Cauchy stress tensor with zero components in the constrained directions, as defined by Parks and Ahzi (1990).

Concluding, the traceless deformation rate generated by all available slip systems is given by

$$\mathbf{D} = \sum_{\alpha=1}^{N} \dot{\gamma}^\alpha \mathbf{R}^\alpha, \tag{3.16}$$

and the lattice spin, $\mathbf{W}^*$, defined as the difference between the crystal spin, $\mathbf{W}$, and the plastic spin, $\mathbf{W}^p$, by

$$\mathbf{W}^* = \mathbf{W} - \mathbf{W}^p = \mathbf{W} - \sum_{\alpha=1}^{N} \dot{\gamma}^\alpha \mathbf{A}^\alpha. \tag{3.17}$$

Thus the rate of change of orientation of the crystallographic axes, for example the $\mathbf{b}$ axis is given by

$$\dot{\mathbf{b}} = \mathbf{W}^* \mathbf{b}. \tag{3.18}$$

3.2.2 The modified Taylor model

Now consider an aggregate of crystals subject to a traceless macroscopic velocity gradient, $\overline{\mathbf{L}}$, that can be additively decomposed into a macroscopic deformation rate, $\overline{\mathbf{D}}$, and a macroscopic spin, $\overline{\mathbf{W}}$,

$$\overline{\mathbf{L}} = \overline{\mathbf{D}} + \overline{\mathbf{W}}. \tag{3.19}$$

In the Parks and Ahzi (1990) formulation of the CH model, $\mathbf{D}$ is chosen to deviate

49

minimally from $\overline{\mathbf{D}}$, to satisfy both the local kinematic constraints and, in a volume average sense, global compatibility. In their reformulation of the CH model, Lee et al. (1993, 1995), showed that such local deformation rate can be written as

$$\mathbf{D} = \left\{ \mathcal{P}\langle\mathcal{P}\rangle^{-1} \right\} \left[\, \overline{\mathbf{D}} \,\right], \tag{3.20}$$

where $\mathcal{P}$ is a local fourth-order projection tensor expressed by

$$\mathcal{P} = \sum_{\alpha=1}^{N}\sum_{\beta=1}^{N}(\Gamma^{-1})^{\alpha\beta}\mathbf{R}^{\alpha} \otimes \mathbf{R}^{\beta}, \tag{3.21}$$

so that the kinematic constraints are accounted for implicitly. In eqn (3.21), Γ is a constant symmetric matrix, the components of which are given by

$$\Gamma^{\alpha\beta} = \mathbf{R}^{\alpha} \cdot \mathbf{R}^{\beta};\ 1 \le \alpha, \beta \le N \le 5. \tag{3.22}$$

Note that $\langle\mathcal{P}\rangle$ is invertible only for an aggregate of crystals that is not highly textured.

To complete the interaction law the local spin in each crystal, $\mathbf{W}$, is simply equated to the macroscopic spin, $\overline{\mathbf{W}} = \mathbf{W}$ so that the requirement of global compatibility, $\langle\mathbf{W}\rangle = \overline{\mathbf{W}}$, is satisfied trivially. Moreover, macroscopic equilibrium requires that $\overline{\mathbf{S}} = \langle\mathbf{S}\rangle$, which Lee et al. (1993, 1995) showed to be satisfied by taking

$$\overline{\mathbf{S}} = \langle\mathcal{P}\rangle^{-1}\left[\langle\mathbf{S}^{*}\rangle\right], \tag{3.23}$$

while assuming that

$$\mathbf{S} - \mathbf{S}^{*} = (\mathcal{I} - \mathcal{P})[\,\overline{\mathbf{S}}\,]. \tag{3.24}$$

Finally, note that for crystals possessing precisely five physically distinct slip systems, $\mathcal{P}$ reduces to $\mathcal{I}$, $\mathbf{S}^{*} = \mathbf{S}$ and $\mathbf{D} = \overline{\mathbf{D}}$.

3.2.3 Application to Polyamide-6

For PA-6, the information regarding the available deformation modes is summarized in Table 3.2. In this study, strain hardening and normal pressure effects on the shear

Type of Slip	Slip System $(n^\alpha s^\alpha)$	Shear Resistance (g^α) (MPa)
Chain Slip	(001)[010]	16.24
Chain Slip	(100)[010]	23.23
Transverse Slip	(001)[100]	23.18

Table 3.2: Deformation modes operable in the crystalline component of PA-6 (Lin and Argon, 1992).

resistance of each system were neglected, so that g^α remained constant during the deformation. Neglecting the intrinsic strain hardening is justified by the fact that the crystalline lamellae are very thin and cannot retain dislocations. Moreover, neglecting the pronounced normal pressure effects, observed by Lin and Argon (1992), is justified by the fact that these effects are most likely a consequence of the three-dimensional nature of hydrogen bonding in the γ crystal form of the PA, which is not present in the material of interest.

For the purpose of mathematical analysis, all tensor and vector components associated with the deformation of a single crystal were expressed in terms of an orthonormal basis, $\{e_1, e_2, e_3\}$, that was related to the crystallographic basis, $\{a, b, c\}$. Here, the orthonormal basis was chosen so that $e_2 = b/b$, $e_3 = c/c$ and $e_1 = e_2 \times e_3$. This choice of local crystal basis, simplifies the representation of the orientation of the crystal with respect to the global set of axes, typically given in terms of three Euler angles, $\{\phi, \psi, \omega\}$. Starting with the crystal basis parallel to the global system of reference, these three angles represent the required rotations for the crystal to reach its final orientation in the aggregate. If these rotations are expressed in matrix form, then by simple matrix multiplication one can get a rotation matrix in terms of Euler angles, which transforms all vector and tensor components expressed in terms of the crystal basis to global coordinates. All possible orientations can be obtained within
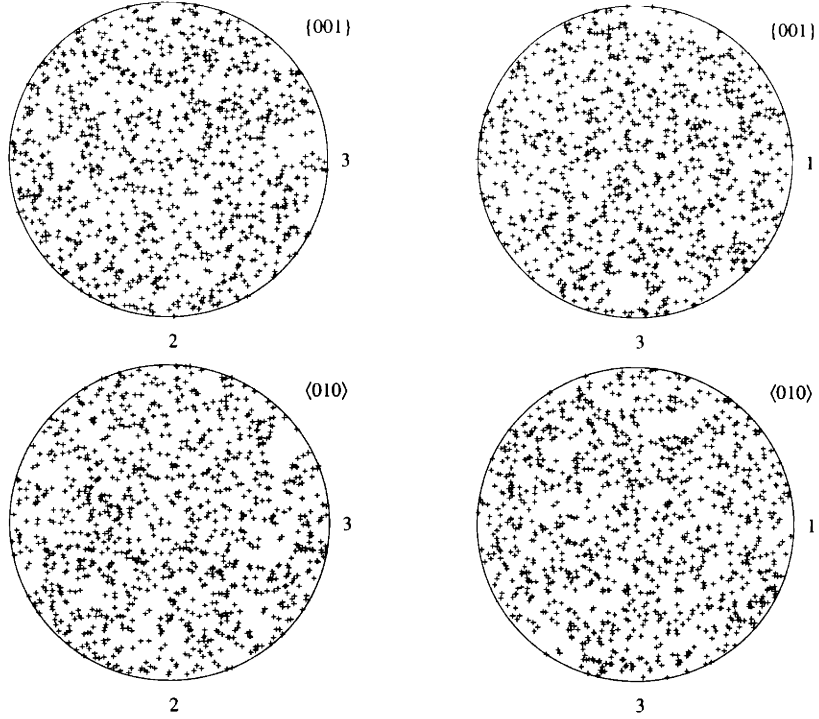
Figure 3-1: Pole figures of {001} planes and ⟨010⟩ directions in the initially isotropic crystal aggregate.

the range $0 \leq \phi \leq 2\pi$, $0 \leq \psi \leq \pi$, and $0 \leq \omega \leq 2\pi$. If all orientations are sufficiently sampled (i.e., there is an even spatial distribution of the poles as shown in Fig. 3-1), the resulting crystal aggregate is isotropic (see Fig. 3-2). Here, the global axes were chosen so that the 1-axis was parallel to the direction along which the initially isotropic texture was compressed, and the 2 and 3-axes were aligned with the flow directions.

To simplify the numerical implementation of the CH model further, all symmetric traceless tensors were reduced to five independent components according to the following convention:

$$\mathbf{A} \rightarrow \left\{ \frac{(A_{22} - A_{11})}{\sqrt{2}}, \sqrt{\frac{3}{2}} A_{33}, \sqrt{2} A_{23}, \sqrt{2} A_{13}, \sqrt{2} A_{12} \right\}. \qquad (3.25)$$

Finally, the simulation of deformation, for example simple tension in the 3-direction,
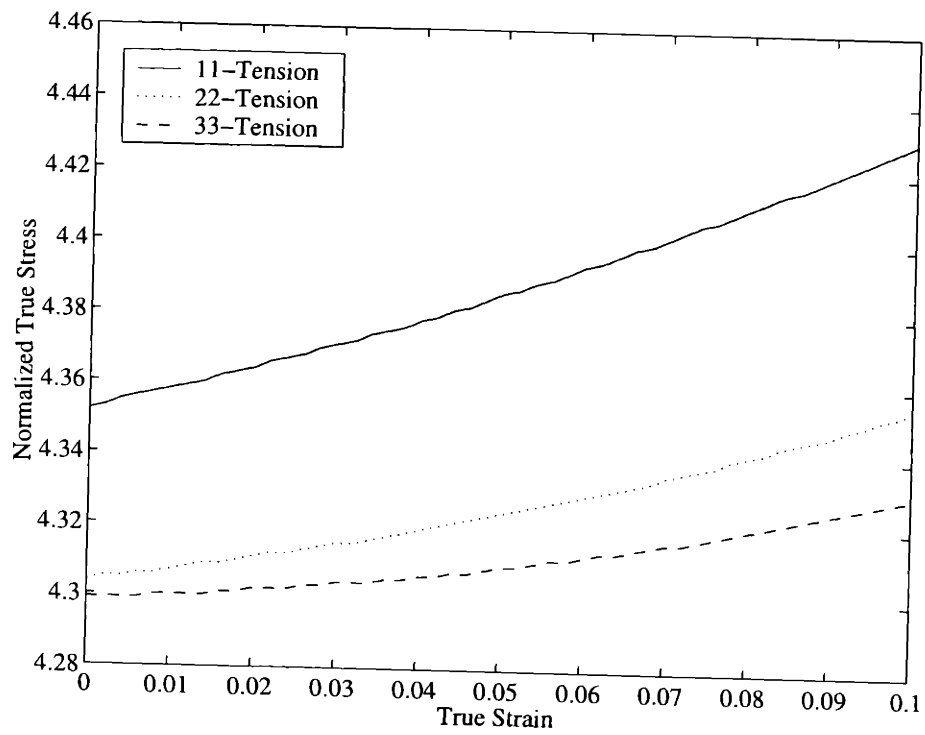
Figure 3-2: Simulated stress-strain behavior of the initially isotropic crystal aggregate in simple tension.

was achieved as follows: $\overline{D}_{33}$ was prescribed, while $\overline{D}_{11}$ and $\overline{D}_{22}$ were guessed iteratively so that they satisfy the incompressibility condition: $\overline{D}_{11} + \overline{D}_{22} + \overline{D}_{33} = 0$, and produce a state of uniaxial stress: $\overline{S}_{12} = \overline{S}_{13} = \overline{S}_{23} = \overline{S}_{11} - \overline{S}_{22} = 0$. The numerical implementation of the CH model is included in Appendix D.

Chapter 4

Results

The macroscopic behavior and underlying micromechanics of deformation were found to depend strongly upon the following factors: (1) assumed particle distribution, (2) matrix morphology, (3) volume fraction of modifier and (4) level of applied triaxiality. Each factor is discussed separately below, where results are presented in terms of the macroscopic stress-strain response of the RVE models, as well as local deformation mechanisms such as progression of matrix plastic straining with applied macroscopic strain. In view of the large number of combinations of cell and matrix material models, an acronym and icon based lexicon is given in Table 4.1.
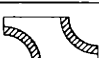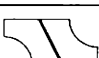
Model Description	Acronym	Icon
Regular Array-Isotropic Matrix model	RA-IM	
Regular Array-Anisotropic Matrix model	RA-AM	
Staggered Array-Isotropic Matrix model	SA-IM	
Staggered Array-Anisotropic Matrix model	SA-AM	
Staggered Array-Partially Anisotropic Matrix model	SA-PAM	
Alternative Staggered Array-Isotropic Matrix model	SAb-IM	
Alternative Staggered Array-Anisotropic Matrix model	SAb-AM	

Table 4.1: Table of acronyms and icons.

4.1 Effect of particle distribution

Numerous studies have explored the deformation of materials containing particles arranged in regular arrays (RA). Even though the deformation of such model materials is well-understood, its main features are summarized here to serve as a comparison basis to the more realistic SA distribution. In order to isolate the effect of particle distribution from other important issues addressed in this study, the results presented in this section regard a model material with a fully isotropic PA-6 matrix deforming in simple tension (the case of $f_0 = 20\%$ is presented). Figures 4-1 (a)-(c) depict contour plots of equivalent plastic strain rate normalized by the macroscopically applied strain rate, $\dot{\epsilon}^p_{eq}/\dot{\overline{E}}_{eq}$, where $\overline{E}_{eq} = 2/3 \, |\overline{E}_{zz} - \overline{E}_{rr}|$, at different macroscopic axial strains, $\overline{E}_{zz}$, and thus illustrate the progression of active plastic deformation in the RA model material. As can be seen, owing to the particle stress concentration effect (Goodier, 1933), plasticity in the RA model initiates at the particle interface along its equatorial plane. Then, after small amounts of applied strain, the deforming material has sufficiently strain-hardened such that the regions located along the main cell diagonals begin to plastically deform, starting from the cell boundary and proceeding

inward towards the particle. As deformation proceeds further, the entire axial ligament between particles actively deforms, since symmetry forces the lateral boundary of the cell to displace uniformly in the radial direction. This axial plastic thinning of interparticle regions dominates the deformation from that point on, while regions located near the poles of the particle barely deform. Concluding, particle interactions in the RA model occur mainly along transverse directions, while the influence of neighbors located above and below the equatorial planes of particles is hardly felt during loading. Clearly, these predicted patterns of deformation are rather simplified and do not capture important modes of deformation such as interparticle shearing of the matrix.

In an effort to correct this weakness of the RA model, a second more realistic staggered array (SA) particle distribution was modeled. In the SA approach, the modifying particles are positioned in a nested configuration, where, owing to the new assumed symmetries, they are allowed to shear relative to each other under macroscopically applied tensile loading. This effect is demonstrated in Figs 4-2 (a)-(c), where plasticity is shown to still initiate at the particle equator, due to the stress concentration effect, but to proceed very differently. In the SA model, plastic deformation concentrates in pronounced broad bands that bridge neighboring particles, indicating interparticle matrix shear. In addition, a rotation of the lateral boundary indicates relative motion of the modifying particles. This combination of events persists up to $\approx$ 20% axial strain and has a dramatic effect on the mechanical response of the material as shown in Fig. 4-3. The ability of the SA model to stretch via interparticle matrix shear and relative motion of particles results in a much softer overall response than that of the RA model. This difference in behavior starts to diminish at large macroscopic strain levels ($>$ 20%).

Almost identical patterns of deformation with the SA-IM model, are observed locally in the case of the SAb-IM model (see Figs 4-4 (a)-(c)). In addition, both models predict the same overall mechanical response for the SA model material (see Fig. 4-5). Thus, although none of the axisymmetric SA models is space-filling, the fact that they both predict identical results reinforces their value in studying three-
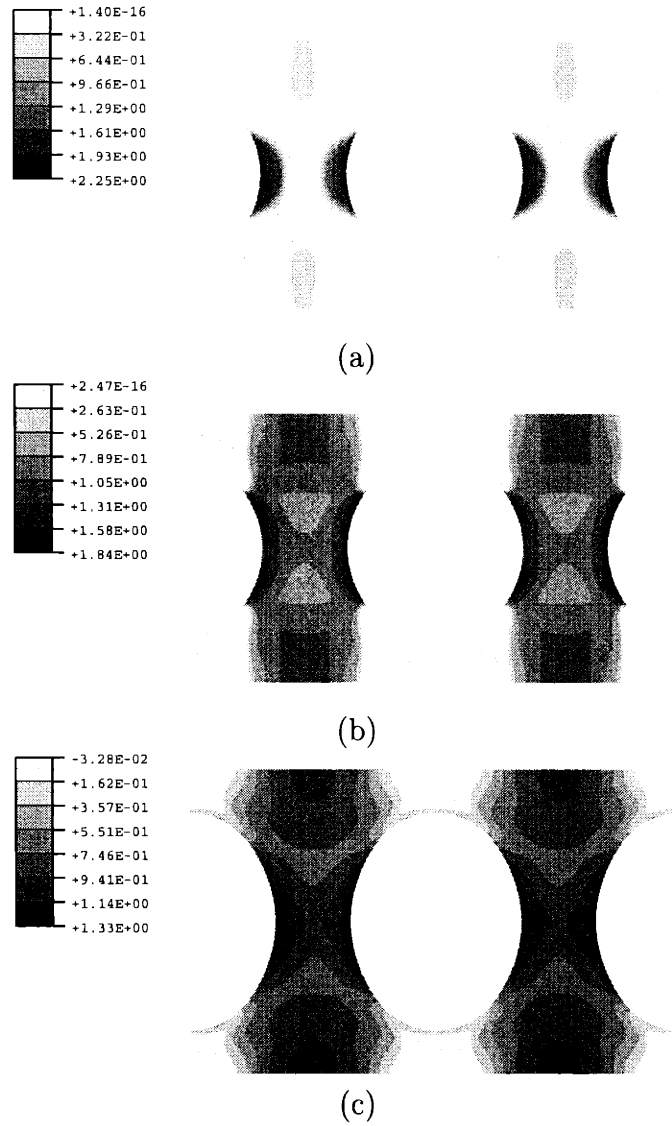
Figure 4-1: RA-IM model in simple tension (f_0 = 20%). Normalized equivalent plastic strain rate, $\dot{\epsilon}^p_{eq}/\overline{E}_{eq}$, at: (a) $\overline{E}_{zz}$= 0.02; (b) $\overline{E}_{zz}$=0.03; (c) $\overline{E}_{zz}$=0.15.

+1.87E-17
+4.94E-01
+9.88E-01
+1.48E+00
+1.98E+00
+2.47E+00
+2.96E+00
+3.46E+00

(a)

+2.36E-17
+4.45E-01
+8.90E-01
+1.34E+00
+1.78E+00
+2.23E+00
+2.67E+00
+3.12E+00

(b)

-4.43E-02
+2.17E-01
+4.77E-01
+7.38E-01
+9.99E-01
+1.26E+00
+1.52E+00
+1.78E+00

(c)

Figure 4-2: SA-IM model in simple tension ($f_0 = 20\%$). Normalized equivalent plastic strain rate, $\dot{\epsilon}^p_{eq}/\overline{\dot{E}}_{eq}$, at: (a) $\overline{E}_{zz}$= 0.02; (b) $\overline{E}_{zz}$=0.03; (c) $\overline{E}_{zz}$=0.15.
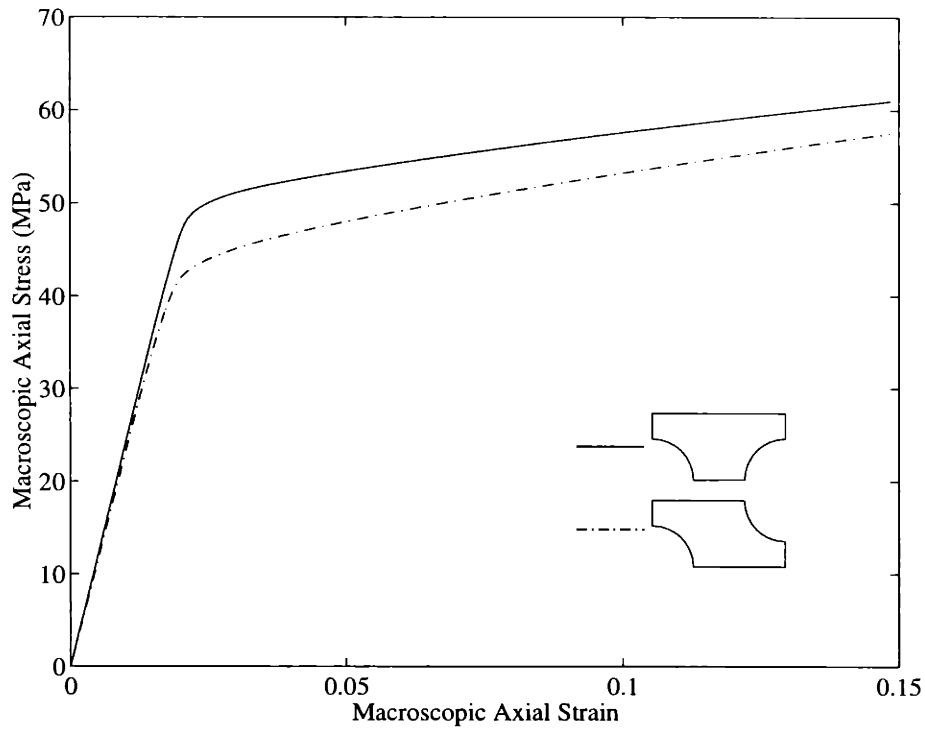
Figure 4-3: Macroscopic axial stress, $\overline{T}_{zz}$ (MPa) vs. macroscopic axial strain, $\overline{E}_{zz}$ for isotropic matrix, but differing RVE models ($f_0 = 20\%$).

dimensional heterogeneous material systems.

In summary, it is found that the assumed particle distribution plays an important role on the predicted deformation behavior of heterogeneous materials for up to significantly high strains. Thus, while the RA model is a good first approach, more physically representative RVE models such as the SA and SAb models provide a more realistic picture of the underlying micromechanics. Finally, the assumptions made in reducing the three-dimensional model material to a two-dimensional representative structure are justified by the fact that both SA and SAb models predict identical results.

Figure 4-4: SAb-IM model in simple tension ($f_0 = 20\%$). Normalized equivalent plastic strain rate, $\dot{\epsilon}^p_{eq}/\overline{\dot{E}}_{eq}$, at: (a) $\overline{E}_{zz}= 0.02$; (b) $\overline{E}_{zz}=0.03$; (c) $\overline{E}_{zz}=0.15$.
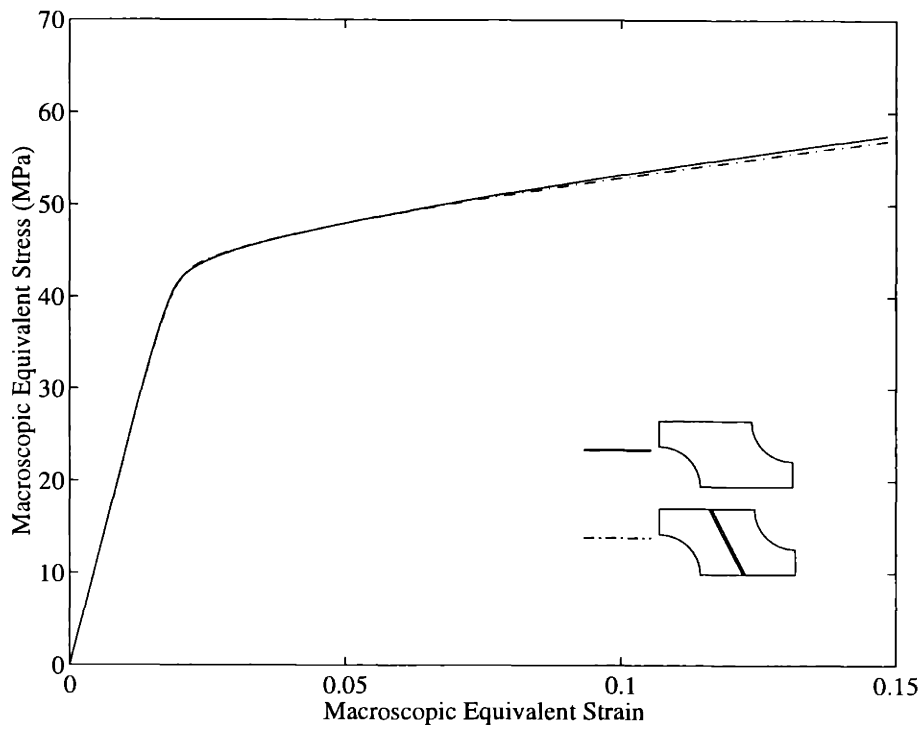
Figure 4-5: Macroscopic axial stress, $\overline{T}_{zz}$ (MPa) vs. macroscopic axial strain, $\overline{E}_{zz}$ for isotropic matrix, but differing SA models ($f_0 = 20\%$).

4.2 Effect of matrix morphology

In this section, the effect of reducing the average interparticle ligament thickness, Λ, below Λ_c is explored in both RVE models deforming in simple tension. Experimentally, the average interparticle distance in a blend can be reduced either by increasing the modifier content at fixed particle size, or by decreasing the particle size at fixed modifier volume fraction. In this study, the latter effect was captured by changing the constitutive behavior of the matrix material at constant volume fraction of modifier. In this section, the case of f_0=20% is used. Three cases of matrix texture were considered: one case considered the interface-induced texture to percolate through the entire matrix and is referred to as the Anisotropic Matrix (AM) model; the second case considered the opposite extreme where the amount of oriented matrix material is negligible and is referred to as the Isotropic Matrix (IM) model; and the third case considered the anisotropic portion of the matrix to be significant, but it does not span the entire interparticle region (the specific case of 5 vol.% AM material is taken). This last texture is modeled by dividing the matrix into an anisotropic region and an isotropic one, and is therefore, termed the Partially Anisotropic Matrix (PAM) model. The macroscopic mechanical response and local modes of plastic deformation of the RA, SA, SAb-IM models were discussed in the previous section. Here the deformation behavior of the RA, SA, SAb-AM and SA-PAM models is compared to the deformation behavior of the IM models. The effect of Hill ratios on the predicted overall mechanical response of the models is also studied.

4.2.1 Anisotropic Matrix (AM) models vs. Isotropic Matrix (IM) models

Figures 4-6 (a)-(c) illustrate the evolution of matrix plasticity in the RA-AM model, where $\dot{\epsilon}^p_{eq} = \mathbf{T} \cdot \dot{\epsilon}^p / \sigma_{BY}$. As can be seen, rather than at the particle equator, plasticity in the AM model initiates along distinct diagonal bands. These bands form in regions where the shear strength of the material is lowered by preferential orientation of the "easy-shear" slip systems of the matrix material, with respect to the loading

63

Figure 4-6: RA-AM model in simple tension ($f_0 = 20\%$). Normalized equivalent plastic strain rate, $\dot{\epsilon}^p_{eq}/\dot{\overline{E}}_{eq}$, at: (a) $\overline{E}_{zz}$=0.02; (b) $\overline{E}_{zz}$=0.03; (c) $\overline{E}_{zz}$=0.15.
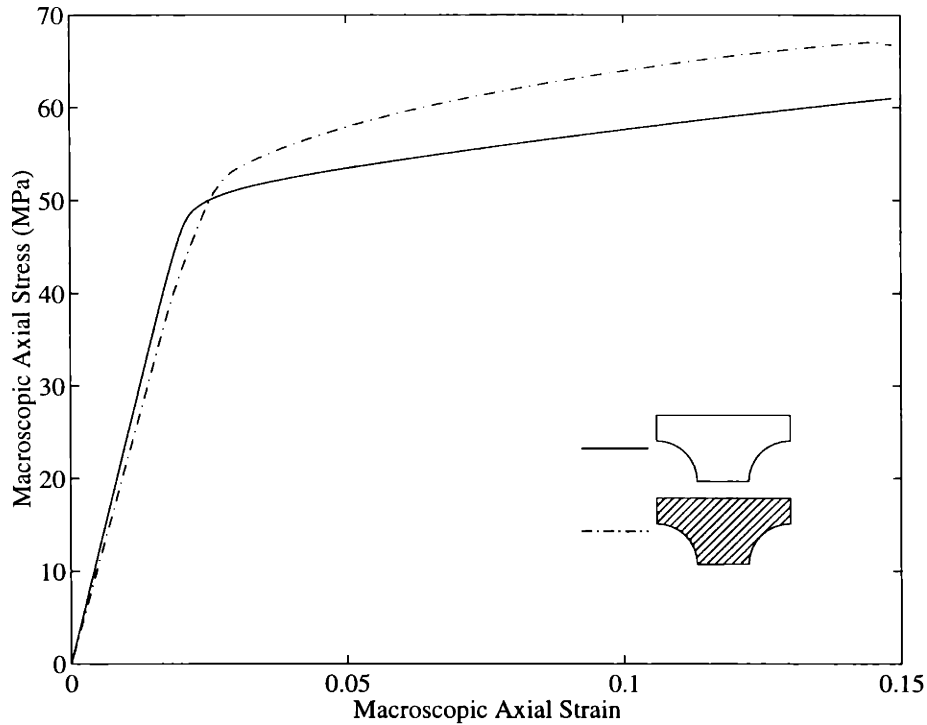
Figure 4-7: Macroscopic axial stress, $\overline{T}_{zz}$ (MPa) vs. macroscopic axial strain, $\overline{E}_{zz}$ for RA models, of both isotropic and oriented matrix material ($f_0 = 20\%$).

axis. Moreover, owing to the void's inability to transmit shear, they form away from the interface. Due to the constraints of the RA cell geometry [1], plasticity then propagates into the "hard-to-deform" equatorial regions of the matrix below the yielded diagonals. As a result, the overall mechanical response predicted by the RA-AM model is significantly stronger than that predicted by the RA-IM model (see Fig. 4-7). While this predicted behavior appears at first to be in direct contradiction with experimental observations: namely, Muratoglu et al. (1995b) observed a 10 % decrease in the overall strength of PA-6,6 blends and no subsequent hardening when Λ was reduced below Λ_c, it will be shown that these predictions are artificial and mostly a consequence of the unrealistic constraints of the RA model.

Figures 4-8 (a)-(c) illustrate the evolution of matrix plasticity in the SA-AM model. For reasons similar to those discussed in the case of the RA-AM model, plas-

---

[1]The RA model deforms primarily through axial plastic thinning of interparticle ligaments.

| -1.58E-01 |
| +1.23E+00 |
| +2.63E+00 |
| +4.02E+00 |
| +5.41E+00 |
| +6.80E+00 |
| +8.19E+00 |
| +9.58E+00 |

(a)

| -5.23E-01 |
| +5.91E-01 |
| +1.70E+00 |
| +2.82E+00 |
| +3.93E+00 |
| +5.04E+00 |
| +6.16E+00 |
| +7.27E+00 |

(b)

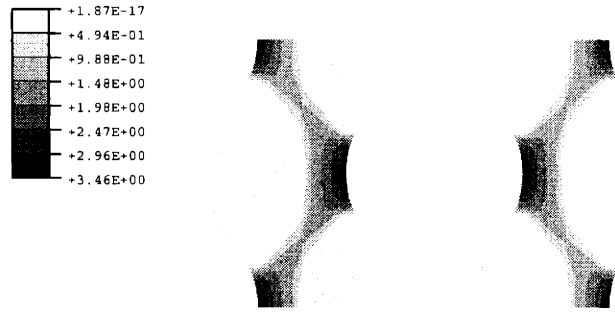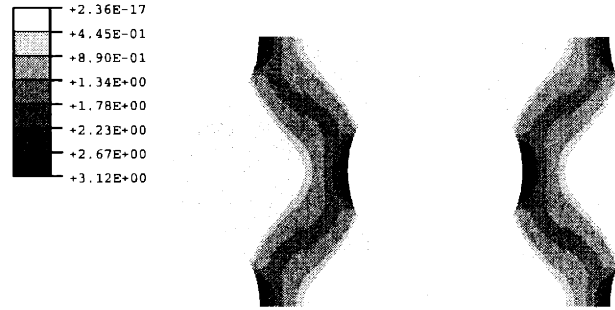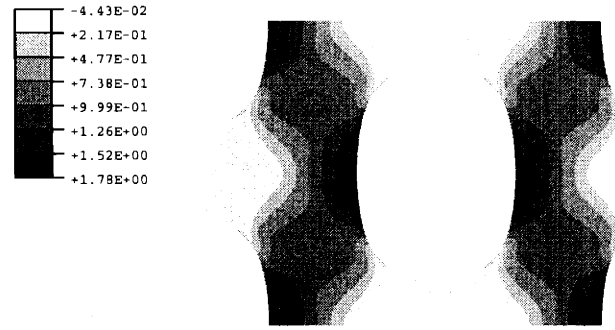| -7.69E-01 |
| +2.38E-01 |
| +1.25E+00 |
| +2.25E+00 |
| +3.26E+00 |
| +4.27E+00 |
| +5.27E+00 |
| +6.28E+00 |

(c)
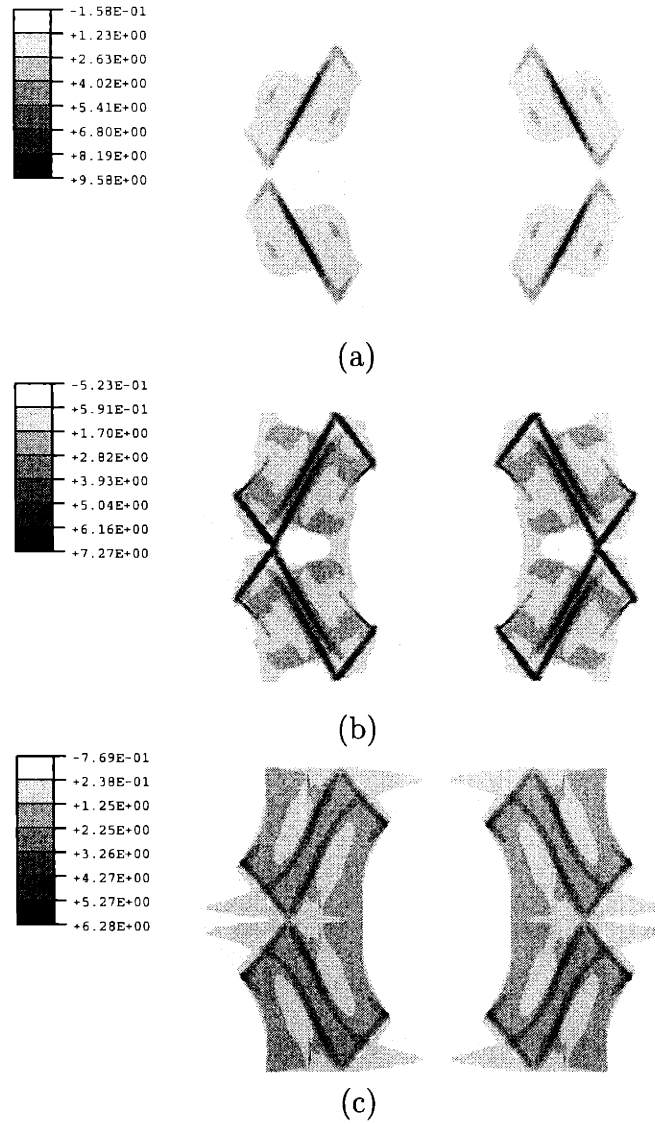
Figure 4-8: SA-AM model in simple tension ($f_0 = 20\%$). Normalized equivalent plastic strain rate, $\dot{\epsilon}^p_{eq}/\overline{\dot{E}}_{eq}$, at: (a) $\overline{E}_{zz}$=0.02; (b) $\overline{E}_{zz}$=0.03; (c) $\overline{E}_{zz}$=0.15.

tic deformation in the SA-AM model initiates in the matrix material diagonally away from the particle interface, forming distinct multiple shear bands. These bands originally develop midway between nearest neighboring particles along directions perpendicular to lines connecting their centers, and then propagate in the form of multiple parallel shear bands. As in the case of the SA-IM model, these deformation patterns indicate relative motion of the modifying particles via interparticle matrix shear; however, matrix shearing occurs in a substantially different way. In the SA-IM model, relative motion of particles concentrates plastic deformation in ever-broadening bands that bridge nearest neighbors. In contrast, in the SA-AM model, deformation is accommodated by distinct shearing of the matrix material along specific crystallographic planes. While plasticity in the SA-AM model eventually percolates to the "hard-to-deform" equatorial regions of particles, the ability of the model to sustain deformation within the preferentially-oriented material causes its macroscopic mechanical response to almost never rise above that corresponding to the SA-IM model (see Fig. 4-11). Rather, the overall mechanical behavior of the two models is very similar with the exception of the slightly reduced elastic stiffness in the AM material.

The patterns of deformation predicted by the SA-AM model are verified by the SAb-AM model as shown in Figs 4-9 (a)-(c). The predictions of both SA models are almost identical with the exception of early on in the deformation; where the SAb model yields near the equator of the particle and in the region of lowered shear resistance simultaneously. This results in a slightly stronger overall mechanical response of the SAb model, a difference that diminishes with increasing deformation (see Fig. 4-10).

4.2.2 Anisotropic Matrix (AM) models vs. Partially Anisotropic Matrix (PAM) models

A combination of the deformation patterns observed in the SA-AM and SA-IM simulations is observed in the case of the SA-PAM model. Namely, similarly to the SA-AM model, plastic deformation in the anisotropic portion of the matrix initiates away from

```
 -1.79E-01
 +3.94E-01
 +9.68E-01
 +1.54E+00
 +2.11E+00
 +2.69E+00
 +3.26E+00
 +3.83E+00
```

(a)

```
 -1.63E+00
 -1.95E-01
 +1.24E+00
 +2.68E+00
 +4.12E+00
 +5.56E+00
 +7.00E+00
 +7.66E+00
```

(b)

```
 -4.41E-01
 +6.32E-01
 +1.71E+00
 +2.78E+00
 +3.85E+00
 +4.93E+00
 +6.00E+00
 +1.85E+01
```
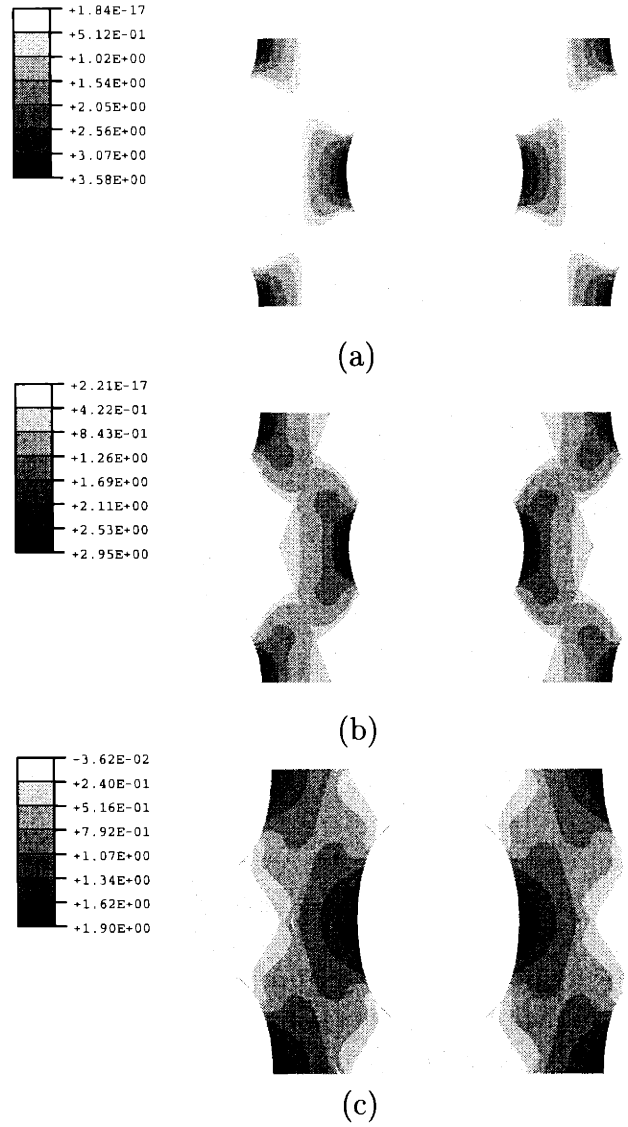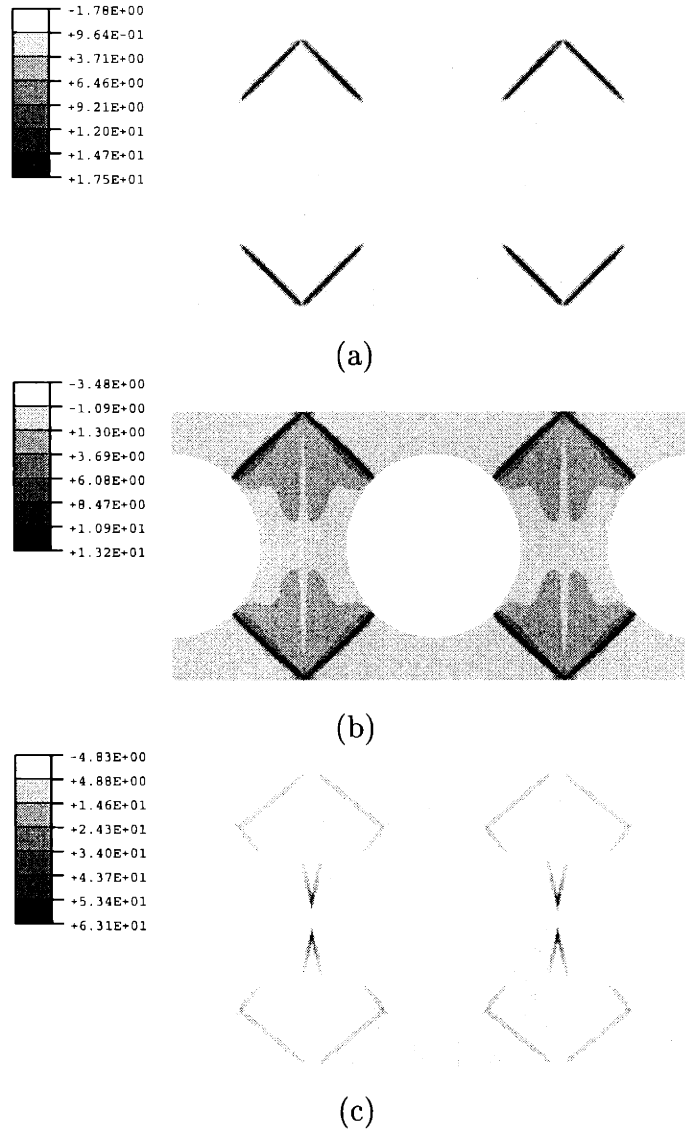
(c)

Figure 4-9: SAb-AM model in simple tension ($f_0 = 20\%$). Normalized equivalent plastic strain rate, $\dot{\epsilon}^p_{eq}/\overline{E}_{eq}$, at: (a) $\overline{E}_{zz}$=0.02; (b) $\overline{E}_{zz}$=0.03; (c) $\overline{E}_{zz}$=0.15.

68
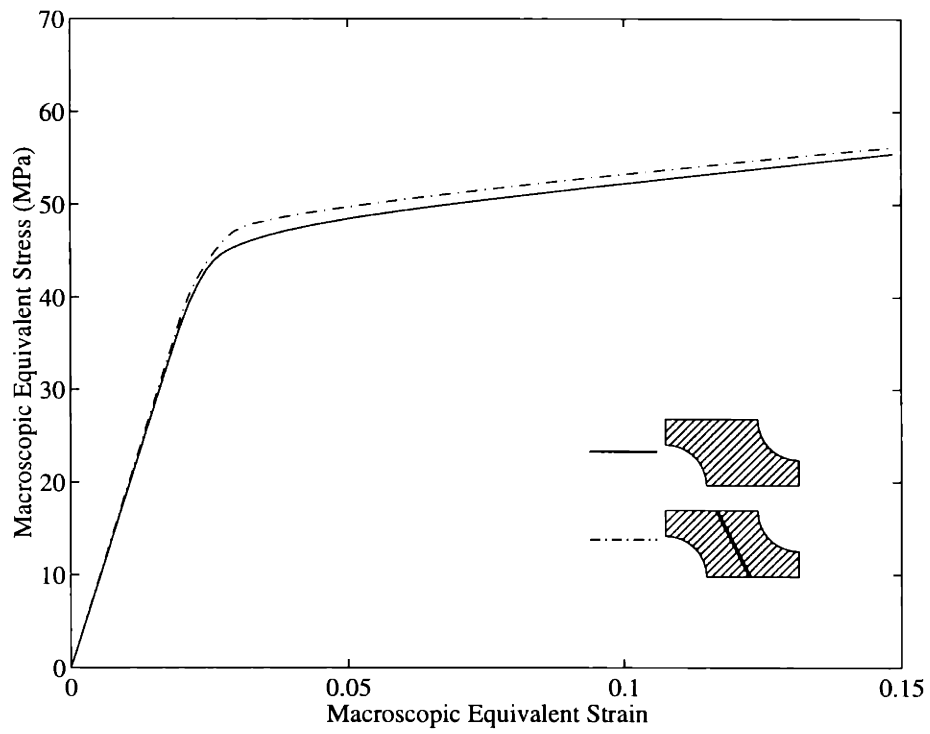
Figure 4-10: Macroscopic axial stress, $\overline{T}_{zz}$ (MPa) vs. macroscopic axial strain, $\overline{E}_{zz}$ ($f_0 = 20\%$).

the interface, and propagates along directions perpendicular to lines connecting the centers of neighboring particles through multiple shear bands. Simultaneously, plasticity in the isotropic portion initiates at the particle equator and propagates through a single broad band, bridging neighboring particles. The net effect of such a combination on the macroscopic mechanical response of the material is rather unexpected. Namely, because shear initiating in the preferentially oriented region of the anisotropic portion of the matrix cannot propagate into the isotropic region, it instead propagates into the "hard-to-deform" equatorial regions of the anisotropic matrix earlier on in the deformation. As a result, the effect of the anisotropic skin layer is that of a stiff shell that does not allow the particle surface to deform (i.e., the voids behave almost like rigid particles). This results in a rise of the macroscopic flow stress levels of the cell above that of the SA-IM and SA-AM models (see Fig. 4-11). In other words, when Λ is sufficiently larger than Λ_c, the yield strength of a material blended with a softer secondary phase may potentially be higher than that of the unmodified material! This effect diminishes as the amount of preferentially-oriented matrix material increases. Indeed, Dijkstra (1993), has experimentally observed this peculiar effect, whereby the strength of PA-6 <u>increases</u> when a small amount of an elastomeric secondary phase is blended in the material. Since Muratoglu et al. (1995b) did not report the yield strength of the isotropic material, the drop in yield strength that they observed upon reaching $\Lambda \leq \Lambda_c$, in blends of identical filler particle volume fraction, is potentially relative to the strength of blends with widely spaced particles. While such a drop in strength may accompany the toughness jumps in PAs, other semicrystalline polymers that are effectively toughened when $\Lambda \leq \Lambda_c$, for instance HDPE, do not exhibit such a drop (Bartczak et al., 1999b) [2]. Consequently, its effect in toughening is secondary, while the easy interparticle shear discussed here is mostly responsible for the jumps.

---

[2]The crystalline component of HDPE is not as anisotropic as that of PAs. Thus, the effect of a thin layer of highly oriented material, surrounding secondary phase soft inclusions in modified HDPE, on the macroscopic mechanical response of the blend might not be as dramatic.
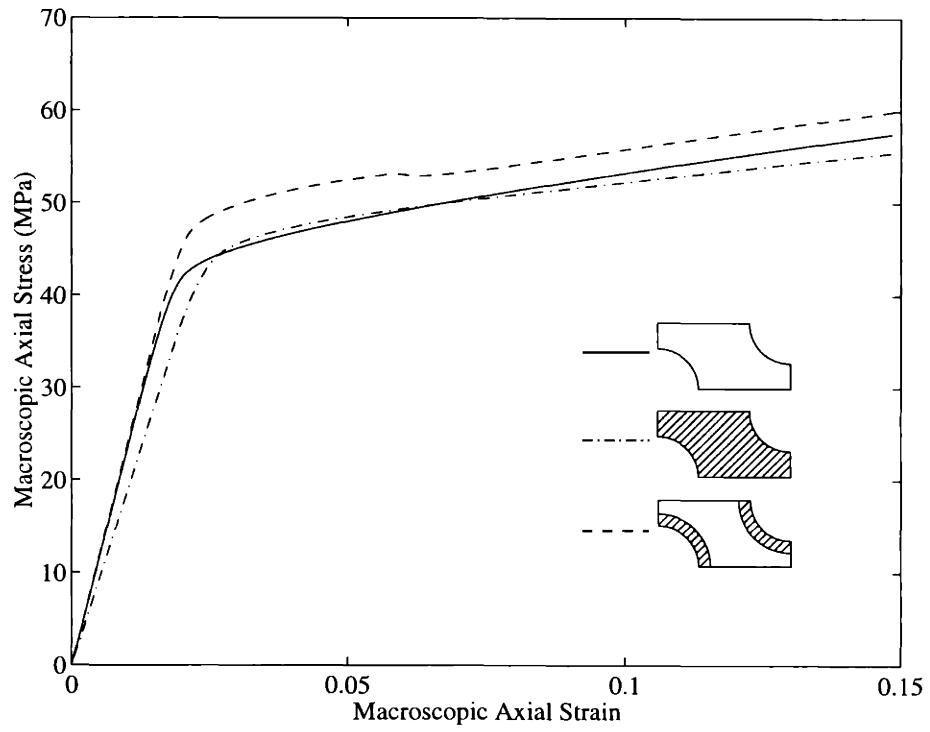
Figure 4-11: Macroscopic axial stress, $\overline{T}_{zz}$ (MPa) vs. macroscopic axial strain, $\overline{E}_{zz}$ for SA model, but differing amounts of oriented material ($f_0 = 20\%$).

4.2.3 Sensitivity study on the effect of Hill ratios on the predicted deformation behavior of the blends

Since the accuracy of the determined anisotropy is difficult to assess, a sensitivity study on the effect of Hill ratios on the predicted deformation behavior of the SA blends was conducted to rule out misleading results [3]. Figure 4-12 depicts the effect of varying R_{11} on the predicted overall response of the blends; where it is clear that the value of R_{11} used in the simulations has no effect on the results. Figure 4-13 depicts the effect of varying $R_{22} = R_{33}$. As can be seen, this parameter has a dramatic effect on the predicted flow stress levels; where increasing its value results in an increase of the overall flow stress. Figure 4-14 depicts the effect of varying $R_{12} = R_{13}$. Similarly to $R_{22} = R_{33}$, this parameter appears to control the predicted macroscopic flow stress levels. In conclusion, results are mostly sensitive to the value of $R_{22} = R_{33}$ and $R_{12} = R_{13}$, and consequently, these parameters must be chosen carefully.

4.3 Effect of volume fraction

The local deformation mechanisms observed in each case: RA-IM, SA, SAb-IM, RA-AM, and SA, SAb-AM were found to be independent of filler volume fraction (see Figs 4-15 (a)-(c), 4-16 (a)-(c), 4-17 (a)-(c) and 4-18 (a)-(c)). However, with decreasing matrix material, the succession of local deformation events is accelerated in each case. The overall trend in mechanical response dependence on filler volume fraction is also the same in each case. Figures 4-19 and 4-20 illustrate this trend, comparing the stress-strain behavior for the RA-IM and AM, and SA-IM and AM cases, for $f_0 = 15$ and 25% respectively. In both assumed microstructures, increasing the volume fraction of modifier results in a decrease of the macroscopic flow stress levels of both IM and AM morphologies by approximately the same amount. However, since increasing the volume fraction of modifier decreases the amount of preferentially ori-

---

[3]Note that for simplicity, the elastic response of the material is taken to be isotropic in this sensitivity study.

72
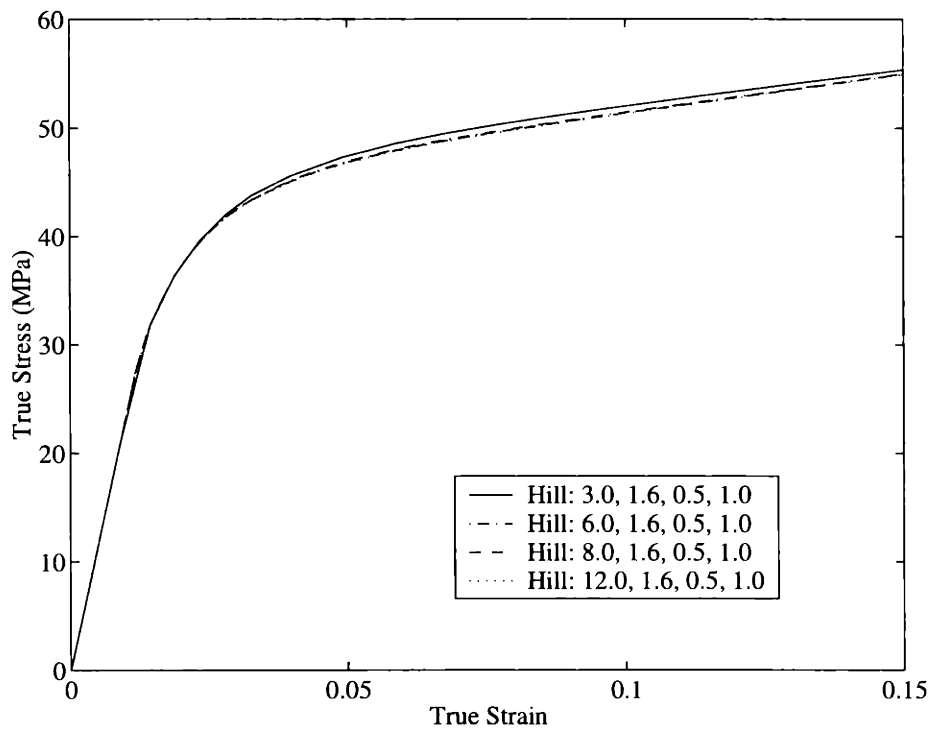
Figure 4-12: Effect of the value of R_{11} on the macroscopic stress-strain response of the SA model ($f_0 = 20\%$).
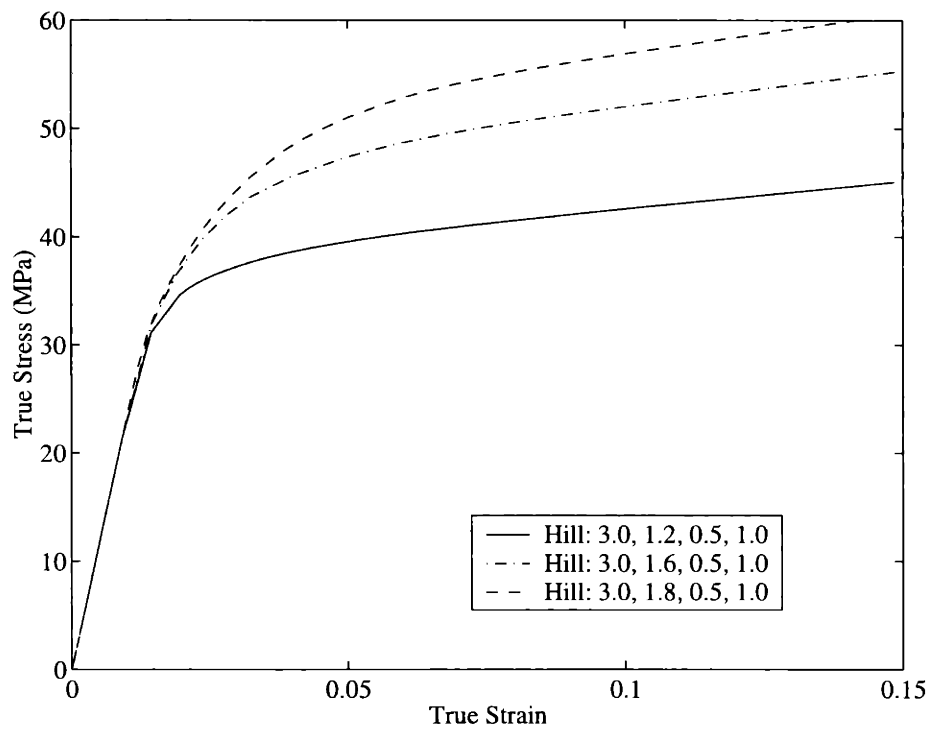
Figure 4-13: Effect of the value of $R_{22} = R_{33}$ on the macroscopic stress-strain response of the SA model ($f_0 = 20\%$).
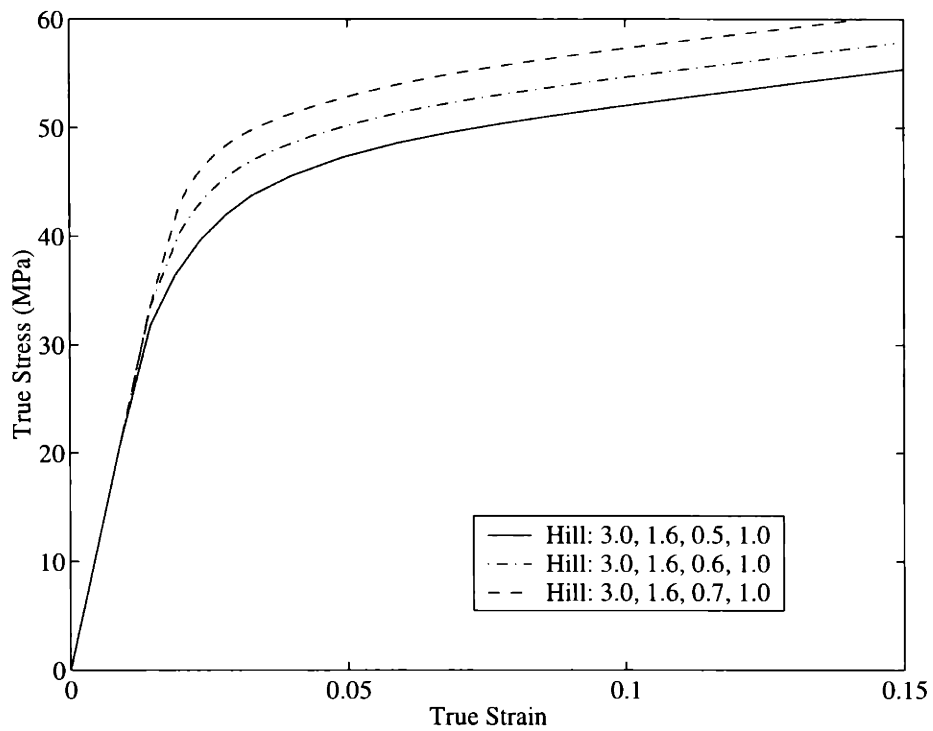
Figure 4-14: Effect of the value of $R_{12} = R_{13}$ on the macroscopic stress-strain response of the SA model ($f_0 = 20\%$).

ented material, the drop in strength of the AM models is smaller than that for the IM models, with increasing filler volume fraction.

4.4   Effect of Triaxiality

As mentioned earlier, it is only in the presence of high triaxiality that the normally quite tough PAs lose their toughness. Consequently, it is important to study their behavior under triaxial loading conditions. Since the SA model has been shown to more realistically capture the deformation of particle-filled PAs, the effects of triaxiality are explored here only with the SA models. Figure 4-21 depicts the overall deviatoric strength, of the SA-IM model under different levels of triaxiality, where the level of triaxiality is indicated using the triaxiality parameter, Σ. Moreover, Fig. 4-22 depicts the volumetric response of the material, $\overline{E}_{kk} = 2\overline{E}_{zz} + \overline{E}_{rr}$, as a function of macroscopic equivalent strain. A pronounced softening of the deviatoric strength of the material is observed with increasing triaxiality, a well-known behavior in porous plasticity of isotropic materials (Gurson, 1977). In addition, the macroscopic volumetric strain increases, indicating that the SA-IM model deforms through void growth and tensile stretching.

In the corresponding plots contouring normalized equivalent plastic strain increment, $\dot{\epsilon}^p_{eq}/\overline{\dot{E}}_{eq}$ for the SA-IM model, the same patterns of plastic deformation are observed to evolve in the matrix, independently of Σ. However, as triaxiality increases the broadening of the interparticle shear bands appears to happen earlier on in the deformation (see Figs 4-23 (a)-(c)). In contrast, the deviatoric strength of the SA-AM model is surprisingly unaffected by triaxiality, while the macroscopic volumetric strain increases but not as dramatically as in the case of the SA-IM model (see Figs 4-24 and 4-25). In addition, shear banding in the matrix appears to become more intense with increasing triaxiality (see Figs 4-26 (a)-(c)). Concluding, the texture of the matrix in the SA-AM model acts to provide a nearly non-stretching shell around the particle that impedes volumetric expansion of the RVE, while still promoting shear via distinct highly localized shear bands under conditions of global triaxiality.
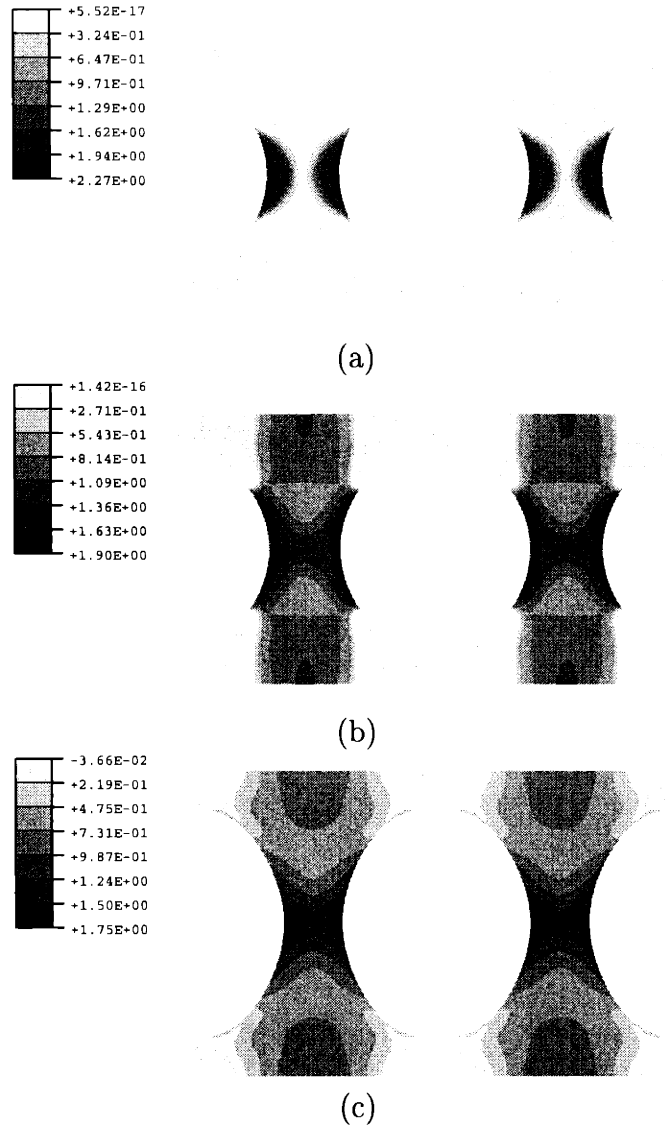
Figure 4-15: RA-IM model in simple tension ($f_0 = 25\%$). Normalized equivalent plastic strain rate, $\dot{\bar{\epsilon}}^p_{eq}/\overline{E}_{eq}$, at: (a) $\overline{E}_{zz}$=0.02; (b) $\overline{E}_{zz}$=0.03; (c) $\overline{E}_{zz}$=0.15.
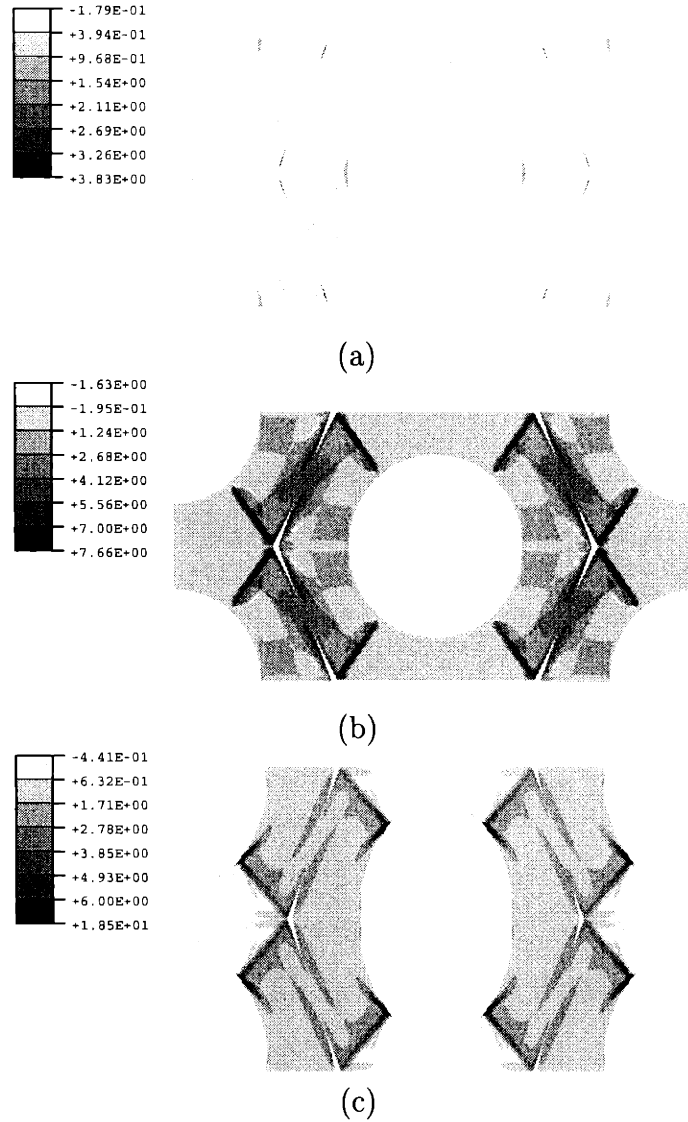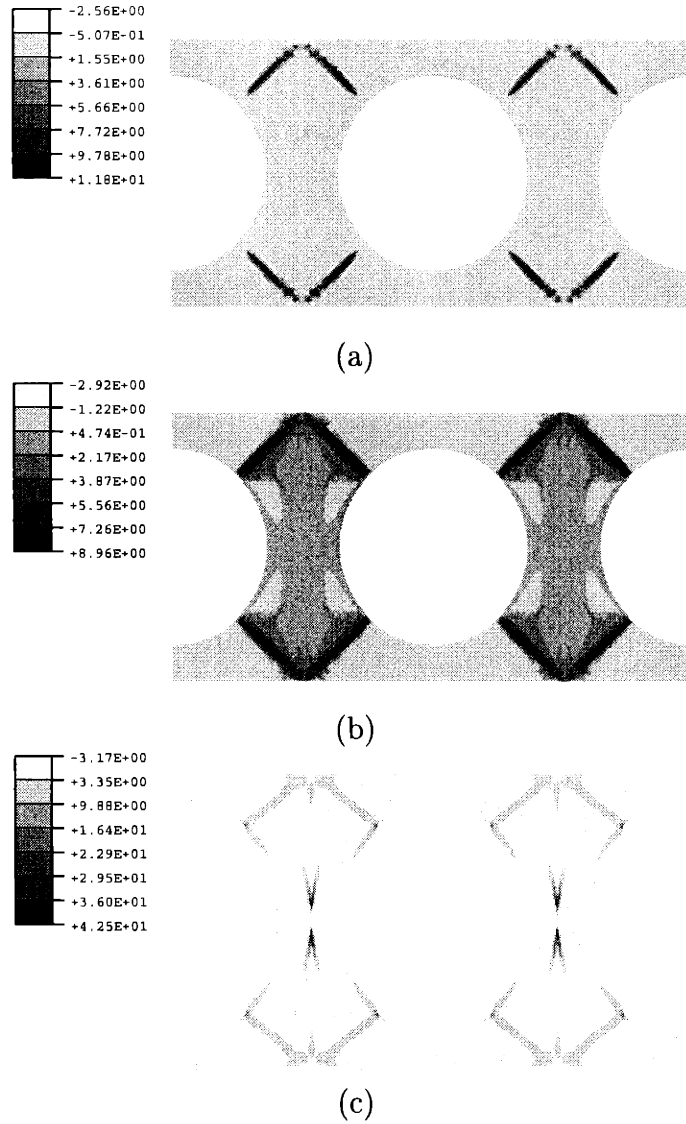
Figure 4-16: RA-AM model in simple tension ($f_0 = 25\%$). Normalized equivalent plastic strain rate, $\dot{\epsilon}^p_{eq}/\overline{\dot{E}}_{eq}$, at: (a) $\overline{E}_{zz}$=0.02; (b) $\overline{E}_{zz}$=0.03; (c) $\overline{E}_{zz}$=0.15.
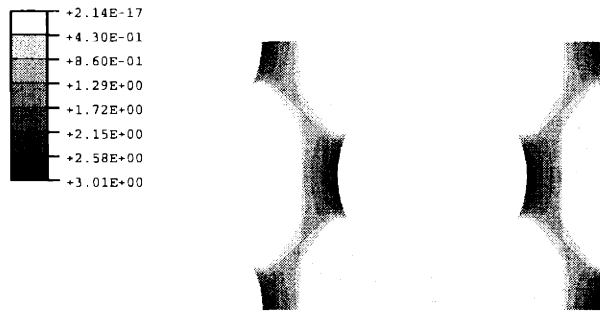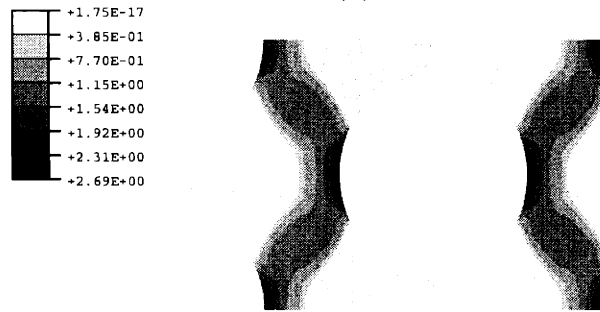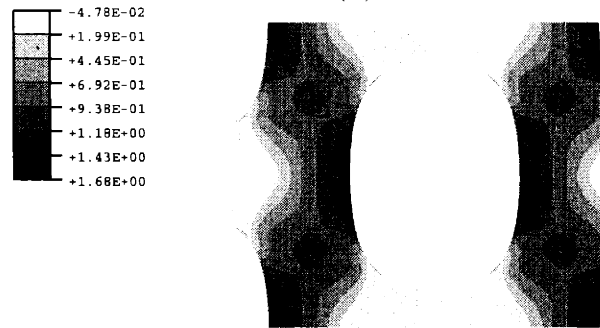
Figure 4-17: SA-IM model in simple tension ($f_0 = 25\%$). Normalized equivalent plastic strain rate, $\dot{\epsilon}^p_{eq}/\overline{E}_{eq}$, at: (a) $\overline{E}_{zz}$=0.02; (b) $\overline{E}_{zz}$=0.03; (c) $\overline{E}_{zz}$=0.15.
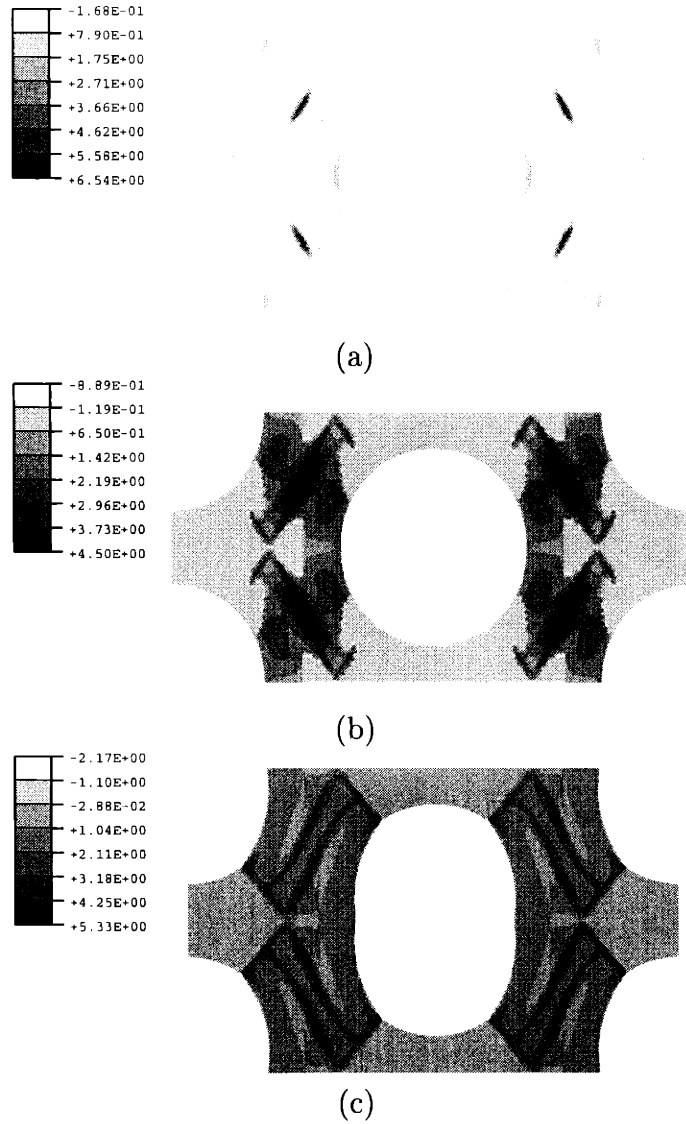
Figure 4-18: SA-AM model in simple tension ($f_0 = 25\%$). Normalized equivalent plastic strain rate, $\dot{\epsilon}^p_{eq}/\overline{E}_{eq}$, at: (a) $\overline{E}_{zz}$=0.02; (b) $\overline{E}_{zz}$=0.03; (c) $\overline{E}_{zz}$=0.15.
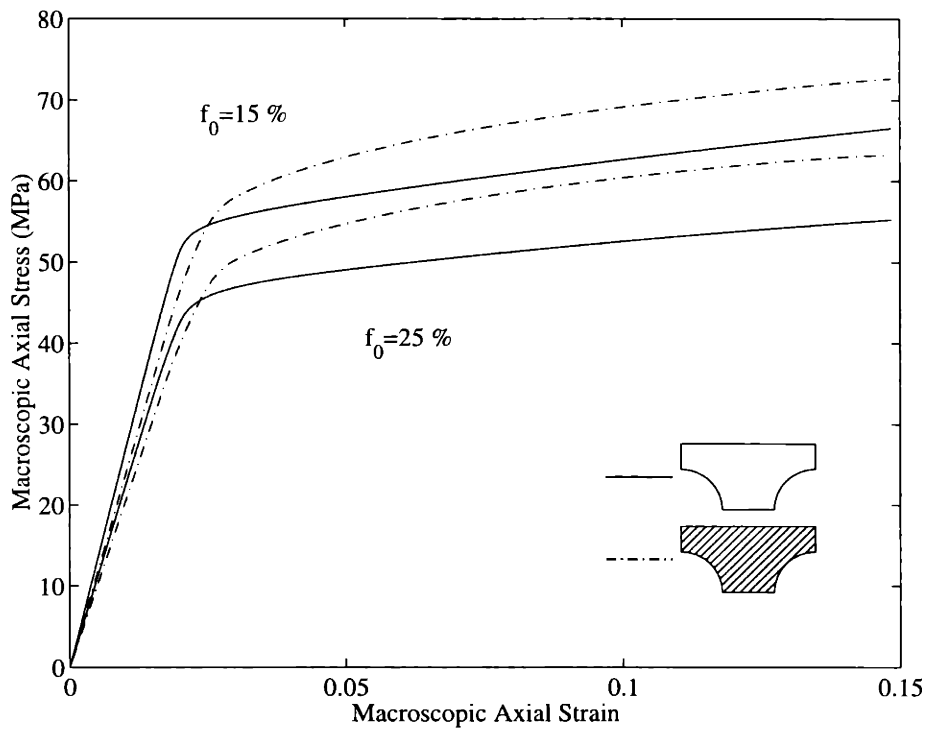
Figure 4-19: Effect of volume fraction of modifier on the macroscopic axial stress, $\overline{T}_{zz}$ (MPa) vs. macroscopic axial strain, $\overline{E}_{zz}$ curves predicted by the RA-IM and RA-AM models.
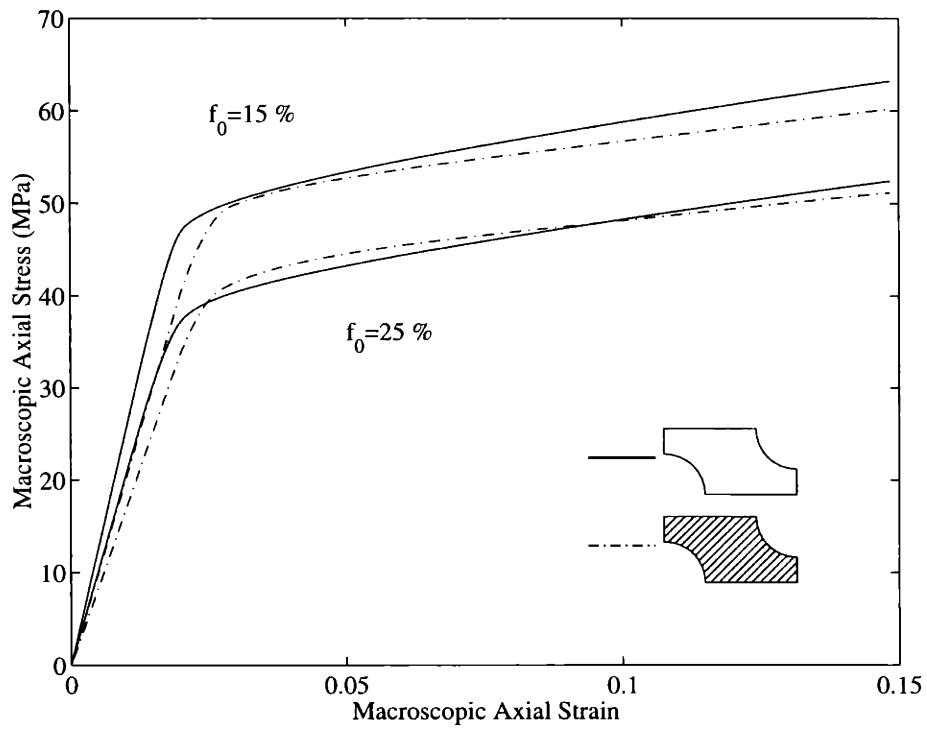
Figure 4-20: Effect of volume fraction of modifier on the macroscopic axial stress, $\overline{T}_{zz}$ (MPa) vs. macroscopic axial strain, $\overline{E}_{zz}$ curves predicted by the SA-IM and SA-AM models.
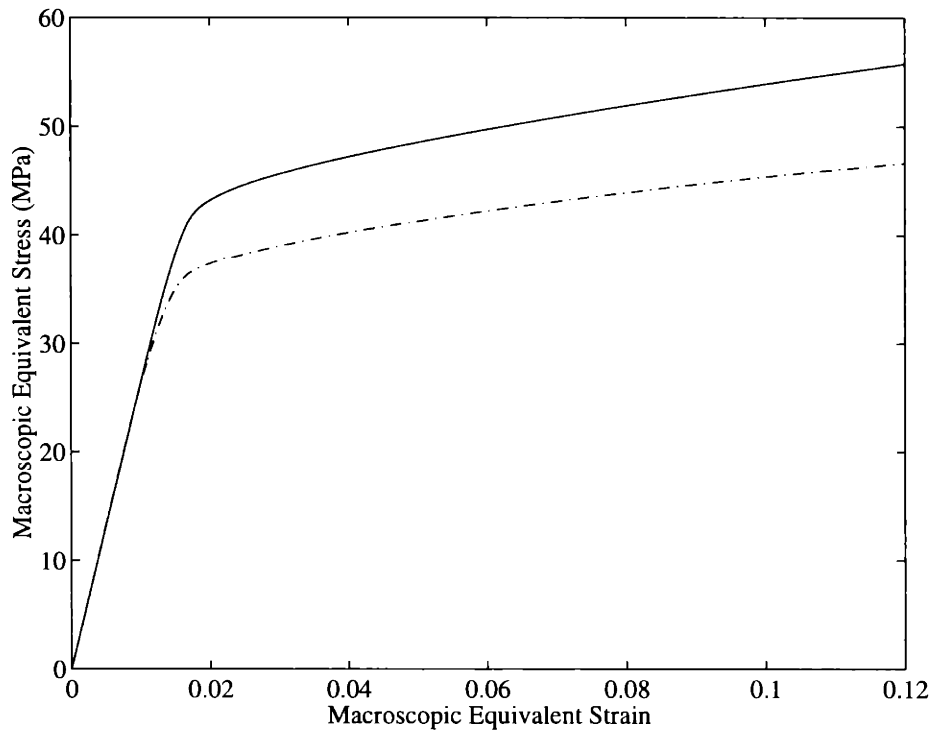
Figure 4-21: Staggered Array-Isotropic Matrix (SA-IM) model. Macroscopic equivalent stress, $\overline{T}_{eq}$ (MPa) vs. macroscopic equivalent strain, $\overline{E}_{eq}$ ($f_0 = 20\%$): (—) low triaxiality, $\Sigma = 0.33$; (- ·) elevated triaxiality, $\Sigma = 1.0$.
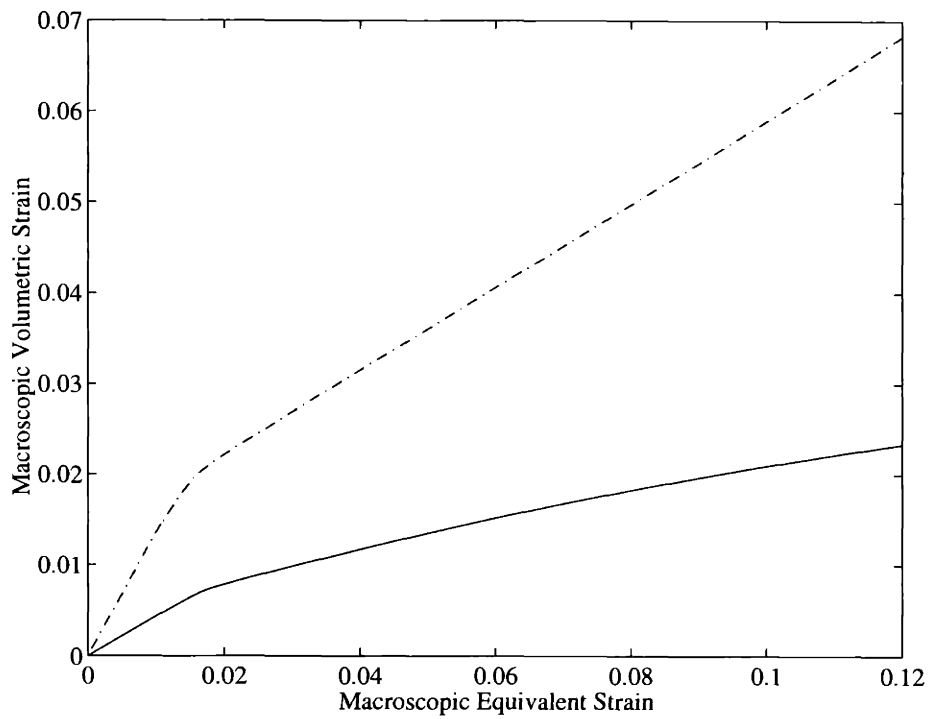
Figure 4-22: Staggered Array-Isotropic Matrix (SA-IM) model. Macroscopic volumetric strain, $\overline{E}_{kk}$ vs. macroscopic equivalent strain, $\overline{E}_{eq}$ ($f_0 = 20\%$): (—) low triaxiality, $\Sigma = 0.33$; (- ·) elevated triaxiality, $\Sigma = 1.0$.
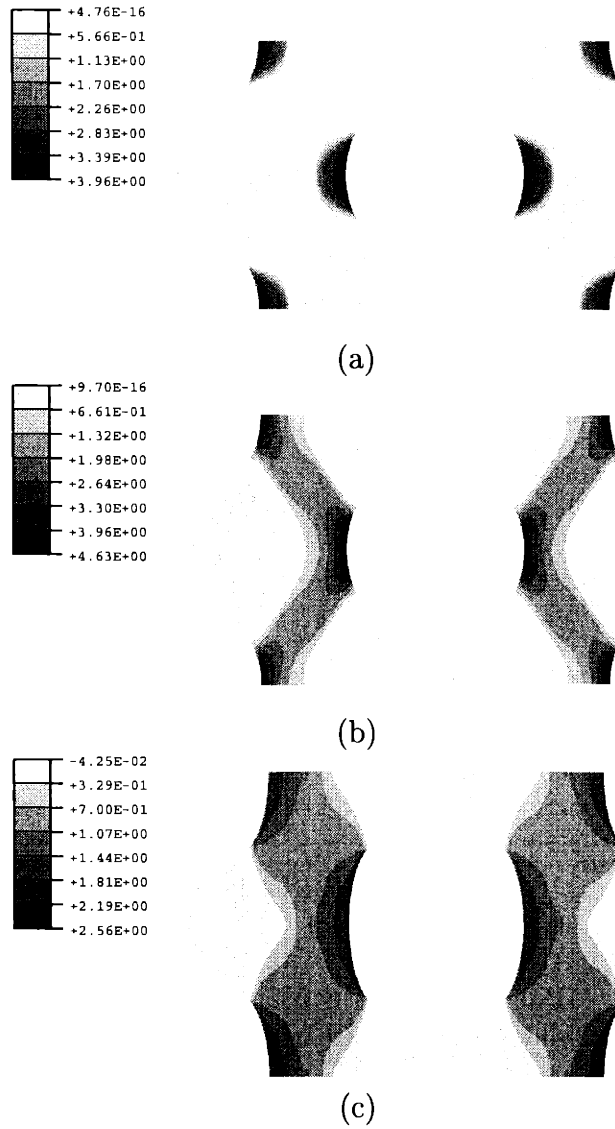
Figure 4-23: SA-IM model ($\Sigma = 1.0$). Normalized equivalent plastic strain rate, $\dot{\epsilon}^p_{eq}/\overline{E}_{eq}$, at: (a) $\overline{E}_{zz}$=0.02; (b) $\overline{E}_{zz}$=0.03; (c) $\overline{E}_{zz}$=0.15.
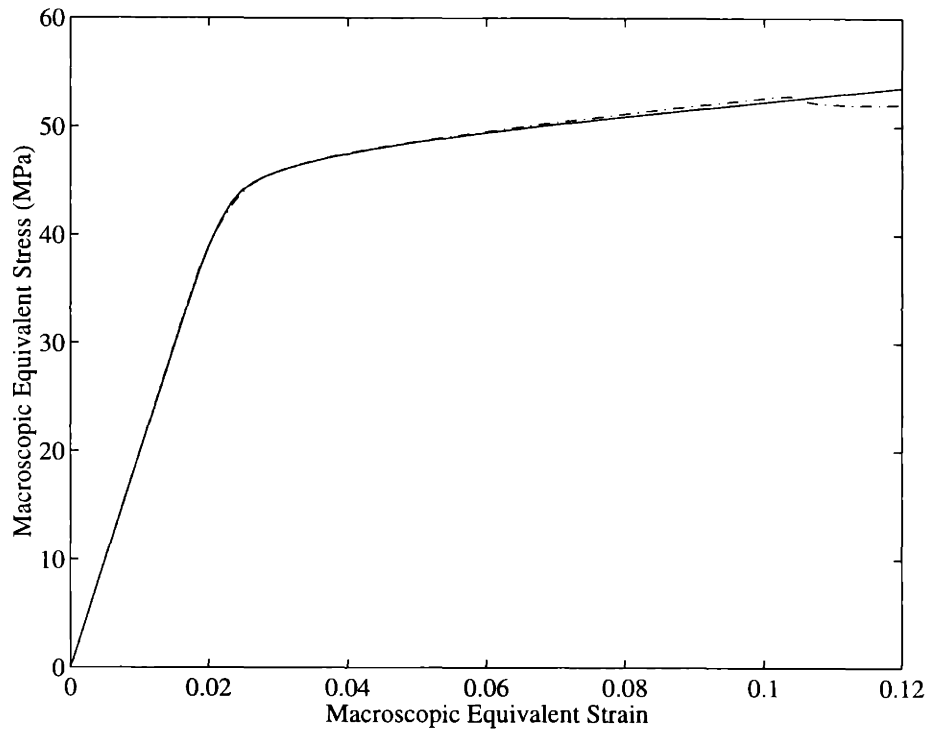
Figure 4-24: Staggered Array-Anisotropic Matrix (SA-AM) model. Macroscopic equivalent stress, $\overline{T}_{eq}$ (MPa) vs. macroscopic equivalent strain, $\overline{E}_{eq}$ ($f_0 = 20\%$): (—) low triaxiality, $\Sigma = 0.33$; (– ·) elevated triaxiality, $\Sigma = 1.0$.
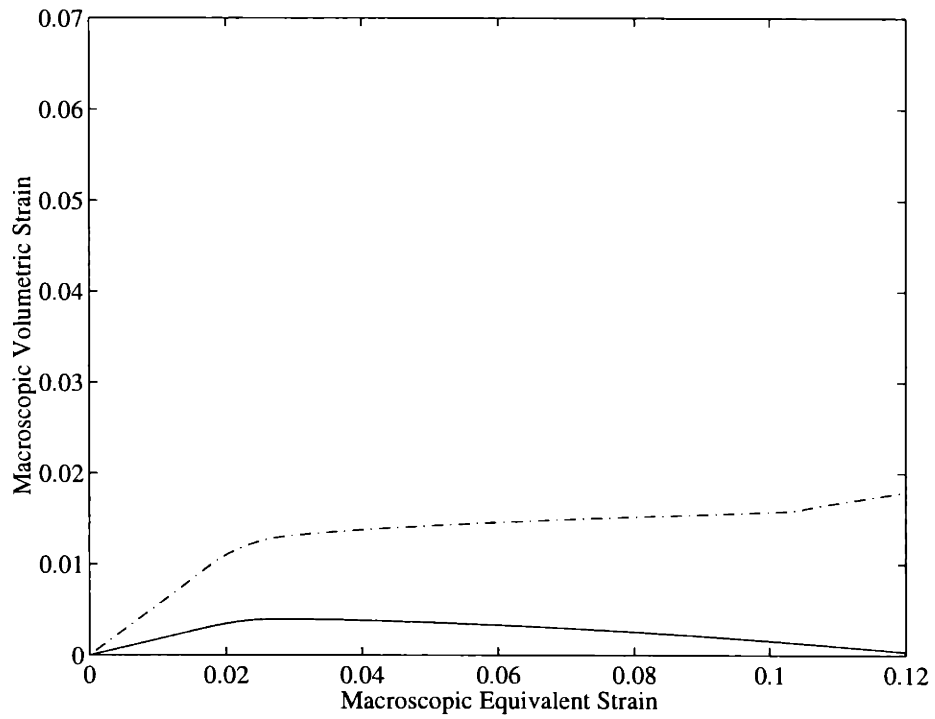
Figure 4-25: Staggered Array-Anisotropic Matrix (SA-AM) model. Macroscopic volumetric strain, $\overline{E}_{kk}$ vs. macroscopic equivalent strain, $\overline{E}_{eq}$ ($f_0 = 20\%$): (—) low triaxiality, $\Sigma = 0.33$; (– ·) elevated triaxiality, $\Sigma = 1.0$.
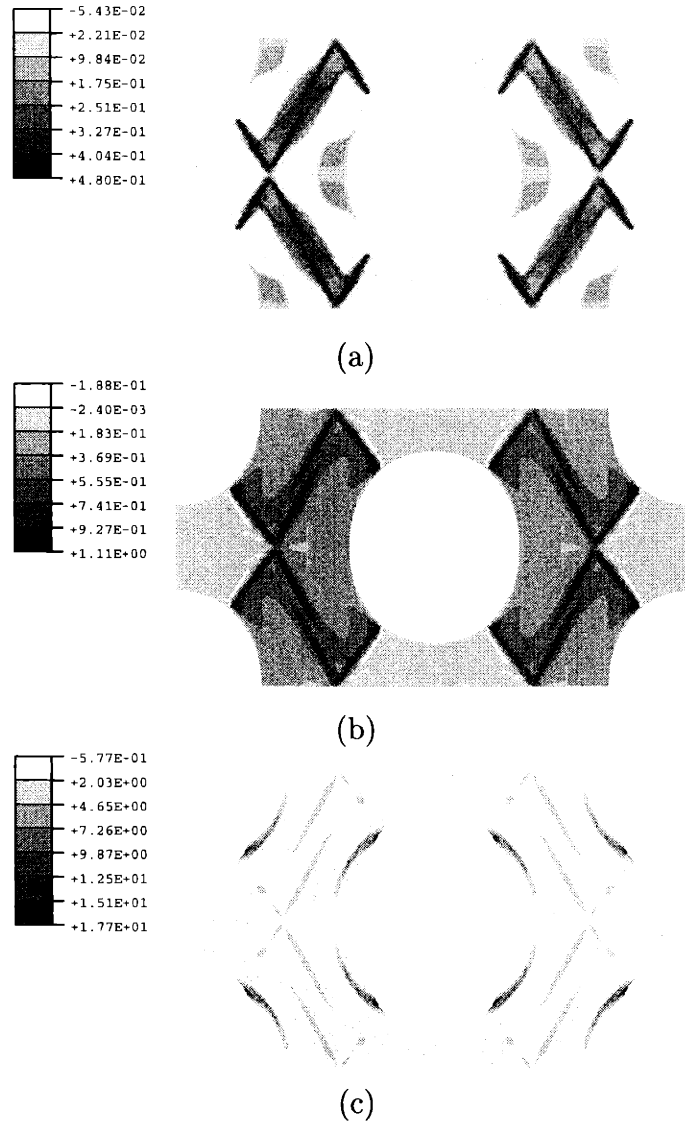
Figure 4-26: SA-AM model ($\Sigma = 1.0$). Normalized Equivalent Plastic Strain Rate, $\dot{\epsilon}^p_{eq}/\dot{\overline{E}}_{eq}$, at: (a) $\overline{E}_{zz}$=0.02; (b) $\overline{E}_{zz}$=0.03; (c) $\overline{E}_{zz}$=0.15.

Chapter 5

Discussion

Prior experimental work has shown that the incorporation of an elastomeric secondary phase in PA-6 acts to fundamentally change its morphology in regions immediately surrounding the second phase particles. As a result, skin layers of pronounced crystallographic orientation and mechanical anisotropy are created around each particle. When a critical, material-specific length exceeds the interparticle matrix spacing in such blends, the skin layers of neighboring particles overlap, and material resulting from preferred crystallization percolates through the primary phase.

In this thesis, micromechanical models of PA-6/rubber blends were developed that allowed the study of the influence of particle distribution, matrix morphology, volume fraction of modifier and triaxial loading conditions on the mechanical behavior of the blends. Two different particle arrangements in a PA-6 matrix were modeled, using the RVE model approach. The two models predicted substantially different deformation patterns both locally in the matrix material and macroscopically in the stress-strain response of the blends. Consequently, it was concluded that the assumed particle distribution is essential in developing realistic two-dimensional models of heterogeneous material systems.

Moreover, three different interparticle matrix ligament thicknesses (i.e., $\Lambda \gg \Lambda_c$, $\Lambda > \Lambda_c$ and $\Lambda \leq \Lambda_c$) were modeled for the same volume fraction of modifier ($f_0 = 20\%$). This was achieved by varying the amount of oriented matrix material of the RVE (from 0, to 5, to 100 vol. %). Comparisons between the deformation behavior

of each of these blends, in simple tension and triaxial loading conditions, revealed that the plastic deformation of the morphologically altered systems ($\Lambda > \Lambda_c$ and $\Lambda \leq \Lambda_c$) initiates and proceeds very differently from the deformation of the isotropic matrix blends ($\Lambda \gg \Lambda_c$). In particular, when $\Lambda > \Lambda_c$ the preferential orientation of the macromolecular chains parallel to the particle-matrix interface gives rise to an initially stiffer and higher strength overall mechanical response than that of the isotropic matrix polymer (i.e. the elastomeric particles surrounded by a thin layer of highly anisotropic material act as rigid inclusions). More importantly, when $\Lambda \leq \Lambda_c$ the plastic deformation of the matrix changes locally in both kind and degree from that of the isotropic matrix blends. At the unit cell level, the matrix is found to plastically deform via distinct shear bands, rather than a single broad band. These changes in underlying micromechanisms of deformation have little effect on the macroscopic mechanical response of the material in uniaxial tension, but have a significant effect under conditions of global triaxiality. In the latter case, the anisotropic matrix morphology is found to impede softening of the deviatoric strength and dilatational expansion of the material, while promoting extensive shear yielding via shear banding along specific crystallographic planes. Consequently, an energy dissipation and therefore toughening mechanism is identified to be in force when Λ of a blend is reduced below Λ_c.

Finally, the effect of varying the amount of rubber was studied (f_0 =15, 20, 25%), for the cases of $\Lambda \gg \Lambda_c$, and $\Lambda \leq \Lambda_c$. The same underlying deformation mechanisms were observed in each case independently of amount of modifier. Thus, it was concluded that once the criterion of $\Lambda \leq \Lambda_c$ is met, increasing the amount of modifier further increases the toughness of the blends in a predictable manner, result that agrees with experimental observations.

Chapter 6

Future work

Several approximations were made in developing the micromechanical models presented in this thesis. These approximations were judged necessary for the time frame of this work, but can be avoided or improved in the future. First, approximations were made to reduce the size of the deformation problems solved. Thus, the random distribution, size and shape of the modifying particles in PA-6/rubber blends, was modeled using two highly symmetric arrays of equally sized spherical particles. While some effort was made in developing realistic models of the actual three-dimensional system, the results presented here are nevertheless derived from the deformation of a single-particle RVE, and therefore lack the ability to capture the randomness in succession of deformation events in the real material.

Approximations were also made in the constitutive modeling of the PA matrix due to the complexity of the underlying microstructure, and lack of experimental data for the material of interest. Semicrystalline polymers with a simpler crystal structure, such as HDPE, have been studied extensively and would make a better model material. Finally, the currently available constitutive models for semicrystalline polymers either are too complex or not complete. In either case, they are not ideal for implementation in finite element micromechanical models of the type presented here and require further improvements. Such improvements are needed in order to study the extensive deformation that these material systems are able to undergo and thus to more fully understand the toughness of these materials.

Bibliography

Ahzi, S., Lee, B. J., and Asaro, J., 1994. Plasticity and anisotropy evolution in crystalline polymers. Mater. Sci. Eng. A189, 35–44.

Arruda, E. M. and Boyce, M. C., 1993. A three-dimensional constitutive model for the large stretch behavior of rubber elastic materials. J. Mech. Phys. Solids 41, 389–412.

Bao, G., Hutchinson, J. W., and McMeeking, R. M., 1991. Particle reinforcement of ductile matrices against plastic flow and creep. Acta Metall. Mater. 39, 1871–1882.

Bartczak, Z., Argon, A. S., Cohen, R. E., and Weinberg, M., 1999a. Toughness mechanism in semicrystalline polymer blends: II. High-density polyethylene toughened with calcium carbonate filler particles. Polymer 40, 2347–2365.

Bartczak, Z., Argon, A. S., Cohen, R. E., and Weinberg, M., 1999b. Toughness mechanism in semicrystalline polymer blends: I. High-density polyethylene toughened with rubbers. Polymer 40, 2331–2346.

Baumann, U. D., 1998. The role of particle cavitation in the toughening of polymers. Master's thesis, Massachusetts Institute of Technology, Cambridge, MA.

Borggreve, R. J. M., Gaymans, R. J., Schuijer, J., and Housz, J. F. I., 1987. Brittle-tough transition in nylon-rubber blends: effect of rubber concentration and particle size. Polymer 28, 1489–1496.

Bowden, P. B. and Young, R. J., 1974. Deformation mechanisms in crystalline polymers. J. Mater. Sci. 9, 2034–2051.

Boyce, M. C., Parks, D. M., and Argon, A. S., 1988. Large inelastic deformation of glassy polymers. Mech. Mater. 7, 15–33.

Boyce, M. C., Weber, G. G., and Parks, D. M., 1989. On the kinematics of finite strain plasticity. J. Mech. Phys. Solids 37, 647–665.

Chacko, V. P., Karasz, F. E., Farris, R. J., and Thomas, E. L., 1982. Morphology of $CaCO_3$-filled polyethylenes. J. Polym. Sci.: Polym. Phys. Ed. 20, 2177–2195.

Dijkstra, K., 1993. Nylon 6-rubber blends: V. The influence of rubber content on the yield stress. J. Mater. Sci. Letters 12, 1678–1679.

Dijkstra, K. and Bolscher, G. H. T., 1994. Nylon-6 / rubber blends: III. Stresses in and around rubber particles and cavities in a nylon matrix. J. Mater. Sci. 29, 4286–4293.

Fitchmun, D. and Newman, S., 1969. Surface morphology in semicrystalline polymers. Polym. letters 7, 301–305.

Flexman, E. A., 1979. Impact behavior of nylon 6,6 compositions: Ductile-brittle transitions. Polym. Eng. Sci. 19, 564–571.

Fukui, T., Kikuchi, Y., and Inoue, T., 1991. Elastic-plastic analysis of the toughening mechanism in rubber-modified nylon: matrix yielding and cavitation. Polymer 32, 2367–2371.

Gähde, J., Müller, V., Lebedev, Y. V., and Lipatov, Y. S., 1977. Effect of silane treatment of fillers in polyethylene-kaolin compositions. Polym. Sci. USSR 10, 1446–1452.

Galeski, A., Argon, A. S., and Cohen, R. E., 1987. Morphology of nylon 6 spherulites in bulk. Makromol. Chem. 188, 1195–1204.

Goodier, J. N., 1933. Concentration of stress around spherical and cylindrical inclusions and flaws. ASME Trans., J. Appl. Mech. 55, 39–44.

G'Sell, C. and Jonas, J. J., 1981. Yield and transient effects during the plastic deformation of solid polymers. J. Mater. Sci. 16, 1956–1974.

Gurson, A. L., 1977. Continuum theory of ductile rupture by void nucleation and growth: Part I. Yield criteria and flow rules for porous ductile media. ASME Trans., J. Eng. Mater. Techn. 99 Ser. H 1, 2-15.

Hill, R., 1947. A theory of the yielding and plastic flow of anisotropic metals. Proc. Roy. Soc. A, 281-297.

Huang, Y. and Kinloch, A. J., 1992. Modeling of the toughening mechanisms in rubber modified epoxy polymers: I. Finite element analysis studies. J. Mater. Sci. 27, 2753-2762.

Keller, A., 1959. Electron microscope-electron diffraction investigations of the crystalline texture of polyamides. J. Polym. Sci. XXXVI, 361-387.

Lee, B. J., Ahzi, S., and Asaro, R. J., 1995. On the plasticity of low symmetry crystals lacking five independent slip systems. Mech. Mater. 20, 1-8.

Lee, B. J., Argon, A. S., Parks, D. M., Ahzi, S., and Bartczak, Z., 1993. Simulation of large strain plastic deformation and texture evolution in high density polyethylene. Polymer 34, 3555-3575.

Lin, L. and Argon, A. S., 1992. Deformation resistance in oriented nylon 6. Macromolecules 25, 4011-4024.

Lin, L. and Argon, A. S., 1994. Review: Structure and plastic deformation of polyethylene. J. Mater. Sci. 29, 294-323.

Margolina, A. and Wu, S., 1988. Percolation model for brittle-tough transition in nylon/rubber blends. Polymer 29, 2170-2173.

Muratoglu, O. K., Argon, A. S., and Cohen, R. E., 1995a. Crystalline morphology of polyamide-6 near planar surfaces. Polymer 36, 2143-2152.

Muratoglu, O. K., Argon, A. S., and Cohen, R. E., 1995b. Toughening mechanism of rubber-modified polyamides. Polymer 36, 921-930.

Parks, D. M. and Ahzi, S., 1990. Polycrystalline plastic deformation and texture evolution for crystals lacking five independent slip systems. J. Mech. Phys. Solids 38, 701-724.

Schonhorn, H., 1967. Heterogeneous nucleation of polymer melts on high-energy surfaces. II. Effect of substrate morphology and wettability. Macromol. 1, 145–151.

Smit, R. J. M., Brekelmans, W. A. M., and Meijer, H. E. H., 1999. Prediction of the mechanical behavior of non-linear heterogeneous systems by multi-level finite element modeling. Submitted to Comp. Meth. Appl. Mech. Eng..

Socrate, S. and Boyce, M. C., 1999. Micromechanics of toughened polycarbonate. Accepted for publication in J. Mech. Phys. Solids.

Steenbrink, A. C., van der Giessen, E., and Wu, P. D., 1997. Void growth in glassy polymers. J. Mech. Phys. Solids 45, 405–437.

Tvergaard, V., 1982. On localization in ductile materials containing spherical voids. Int. J. Fract. 18, 237–251.

Tvergaard, V., 1996. Effect of void size difference on growth and cavitation instabilities. J. Mech. Phys. Solids 44, 1237–1253.

Tvergaard, V., 1998. Interaction of very small voids with larger voids. Int. J. Solids Structures 35, 3989–4000.

Wu, S., 1985. Phase structure and adhesion in polymer blends: A criterion for rubber toughening. Polymer 26, 1855–1863.

Wu, X., Zhu, X., and Qi, Z., 1991. Toughening mechanisms of rubber modified polypropylene: Fractograph analysis. The 8th international conference on deformation, yield and fracture of polymers, 1–4.

Appendix A

Determination of local material directions

A.1   Regular Array (RA) model

Figure A-1 (a) depicts the steady-state heat transfer boundary value problem solved to obtain the texture of Fig. 2-12 (a). Namely, the discretized structure analyzed in the RA approach was subjected to the following boundary conditions. All boundaries along which the base vector $\mathbf{m}_1(\mathbf{y})$ must be perpendicular, i.e., the particle-matrix interface (boundary AE) and boundaries BC and CD were subjected to constant temperatures, T_H and T_L respectively. In order for $\mathbf{m}_1(\mathbf{y})$ to point outward from the center of the particle, T_H was taken to be the highest temperature, while the absolute values of T_H and T_L is not important. Moreover, boundaries with which $\mathbf{m}_1(\mathbf{y})$ must be parallel, i.e., boundaries AB and ED, were taken to be adiabatic. The r and z components of the heat flux vector at each integrations point were saved in a file, which was then read by user subroutine ORIENT at the beginning of the stress analysis (see Appendix C.2).
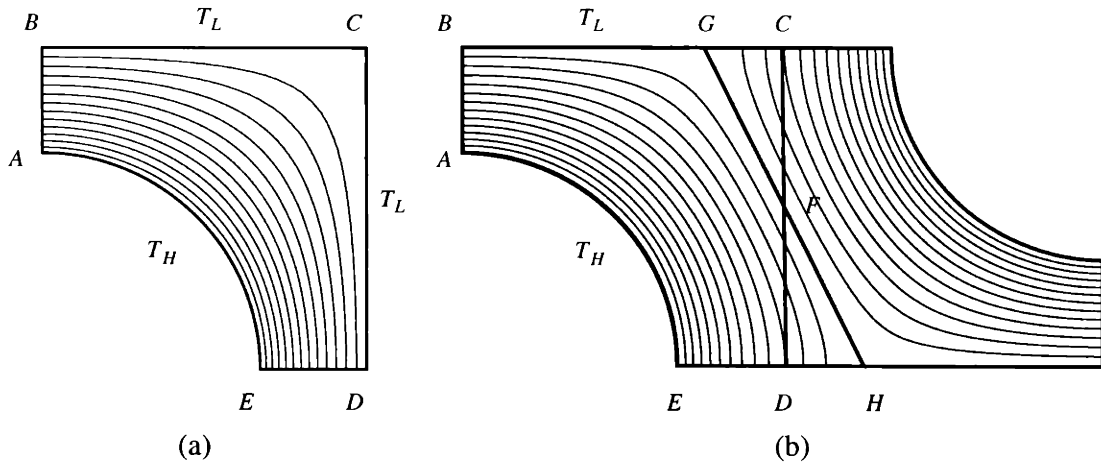
Figure A-1: Steady-state heat transfer analyses: (a) RA model, $f_0 = 20\%$; (b) SA model, $f_0 = 20\%$. Thick lines represent RVE boundaries, while thin lines represent the isotherms produced by the analysis.

A.2 Staggered Array (SA) model

Figure A-1 (b) depicts the boundary value problem solved to obtain the texture of Figure 2-12 (b). The structure analyzed was obtained by dividing the region $ABCDE$, with line GH. This line is perpendicular to the line connecting the centers of the particles and passes through its mid-point, point F. The imposed boundary conditions were identical to the ones discussed above, while in order to complete the two-dimensional domain analyzed in the SA approach, the texture of area DFH was used in place of CFG.

Appendix B

User Element

The user element employed to deform the RVE models involves only two nodes, both of which are initially located at point B, in the RA approach, and point F, in the SA approach (see Fig. B-1). The node referred to here as node 1, is fixed to move with the above mentioned points, while node 2 is a pseudo-node and moves independently. Nodes 1 and 2 are connected with a spring of stiffness, K, to monitor the applied axial force, t_z [1]. This is accomplished simply by displacing node 2 an amount, Δz, and calculating the force from $t_z = K\Delta z$. The macroscopically applied axial stress, $\overline{T}_{zz}$ can be then calculated from t_z and the position of node 1 in the z-direction, x_z, using eqns (2.8) and (2.9). From eqn (2.14), the value of desired Σ, and $\overline{T}_{zz}$ the appropriate level of radial stress, $\overline{T}_{rr}$, is calculated. Following, the radial force to be applied on the lateral boundary of the RVE, t_r, is found from $\overline{T}_{rr}$ and the position of node 1 in the r-direction, x_r, using again eqn (2.8). Finally, the magnitude of the determined radial force is applied on node 1, inside the user element. In this way, constant triaxial loading is achieved throughout the deformation. The position of nodes along the outer boundary of the RVE is also monitored inside the user element to allow for the calculation of the deformed volume of the models using eqn 2.9. The numerical implementation of this user element is included in Appendix C.3, together

---

[1]Note that, given the constraints (2.1) in the case of the RA model, and (2.2)-(2.5) in the case of the SA model, all reaction forces from nodes located along the outer boundary of the RVE models are lumped on node 1.
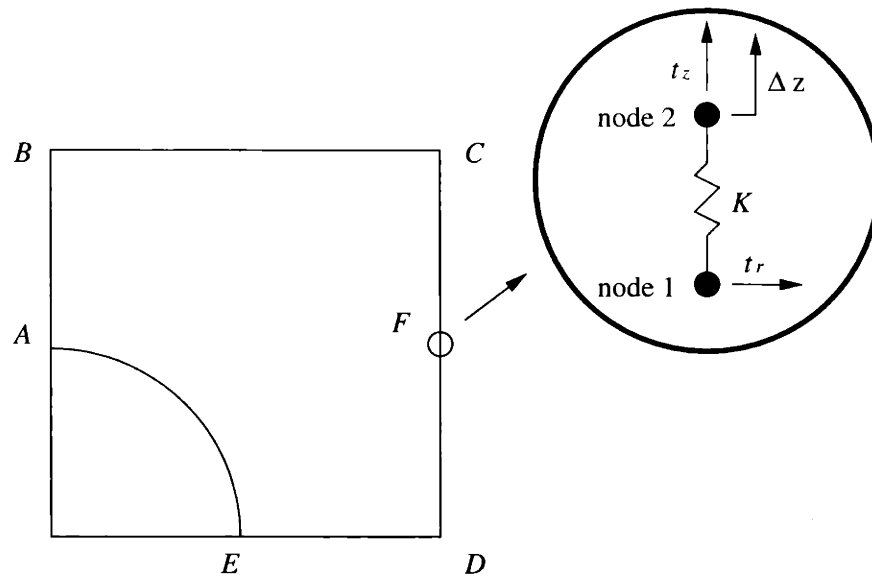
Figure B-1: User element used to deform the SA model.

with the subroutine used to displace node 2.

Appendix C

User subroutines

C.1   User multi-point constraints

```
SUBROUTINE MPC(UE,A,JDOF,MDOF,N,JTYPE,X,U,UINIT,MAXDOF,
&               LMPC,KSTEP,KINC,TIME,NT,NF,TEMP,FIELD)
INCLUDE 'ABA_PARAM.INC'
DIMENSION A(N),JDOF(N),X(6,N),U(MAXDOF,N),UINIT(MAXDOF,N),
&               TIME(2),TEMP(NT,N),FIELD(NF,NT,N)
 IF(JTYPE.EQ.1)THEN
JDOF(1) = 1
JDOF(2) = 1
JDOF(3) = 1
A(1) = 2*(1 + U(1,1))
A(2) = 2*(1 + U(1,2))
A(3) = (-4)*(1 + U(1,3))
C  = SQRT(2*(1 + U(1,3))**2 - (1 + U(1,2))**2)
UE = C - 1
 END IF
RETURN
END
```

C.2   Local axes orientation

```
SUBROUTINE ORIENT(T,NOEL,NPT,LAYER,KSPT,COORDS,BASIS,ORNAME,
```

```
      &                             NNODES,CNODES)
      INCLUDE 'ABA_PARAM.INC'
      CHARACTER*8 ORNAME
      PARAMETER(ELNUM = 4000,INTPT = 9)
      INTEGER ELEMENT
      DIMENSION T(3,3),
     & ELDATA1(ELNUM,INTPT),ELDATA2(ELNUM,INTPT)
      SAVE IFLAG,ELDATA1,ELDATA2
      DATA IFLAG/0/
IF(IFLAG.EQ.0)THEN
      OPEN(UNIT = 10,
     & FILE   = '/usr/home/kuhn2/tzika/orient_data/20_perc_c_cyl.dat',
     & STATUS = 'OLD')
      REWIND(10)
c Read and save the x and y coords of the heat flux vector, at each
c integration point, of each element into two ELNUM x INTPT arrays
c (ELDATA1 stores the x-coordinate and ELDATA2 stores the y-coordinate):
100       READ(10,*,END = 101) ELEMENT, INTEGPT, HEATFL1, HEATFL2
c Normalize:
   VALUE = SQRT((HEATFL1)**2 + (HEATFL2)**2)
   U     = (HEATFL1)/(VALUE)
   V     = (HEATFL2)/(VALUE)
            ELDATA1(ELEMENT,INTEGPT) = U
            ELDATA2(ELEMENT,INTEGPT) = V
            GOTO 100
101       IFLAG=1
END IF
c Define the local axes of anisotropy:
c Local 1-direction:
            T(1,1) = ELDATA1(NOEL,NPT) !NOEL = ELEMENT #, NPT = INTEG. POINT #
            T(2,1) = ELDATA2(NOEL,NPT)
c Local 2-direction:
            T(1,2) = -ELDATA2(NOEL,NPT)
            T(2,2) =  ELDATA1(NOEL,NPT)
      RETURN
      END
```

C.3 User element

```
      SUBROUTINE UEL(RHS,AMATRX,SVARS,ENERGY,NDOFEL,NRHS,NSVARS,
     & PROPS,NPROPS,COORDS,MCRD,NNODE,U,DU,V,A,JTYPE,TIME,DTIME,
     & KSTEP,KINC,JELEM,PARAMS,NDLOAD,JDLTYP,ADLMAG,PREDEF,NPREDF,
     & LFLAGS,MLVARX,DDLMAG,MDLOAD,PNEWDT,JPROPS,NJPROP,PERIOD)
      INCLUDE 'ABA_PARAM.INC'
      COMMON DELU1
      DIMENSION RHS(MLVARX,*),AMATRX(NDOFEL,NDOFEL),PROPS(*),
     & SVARS(*),ENERGY(8),COORDS(MCRD,NNODE),U(NDOFEL),
     & DU(MLVARX,*),V(NDOFEL),A(NDOFEL),TIME(2),PARAMS(*),
     & JDLTYP(MDLOAD,*),ADLMAG(MDLOAD,*),DDLMAG(MDLOAD,*),
     & PREDEF(2,NPREDF,NNODE),LFLAGS(5),JPROPS(*)
      PARAMETER(NMAX = 100)
      DIMENSION
     & UCOORDS(2,NMAX), UM(2,NMAX), UN(2,NMAX), UDS(NMAX)
      ONE   = 1.D0
      TWO   = 2.D0
      THREE = 3.D0
      PI    = TWO * TWO * DATAN(ONE)
      AK    = PROPS(1) ! Spring Striffness
      TRIAX = PROPS(2) ! Triaxiality Ratio
c Initialize variables:
      DO K1   = 1,NDOFEL
       DO KRHS = 1,NRHS
       RHS(K1,KRHS) = 0.D0
       END DO
       DO K2   = 1,NDOFEL
       AMATRX(K2,K1) = 0.D0
       END DO
      END DO
c Calculate axial force acting on the spring:
      DELU1    = U(90) - U(46) ! Spring Elongation
      FORCE1   = AK * DELU1 ! Force
      RHS(46,1) =  FORCE1
      RHS(90,1) = -FORCE1
```

```fortran
c Calculate contribution to the Jacobian (stiffness):
      AMATRX(46,46)   =  AK
      AMATRX(90,90)   =  AK
      AMATRX(46,90)   = -AK
      AMATRX(90,46)   = -AK
c Calculate the ratio of the radial to the axial stress:
      FACTOR    = ((THREE*TRIAX)-ONE)/(TWO+(THREE*TRIAX))
c Calculate current coordinates of nodes along the outer
c boundary of the RVE:
      DO 70 KNN = 1,NNODE
 UCOORDS(1,KNN) = COORDS(1,KNN) + U((2*KNN)-1)
 UCOORDS(2,KNN) = COORDS(2,KNN) + U(2*KNN)
   70 CONTINUE
c Initialize volume:
      VU = 0.0D0
c Calculate position vectors and surface normals:
      DO 100 KNN = 1,(NNODE-2)
 UM(1,KNN) = ( UCOORDS(1,KNN) + UCOORDS(1,(KNN+1)) ) / 2.D0
 UM(2,KNN) = ( UCOORDS(2,KNN) + UCOORDS(2,(KNN+1)) ) / 2.D0
 UN(1,KNN) = ( UCOORDS(2,KNN) - UCOORDS(2,(KNN+1)) )
 UN(2,KNN) = ( UCOORDS(1,(KNN+1)) - UCOORDS(1,KNN) )
 ULENG = DSQRT((UN(1,KNN))**2 + (UN(2,KNN))**2)
c Normalize:
 UN(1,KNN) = UN(1,KNN) / ULENG
 UN(2,KNN) = UN(2,KNN) / ULENG
  100 CONTINUE
c Calculate surface increment:
      DO 120 KNN = 1,(NNODE-2)
      UDS(KNN) = PI * (UCOORDS(1,KNN) + UCOORDS(1,(KNN+1))) *
     &          DSQRT( ((UCOORDS(1,KNN) - UCOORDS(1,(KNN+1)))**2
     &          + ((UCOORDS(2,KNN) - UCOORDS(2,(KNN+1)))**2) )
  120 CONTINUE
c Calculate current volume:
      DO 130 KNN = 1,(NNODE-2)
         VU = VU + (( (UM(1,KNN)*UN(1,KNN)) + (UM(2,KNN)*UN(2,KNN)))
     &             * UDS(KNN) )
```

```fortran
  130 CONTINUE
      VU = VU/3.DO
c Macroscopic Axial Stress:
      SIGZ      = (1/VU)*(FORCE1*UCOORDS(2,23))
c Macroscopic Radial Stress:
      SIGR      = FACTOR * SIGZ
c Radial force applied on the lateral boundary:
      FORCE2    = (2.DO*VU*SIGR)/(UCOORDS(1,23))
      RHS(45,1) = FORCE2
      SVARS(1)  = VU
      SVARS(2)  = SIGZ
      SVARS(3)  = DELU1
      SVARS(4)  = SIGEQ
      RETURN
      END
c

      SUBROUTINE DISP (U, KSTEP, KINC, TIME, NODE, JDOF)
      INCLUDE 'ABA_PARAM.INC'
      COMMON DELU1
      DIMENSION U(3), TIME(2)
       U(1) = 0.08 * TIME(2) + DELU1
      RETURN
      END
```

Appendix D

CH driver

```
C Written by Said Ahzi, Jean-Marc Diani and Panagiota A. Tzika.


C INPUT DATA FILES:
C loading.dat     --- DEFORMATION HISTORY (file 15)
C material.dat    --- MATERIAL PARAMETERS (file 10)
C epsvar.dat      --- SHEAR SYSTEMS (file 11)
C aeuler.dat      --- EULER ANGLES  (file 12)
C OUTPUT FILES:
C AA_DRIVER_OUTPUT (time, strain, stress) (file 50)
C AA_EULER_OUTPUT  (euler angles) (file 103)


C MAIN VARIABLES USED IN THIS PROGRAM:


C AMV(3,MAXSYST)          -- SLIP DIRECTION VECTORS (input in crystal coords)
C ANV(3,MAXSYST)          -- SLIP PLANE NORMAL VECTORS (input in crystal coords)
C DBSAG(3,MAXSYST,MAXCRYS)-- SLIP DIRECTION VECTORS (in global coords)
C DNSAG(3,MAXSYST,MAXCRYS)-- SLIP PLANE NORMAL VECTORS (in global coords)
C QG(3,3,MAXCRYS)         -- ROTATION MATRIX
C SMATC(5,MAXSYST)        -- SCHMID TENSOR (in crystal coords)
C SCHG(5,MAXSYST,MAXCRYS) -- SCHMID TENSOR (in global coords at time t)
C DBAR(5)                 -- MACROSCOPIC STRAIN RATE (imposed)
C SBAR(5)                 -- MACROSCOPIC STRESS (deviatoric)
C WBAR(3,3)               -- MACROSCOPIC SPIN RATE (imposed)
```

```
C TGAMI(MAXSYST,MAXSYST)   -- TENSOR GAMMA^alpha beta^-1

C SALPHT(MAXSYST,MAXCRYS) -- SLIP RESISTANCE (constant)

C P(5,5,MAXCRYS)           -- LOCAL CONSTRUCTED PROJECTION FOR EACH CRYSTAL

C PAV(5,5)                 -- <[P]> AVERAGE CONSTRUCTED PROJECTION

C PAVINV(5,5)              -- <[P]>^-1 : INVERSE OF PREVIOUS

C D(5,MAXCRYS)             -- STRAIN RATE IN EACH CRYSTAL

C DGAMMA(MAXSYST,MAXCRYS) -- SHEAR RATE OF EACH SYSTEM IN EACH CRYSTAL

C SSTAR(5,MAXCRYS)         -- S^* IN EACH CRYSTAL


      PROGRAM MAIN


      IMPLICIT REAL*8 (A-H,O-Z)

      PARAMETER(MAXCRYS = 3000, MAXSYST = 5)

      COMMON/VARIABLES/AMV(3,MAXSYST),ANV(3,MAXSYST),QG(3,3,MAXCRYS),

     &   SMATC(5,MAXSYST),DBAR(5),SBAR(5),NSYST,NCRYS,

     &   TGAMI(MAXSYST,MAXSYST),SALPHT(MAXSYST,MAXCRYS),

     &   PAVINV(5,5),WBAR(3,3),SSTAR(5,MAXCRYS),

     &   D(5,MAXCRYS),DGAMMA(MAXSYST,MAXCRYS)


      COMMON/MATPLAS/GDOTO,AM,HO,R1,R2,R3,STILDE,AHARD,

     &   QL,CRYSDIA,G,WIDTH


      INTEGER  FD,LD,CD,TR1,TR2

      REAL*8  LBARDOT(3,3),A(3,3),DB3(3,3)

      REAL*8  DNSAG(3,MAXSYST,MAXCRYS),DBSAG(3,MAXSYST,MAXCRYS)

      REAL*8  GDOT(MAXSYST),LDOT(3,3),DBSA(3,MAXSYST)

      REAL*8  DNSA(3,MAXSYST),SSTAV(5),PAV(5,5)

      REAL*8  SDEV(3,3),T(3,3),SCHG(5,MAXSYST,MAXCRYS)


C READ INPUT MATERIAL PARAMETERS (from file material.dat)


      OPEN(UNIT=10,FILE='nylon6.dat',STATUS='OLD')

      REWIND(10)

      READ(10,*)

      READ(10,*) GDOTO,AM !flow parameters

      READ(10,*)
```

```fortran
      READ(10,*) R1,R2,R3


C INITIALIZE STATE


C -OBTAIN INFORMATION ABOUT AVAILABLE SLIP SYSTEMS IN CRYSTAL COORDS (AMV, ANV)
C  FROM FILE epsvar.dat
C -CALCULATE THE SYMMETRIC, TRACELESS SCHMID TENSOR ASSOCIATED WITH EACH SLIP
C  SYSTEM IN CRYSTAL COORDS (SMATC)
C -CALCULATE THE COMPONENTS OF THE CONSTANT, SYMMETRIC  MATRIX GAMMA^alpha beta
C  (TGAM), AS WELL AS IT'S INVERSE (GAMMA^alpha beta)^-1 (TGAMI)
C -OBTAIN EULER ANGLES FOR EACH CRYSTAL FROM FILE aeuler.dat AND CALCULATE
C  ROTATION MATRICES FOR EACH CRYSTAL
C -FOR NYLON6 READ THREE CONSTANT CRSS
C -CALCULATE THE SCHMID TENSOR IN GLOBAL COORDS (SCHG) USING SUBROUTINE SCHMAC


      CALL INITIAL(DNSAG,DBSAG,SCHG)


C SET DEFORMATION HISTORY (from file loading.dat)
C LFLAG: 1 --- SIMPLE SHEAR
C 2 --- SIMPLE TENSION/COMPRESSION
C 3 --- PLANE STRAIN TENSION/COMPRESSION


      OPEN(UNIT=15,FILE='loading.dat',STATUS='OLD')
      REWIND(15)
      READ(15,*)
      READ(15,*) LFLAG
      READ(15,*)
      READ(15,*) EQINCR
      READ(15,*)
      READ(15,*) STRAINRATE


C MACROSCOPIC VELOCITY GRADIENT IMPOSED ON THE CRYSTAL AGGREGATE (LBARDOT)


      IF(LFLAG.EQ.1)THEN
      CALL ZEROM(LBARDOT,3)
      LBARDOT(1,2) = STRAINRATE
```

```fortran
      WRITE(*,*)'IMPOSED MACROSCOPIC VELOCITY GRADIENT'
          DO 5000 I=1,3
           WRITE(*,2) (LBARDOT(I,J),J=1,3)
5000      CONTINUE
      ELSE IF(LFLAG.EQ.2)THEN
      WRITE(*,*)'PLEASE SPECIFY LD,TR1,TR2'
      READ(*,*)LD,TR1,TR2
      DTIME=2.D0
      DEQPSTN=EQINCR/DTIME
      TOL=0.00001D0
      ELSE IF(LFLAG.EQ.3)THEN
      WRITE(*,*)'PLEASE SPECIFY LD,CD,FD'
      READ(*,*)LD,CD,FD
      CALL ZEROM(LBARDOT,3)
      LBARDOT(CD,CD) = 0.D0
      LBARDOT(FD,FD) = -STRAINRATE
      LBARDOT(LD,LD) = STRAINRATE
      WRITE(*,*)'IMPOSED MACROSCOPIC VELOCITY GRADIENT'
          DO 5001 I=1,3
           WRITE(*,2) (LBARDOT(I,J),J=1,3)
5001      CONTINUE
      END IF

C DECOMPOSE LBARDOT TO GET:
C -MACROSCOPIC DEFORMATION RATE (DBAR,A 5-VECTOR)
C -MACROSCOPIC SPIN (WBAR, A 3X3-MATRIX)
C -ALSO CALCULATE DEQPSTN AND GET TIME INCREMENT (DTIME)

      IF(LFLAG.EQ.1.OR.LFLAG.EQ.3)THEN
      DO 10 I=1,3
      DO 10 J=1,3
          DB3(I,J)=(LBARDOT(I,J)+LBARDOT(J,I))/2.D0
          WBAR(I,J)=(LBARDOT(I,J)-LBARDOT(J,I))/2.D0
10 CONTINUE
      WRITE(*,*)'MACROSCOPIC DEFORMATION RATE'
          DO 5002 I=1,3
```

108

```fortran
          WRITE(*,2) (DB3(I,J),J=1,3)
5002         CONTINUE
       CALL TRACEM(DB3,TRD)
       WRITE(*,*)'TRACE OF D IS:',TRD
       WRITE(*,*)'MACROSCOPIC SPIN'
       DO 5003 I=1,3
        WRITE(*,2) (WBAR(I,J),J=1,3)
5003         CONTINUE
       CALL TRACEM(WBAR3,TRW)
       WRITE(*,*)'TRACE OF W IS:',TRW
DEQPSTN=0.D0
CALL DOTPM(DB3,DB3,DEQPSTN)
WRITE(*,*)'DBAR*DBAR IS'
WRITE(*,*)DEQPSTN
DEQPSTN=DSQRT(2.D0*DEQPSTN/3.D0)
DTIME=EQINCR/DEQPSTN !time increment
CALL MATVEC(DB3,DBAR)
END IF


C ADDITIONAL INPUT (from loading.dat)

READ(15,*)
READ(15,*) EPSMAX
READ(15,*)
READ(15,*) TEXSTNINC

C OPEN FILES FOR WRITING OUTPUT
OPEN(50,FILE='AA_DRIVER_OUTPUT',STATUS='OLD')
REWIND(50)
IF(LFLAG.EQ.1) THEN
  WRITE(50,'(A,//1X,A,4X,A,6X,A,6X,A,8X,A,8X,A,8X,A//)')
  +      'OUTPUT FROM DRIVER: SIMPLE SHEAR',
  +      'INC','M. EQ. STRAIN','M. EQ. STRESS','SDEV(1,2)',
  +      'SDEV(1,3)','SDEV(2,3)'
ELSE IF(LFLAG.EQ.2) THEN
  WRITE(50,'(A,//1X,A,2X,A,2X,A,2X,A,2X,A,2X,A//)')
```

```
        +       'OUTPUT FROM DRIVER: SIMPLE TENSION/COMPRESSION',
        +       'INC','M. EQ. STRAIN','M. EQ. STRESS','SDEV(1,2)',
        +       'SDEV(1,3)','SDEV(2,3)'
ELSE IF(LFLAG.EQ.3) THEN
  WRITE(50,'(A,//1X,A,2X,A,2X,A,2X,A,2X,A,2X,A,2X,A//)')
        +       'OUTPUT FROM DRIVER: PLANE STRAIN TENSION/COMPRESSION',
        +       'INC','M. EQ. STRAIN','M. EQ. STRESS','SDEV(1,2)',
        +       'SDEV(1,3)','SDEV(2,3)','SDEV(3,3)'
  END IF


        OPEN(103,FILE='AA_EULER_OUTPUT',STATUS='OLD')
        REWIND(103)


        WRITE(103,'(A,//A,I3)')
        +         'OUTPUT OF EULER ANGLES FOR CALCULATING TEXTURE:',
        +         'NCRYS = ',NCRYS


C COMPUTATION

PI=4.D0*DATAN(1.D0)
SQR2=DSQRT(2.D0)
SQR3=DSQRT(3.D0)
EPSILON=0.D0 !initialize strain
ISTEP=0
999  IF(LFLAG.EQ.2)THEN
CALL MNBRAK(DTIME,LD,TR1,TR2,STRAINRATE,SCHG,
      + AX,BX,CX)
WRITE(*,*)'AX, BX, CX ARE:',AX,BX,CX
CALL GOLDEN(DTIME,LD,TR1,TR2,STRAINRATE,SCHG,
      + AX,BX,CX,TOL,RMIN,GOLE)
        CALL ZEROM(LBARDOT,3)
LBARDOT(LD,LD)=STRAINRATE
LBARDOT(TR1,TR1)=-STRAINRATE/(1+RMIN)
LBARDOT(TR2,TR2)=-(RMIN*STRAINRATE)/(1+RMIN)
DO 55 I=1,3
DO 55 J=1,3
```

```
            DB3(I,J)=(LBARDOT(I,J)+LBARDOT(J,I))/2.DO

            WBAR(I,J)=(LBARDOT(I,J)-LBARDOT(J,I))/2.DO

55 CONTINUE

CALL MATVEC(DB3,DBAR)

END IF


C -TAKE THE MATRIX (GAMMA^-1)^alpha beta (TGAMI) CALCUALTED IN SUBROUTINE

C  INITIAL AND  USE IT TO CALCULATE THE LOCAL FOURTH ORDER PROJECTION TENSOR P (P)

C -CALCULATE  IT'S VOLUME AVERAGE OVER THE POLYCRYSTALLINE AGGREGATE <P> (PAV)

C -USE THAT TO CALCULATE THE LOCAL DEFORMATION RATE D (TEMPD)

C -USE THAT TO CALCULATE THE SHEAR RATE ON EACH SYSTEM dgamma^alpha (DAGAMM)

C -GET THE RESOLVED SHEAR STRESS ON EACH SYSTEM tau^alpha (RSS)

C -GET sigma^alpha (SIGALPH)

C -GET S^* (SSTAR)

C -CALCULATE IT'S VOLUME AVERAGE <S^*> (SSTAV)


CALL SOLVCRYS(DTIME,SCHG,SSTAV,PAV) !time increment, global Schmid, <S^*>


C UPDATE THE GLOBAL DEVIATORIC CAUCHY STRESS (SBAR), WHICH FROM MACROSCOPIC

C EQUILIBR. IS EQUAL TO <P>^-1 * [<S^*>] (OR SBAR=PAVINV*SSTAV)


CALL MULTMV(PAVINV,SSTAV,SBAR,5)


C BEGIN THE LOOP ON CRYSTALS FOR VARIABLE UPDATING


DO 70 ICRYS=1,NCRYS


C UPDATE THE ORIENTATION MATRIX [QG]


DO 80 IS=1,NSYST

GDOT(IS)=DGAMMA(IS,ICRYS)/DTIME

80     CONTINUE


   DO 100 IS=1,NSYST

    DO 105 I=1,3

   DBSA(I,IS)=DBSAG(I,IS,ICRYS)
```

```
      DNSA(I,IS)=DNSAG(I,IS,ICRYS)
105 CONTINUE
100    CONTINUE
DO 110 I=1,3
DO 110 J=1,3
LDOT(I,J)=0.D0
             DO 115 KS=1,NSYST
                 LDOT(I,J)=LDOT(I,J)+DBSA(I,KS)*DNSA(J,KS)*GDOT(KS)
115              CONTINUE
           IF(DABS(LDOT(I,J)/DEQPSTN).LT.1.D-06) LDOT(I,J)=0.D0
110    CONTINUE
DO 119 I=1,3
DO 119 J=1,3
         A(I,J)=QG(I,J,ICRYS)
119    CONTINUE
           CALL ORIENT(DTIME,LDOT,A)
           DO 120 I=1,3
           DO 120 J=1,3
       QG(I,J,ICRYS)=A(I,J)
120    CONTINUE


C END OF VARIABLE UPDATING => NEW CRYSTAL


70 CONTINUE    !loop for variable updating, done for all crystals


C UPDATE NORMALS, SLIP DIRECTIONS AND SCHMID TENSORS IN GLOBAL AXES


       CALL SCHMAC(DNSAG,DBSAG,SCHG) !SCHMAC has the crystal loop built in


C WRITE THE RESULTS IN OUTPUT FILES


SDOTS=0.D0
SEQ=0.D0
EQPSTN = ISTEP*DEQPSTN*DTIME
CALL VECMAT(SBAR,SDEV) !transforms a 5-vector back to a 3X3 matrix
CALL DOTPM(SDEV,SDEV,SDOTS) !scalar product of two matrices
```

```fortran
      SEQ=DSQRT(1.5D0*SDOTS)
      IF(LFLAG.EQ.2)THEN
      T(1,1)=SDEV(1,1)-0.5D0*(SDEV(TR1,TR1)+SDEV(TR2,TR2))
      T(2,2)=SDEV(2,2)-0.5D0*(SDEV(TR1,TR1)+SDEV(TR2,TR2))
      T(3,3)=SDEV(3,3)-0.5D0*(SDEV(TR1,TR1)+SDEV(TR2,TR2))
      T(1,2)=SDEV(1,2)
      T(2,1)=T(1,2)
      T(1,3)=SDEV(1,3)
      T(3,1)=T(1,3)
      T(2,3)=SDEV(2,3)
      T(3,2)=T(2,3)
      ELSE IF(LFLAG.EQ.3)THEN
      T(1,1)=SDEV(1,1)-SDEV(FD,FD)
      T(2,2)=SDEV(2,2)-SDEV(FD,FD)
      T(3,3)=SDEV(3,3)-SDEV(FD,FD)
      T(1,2)=SDEV(1,2)
      T(2,1)=T(1,2)
      T(1,3)=SDEV(1,3)
      T(3,1)=T(1,3)
      T(2,3)=SDEV(2,3)
      T(3,2)=T(2,3)
      END IF
      GOLE=DABS(SDEV(TR1,TR1)-SDEV(TR2,TR2))
      WRITE(50,'(I4,2X,9(E10.4,4X))')ISTEP,DABS(EQPSTN),DABS(SEQ),
     + DABS(T(TR1,TR1)/T(LD,LD)),DABS(T(TR2,TR2)/T(LD,LD)),
     + DABS(T(1,2)/T(LD,LD)),DABS(T(1,3)/T(LD,LD)),
     + DABS(T(2,3)/T(LD,LD)),RMIN,GOLE
      WRITE(*,*)' '
       WRITE(*,'(A,1X,A,2X,A)')'ISTEP','EQ.STRAIN','EQ.STRESS'
      WRITE(*,'(I4,1X,2(E10.4,1X))')ISTEP,EQPSTN,SEQ
      WRITE(*,*)' '
       WRITE(*,*)'MACROSCOPIC DEVIATORIC STRESS'
       DO 8000 I=1,3
       WRITE(*,2) (SDEV(I,J),J=1,3)
8000        CONTINUE
      CALL TRACEM(SDEM,TRS)
```

```fortran
      WRITE(*,*)'TRACE OF SDEV IS:',TRS


C CALCULATE AND STORE THE TEXTURE


      IF ((TEXSTNINC .GE. EPSILON)
     +      .AND. (TEXSTNINC .LT. (EPSILON+EQINCR))) THEN
             WRITE(103,*)' '
             WRITE(103,'(A,F6.4)')
     +           'STRAIN =',EPSILON
              WRITE(103,*)' '
             WRITE(103,'(2X,A,2X,A,2X,A)') '       THETA',
     +              '         PHI',',       OMEGA'
            WRITE(103,*)' '
        DO 140 ICRYS=1,NCRYS
      DO 150 I=1,3
                DO 150 J=1,3
              A(I,J)=QG(I,J,ICRYS)
150          CONTINUE
             CALL EULANG(A,3,TH,PHI,OM,ICRYS)
             TH  = TH*180.D0/PI
             PHI = PHI*180.D0/PI
             OM  = OM*180.D0/PI
             WRITE(103,'(3(4X,F10.4))') TH,PHI,OM
140          CONTINUE
        ENDIF


C UPDATE THE 999 LOOP


      EPSILON=EPSILON+DTIME*DEQPSTN
      ISTEP=ISTEP+1


C GO TO NEXT INCREMENT IF THE MAXIMUM STRAIN IS NOT EXCEEDED


      IF(EPSILON.LT.EPSMAX) GOTO 999
        STOP
      END
```

```
C                MAIN SUBROUTINES


C SOLVCRYS
         SUBROUTINE SOLVCRYS(DTIME,SCHG,SSTAV,PAV)
IMPLICIT REAL*8 (A-H,O-Z)
PARAMETER(MAXCRYS = 3000, MAXSYST = 5)
COMMON/VARIABLES/AMV(3,MAXSYST),ANV(3,MAXSYST),QG(3,3,MAXCRYS),
     +   SMATC(5,MAXSYST),DBAR(5),SBAR(5),NSYST,NCRYS,
     +   TGAMI(MAXSYST,MAXSYST),SALPHT(MAXSYST,MAXCRYS),
     +   PAVINV(5,5),WBAR(3,3),SSTAR(5,MAXCRYS),
     +   D(5,MAXCRYS),DGAMMA(MAXSYST,MAXCRYS)
COMMON/MATPLAS/GDOTO,AM,HO,R1,R2,R3,STILDE,AHARD,
     +   QL,CRYSDIA,G,WIDTH
REAL*8 RSS(MAXSYST),SIGALPH(MAXSYST),P(5,5,MAXCRYS),PAV(5,5)
REAL*8 SSTAV(5),TEMPD(5),SCHG(5,MAXSYST,MAXCRYS),DIFF(5,5)
REAL*8 RES(5)


C  CALCULATES THE PROJECTION TENSORS: P, <P>, <P>^-1


DO 10 ICRYS=1,NCRYS
   DO 30 I=1,5
   DO 30 J=1,5
P(I,J,ICRYS)=0.D0
DO 40 KS=1,NSYST
DO 40 LS=1,NSYST
   P(I,J,ICRYS)=P(I,J,ICRYS)+
     +            TGAMI(KS,LS)*SCHG(I,KS,ICRYS)*SCHG(J,LS,ICRYS)
40 CONTINUE
30    CONTINUE
10 CONTINUE
IF(ISOLVE.EQ.0)THEN
WRITE(*,*)'OUTPUT FROM SUBR. SOLVCRYS: P FOR ICRYS=1'
      DO 7000 I=1,5
      WRITE(*,2) (P(I,J,1),J=1,5)
7000      CONTINUE
```

```fortran
      ENDIF
      DO 50 I=1,5
      DO 50 J=1,5
         PAV(I,J)=0.D0
         DO 60 ICRYS=1,NCRYS
      PAV(I,J)=PAV(I,J)+P(I,J,ICRYS)
60 CONTINUE
      PAV(I,J)=PAV(I,J)/FLOAT(NCRYS)
50 CONTINUE
      IF(ISOLVE.EQ.0)THEN
      WRITE(*,*)'OUTPUT FROM SUBR. SOLVCRYS: PAV'
C WRITE(*,*)'ISOLVE IS:',ISOLVE
         DO 7001 I=1,5
          WRITE(*,2) (PAV(I,J),J=1,5)
7001     CONTINUE
      DO 7010 I=1,5
      DO 7010 J=1,5
         IF(I.EQ.J)THEN
         DIFF(I,J)=((PAV(I,J)-0.6D0)/0.6D0)*100.D0
         ELSE
         DIFF(I,J)=PAV(I,J)
         ENDIF
7010 CONTINUE
      WRITE(*,*)'OUTPUT FROM SUBR. SOLVCRYS: % DIFF'
         DO 7011 I=1,5
          WRITE(*,2) (DIFF(I,J),J=1,5)
7011     CONTINUE
      ENDIF
         CALL MATINV(PAV,5,5,PAVINV)
         IF(ISOLVE.EQ.0)THEN
      WRITE(*,*)'OUTPUT FROM SUBR. SOLVCRYS: PAVINV'
C WRITE(*,*)'ISOLVE IS:',ISOLVE
         DO 7002 I=1,5
          WRITE(*,2) (PAVINV(I,J),J=1,5)
7002     CONTINUE
      ENDIF
```

```
DO 55 L=1,5
RES(L)=0.D0
DO 100 K=1,5
RES(L)=RES(L)+PAVINV(L,K)*DBAR(K)*DTIME
100 CONTINUE
55 CONTINUE
DO 70 ICRYS=1,NCRYS


C   CALCULATES THE STRAIN RATE WITHIN EACH CRYSTAL.


    DO 80 I=1,5
TEMPD(I)=0.D0
DO 90 L=1,5
TEMPD(I)=TEMPD(I)+P(I,L,ICRYS)*RES(L)
90 CONTINUE
80 CONTINUE
IF((ISOLVE.EQ.0).AND.(ICRYS.EQ.1))THEN
WRITE(*,*)'OUTPUT FROM SUBR. SOLVCRYS: TEMPD FOR ICRYS=1'
C WRITE(*,*)'ISOLVE IS:',ISOLVE
      DO 7003 I=1,5
       WRITE(*,2) TEMPD(I)
7003        CONTINUE
ENDIF


C   GET THE SHEAR RATE ON EACH SYSTEM: DGAMMA


  DO 115 IS = 1,NSYST
   DGAMMA(IS,ICRYS)=0.D0
   DO 120 JS=1,NSYST
        RAS=0.D0
        DO 130 K=1,5
        RAS=RAS+TEMPD(K)*SCHG(K,JS,ICRYS)
130          CONTINUE
        DGAMMA(IS,ICRYS)=DGAMMA(IS,ICRYS)+TGAMI(IS,JS)*RAS
120     CONTINUE
115     CONTINUE
```

```fortran
      IF((ISOLVE.EQ.0).AND.(ICRYS.EQ.1))THEN
      WRITE(*,*)'OUTPUT FROM SUBR. SOLVCRYS: DGAMMA FOR ICRYS=1'
            DO 7004 IS=1,NSYST
             WRITE(*,2) DGAMMA(IS,1)
7004        CONTINUE
      ENDIF


C  GET THE RESOLVED SHEAR STRESS (RSS) AND (SIG^ALPHA)


      DO 140 IS = 1,NSYST
      RSS(IS)=(DGAMMA(IS,ICRYS)/DABS(DGAMMA(IS,ICRYS)))*
     + SALPHT(IS,ICRYS)*
     + (DABS(DGAMMA(IS,ICRYS))/(DTIME*GDOTO))**AM
140     CONTINUE
      IF((ISOLVE.EQ.0).AND.(ICRYS.EQ.1))THEN
      WRITE(*,*)'OUTPUT FROM SUBR. SOLVCRYS: RSS FOR ICRYS=1'
            DO 7005 IS=1,NSYST
             WRITE(*,2) RSS(IS)
7005        CONTINUE
      ENDIF
      DO 145 IS = 1,NSYST
      SIGALPH(IS)=0.DO
         DO 150 KS = 1,NSYST
         SIGALPH(IS)=SIGALPH(IS)+TGAMI(IS,KS)*RSS(KS)
150     CONTINUE
145     CONTINUE
      IF((ISOLVE.EQ.0).AND.(ICRYS.EQ.1))THEN
      WRITE(*,*)'OUTPUT FROM SUBR. SOLVCRYS: SIGALPH FOR ICRYS=1'
            DO 7006 IS=1,NSYST
             WRITE(*,2) SIGALPH(IS)
7006        CONTINUE
      ENDIF


C  GET THE S^*


      DO 160 I=1,5
```

```fortran
SSTAR(I,ICRYS)=0.D0
DO 170 KS=1,NSYST
SSTAR(I,ICRYS)=SSTAR(I,ICRYS)+SIGALPH(KS)*
     +          SCHG(I,KS,ICRYS)
170 CONTINUE
160    CONTINUE
IF((ISOLVE.EQ.0).AND.(ICRYS.EQ.1))THEN
WRITE(*,*)'OUTPUT FROM SUBR. SOLVCRYS: SSTAR FOR ICRYS=1'
     DO 7007 I=1,5
      WRITE(*,2) SSTAR(I,1)
7007     CONTINUE
ENDIF
70 CONTINUE !crystal loop

C  GET <S^*>

DO 180 I=1,5
   SSTAV(I) = 0.D0
   DO 190 ICRYS=1,NCRYS
      SSTAV(I) = SSTAV(I)+SSTAR(I,ICRYS)
190    CONTINUE
SSTAV(I)=SSTAV(I)/FLOAT(NCRYS)
180 CONTINUE
IF(ISOLVE.EQ.0)THEN
WRITE(*,*)'OUTPUT FROM SUBR. SOLVCRYS: SSTAV'
     DO 7008 I=1,5
      WRITE(*,2) SSTAV(I)
7008     CONTINUE
ENDIF
ISOLVE=ISOLVE+1
2 FORMAT(5(2X,F10.6))
RETURN
END

C INITIAL
```

```fortran
      SUBROUTINE INITIAL(DNSAG,DBSAG,SCHG)
IMPLICIT REAL*8 (A-H,O-Z)
PARAMETER(MAXCRYS = 3000, MAXSYST = 5)
COMMON/VARIABLES/AMV(3,MAXSYST),ANV(3,MAXSYST),QG(3,3,MAXCRYS),
     +   SMATC(5,MAXSYST),DBAR(5),SBAR(5),NSYST,NCRYS,
     +   TGAMI(MAXSYST,MAXSYST),SALPHT(MAXSYST,MAXCRYS),
     +   PAVINV(5,5),WBAR(3,3),SSTAR(5,MAXCRYS),
     +   D(5,MAXCRYS),DGAMMA(MAXSYST,MAXCRYS)
COMMON/MATPLAS/GDOTO,AM,HO,R1,R2,R3,STILDE,AHARD,
     + QL,CRYSDIA,G,WIDTH
REAL*8 AUX(3,3),SCHG(5,MAXSYST,MAXCRYS)
      REAL*8 TGAM(MAXSYST,MAXSYST)
REAL*8 DNSAG(3,MAXSYST,MAXCRYS),DBSAG(3,MAXSYST,MAXCRYS)
      PI = DACOS(-1.D0)
SQR2=DSQRT(2.D0)
SQR3=DSQRT(3.D0)


C  OBTAIN SLIP SYSTEM INFORMATION

OPEN(UNIT=11,FILE='epsvar.dat',STATUS = 'OLD')
READ(11,*)
READ(11,*)  NSYST !total # of available systems
READ(11,*)
DO 10 I = 1,NSYST
READ(11,*)
READ(11,*)(ANV(J,I),J=1,3),(AMV(J,I),J=1,3) !read info for slip systems
10 CONTINUE
DO 20 IS = 1,NSYST


C    COMPUTE THE SCHMID TENSOR IN CRYSTAL COORDS (AS A 5-VECTOR)

   SMATC(1,IS)=(ANV(2,IS)*AMV(2,IS)-
     +              ANV(1,IS)*AMV(1,IS))/SQR2
   SMATC(2,IS)=ANV(3,IS)*AMV(3,IS)*
     +        SQR3/SQR2
   SMATC(3,IS)=(ANV(2,IS)*AMV(3,IS)+
```

```
     +         ANV(3,IS)*AMV(2,IS))/SQR2
   SMATC(4,IS)=(ANV(1,IS)*AMV(3,IS)+
     +         ANV(3,IS)*AMV(1,IS))/SQR2
   SMATC(5,IS)=(ANV(1,IS)*AMV(2,IS)+
     +         ANV(2,IS)*AMV(1,IS))/SQR2
       WRITE(*,*)'OUTPUT FROM SUBR. INITIAL: LOCAL SCHMID',IS
WRITE(*,2) (SMATC(I,IS),I=1,5)
20 CONTINUE


C    GET THE TENSOR TGAM(NSYST,NSYST) AND ITS INVERSE 'TGAMI'
C    WHICH DO NOT DEPEND ON THE FRAME AND ARE USED IN
C    SUBROUTINE 'SOLVCRYS'


   DO 40 IS=1,NSYST
      DO 40 JS=1,NSYST
      TGAM(IS,JS)=0.D0
      DO 50 K=1,5
      TGAM(IS,JS)=TGAM(IS,JS)+SMATC(K,IS)*SMATC(K,JS)
50 CONTINUE
40      CONTINUE
WRITE(*,*)'OUTPUT FROM SUBR. INITIAL: TGAM'
      DO 1001 I=1,NSYST
      WRITE(*,2) (TGAM(I,J),J=1,NSYST)
1001      CONTINUE
CALL MDET(TGAM,DET)
WRITE(*,*)'DETERMINANT OF TGAM IS:',DET
CALL MATINV(TGAM,NSYST,MAXSYST,TGAMI)
WRITE(*,*)'OUTPUT FROM SUBR. INITIAL: TGAMI'
      DO 1002 I=1,NSYST
      WRITE(*,2) (TGAMI(I,J),J=1,NSYST)
1002      CONTINUE


C 1. READ EULER ANGLES FOR EACH N CRYSTALS
C 2. CALCULATE THE ROTATION MATRIX [QG] FOR EACH CRYSTAL
C 3. CALCULATE THE SCHMID TENSOR IN THE GLOBAL COORDINATE SYSTEM (SCHG) USING
C SUBROUTINE SCHMAC
```

```fortran
      OPEN(UNIT=12,FILE='euler8untex.dat',STATUS='OLD')
      READ(12,*)
      READ(12,*) NCRYS
      READ(12,*)
      READ(12,*)
      DO 60 ICRYS = 1,NCRYS


C READ EULER ANGLES FOR EACH CRYSTAL


      READ(12,*)TH,PHI,OM
      TH  = TH*PI/180.D0
      PHI = PHI*PI/180.D0
      OM  = OM*PI/180.D0


C CALCULATE THE ROTATION MATRIX [QG] FOR EACH CRYSTAL


      CALL ROTMAT(TH,PHI,OM,AUX)


C STORE [AUX] FOR EACH CRYSTAL IN [QG] FOR FUTURE USE


      DO 70 I=1,3
      DO 70 J=1,3
       QG(I,J,ICRYS) = AUX(I,J)
70        CONTINUE


C INPUT CONSTANT CRSS


             SALPHT(1,ICRYS) = R1
             SALPHT(2,ICRYS) = R2
             SALPHT(3,ICRYS) = R3 !constant CRSS for Nylon6 trial
60 CONTINUE !done for all crystals
WRITE(*,*)'OUTPUT FROM SUBR. INITIAL: QG FOR ICRYS=1'
      DO 1003 I=1,3
       WRITE(*,2) (QG(I,J,1),J=1,3)
1003       CONTINUE
```

```fortran
      WRITE(*,*)'OUTPUT FROM SUBR. INITIAL: SALPHT(IS,1)'
          DO 1004 IS=1,NSYST
           WRITE(*,2) SALPHT(IS,1)
1004          CONTINUE


C CALCULATE SCHMID TENSOR IN GLOBAL AXES (SCHG)


      CALL SCHMAC(DNSAG,DBSAG,SCHG)


      WRITE(*,*)'EVEN MORE OUTPUT FROM SUBR. INITIAL'
      DO 1005 IS=1,NSYST
      WRITE(*,*)'SLIP PLANE NORMAL IN GLOBAL FOR ICRYS=1, SYST:',IS
      WRITE(*,2) (DNSAG(I,IS,1),I=1,3)
      WRITE(*,*)'SLIP DIRECTION IN GLOBAL FOR ICRYS=1, SYST:',IS
      WRITE(*,2) (DBSAG(I,IS,1),I=1,3)
      WRITE(*,*)'SCHMID TENSOR IN GLOBAL FOR ICRYS=1, SYST:',IS
      WRITE(*,2) (SCHG(I,IS,1),I=1,5)
1005 CONTINUE
2 FORMAT(5(2X,F10.6))
      RETURN
      END


C SCHMAC


          SUBROUTINE SCHMAC(DNSAG,DBSAG,SCHG)
          IMPLICIT REAL*8(A-H,O-Z)
      PARAMETER(MAXCRYS = 3000, MAXSYST = 5)
      COMMON/VARIABLES/AMV(3,MAXSYST),ANV(3,MAXSYST),QG(3,3,MAXCRYS),
          +   SMATC(5,MAXSYST),DBAR(5),SBAR(5),NSYST,NCRYS,
          +   TGAMI(MAXSYST,MAXSYST),SALPHT(MAXSYST,MAXCRYS),
          +   PAVINV(5,5),WBAR(3,3),SSTAR(5,MAXCRYS),
          +   D(5,MAXCRYS),DGAMMA(MAXSYST,MAXCRYS)
      COMMON/MATPLAS/GDOTO,AM,HO,R1,R2,R3,STILDE,AHARD,
          +   QL,CRYSDIA,G,WIDTH
      REAL*8  DNSA(3,MAXSYST),DBSA(3,MAXSYST),A(3,3),SCH(5,MAXSYST)
      REAL*8 DNSAG(3,MAXSYST,MAXCRYS),DBSAG(3,MAXSYST,MAXCRYS)
```

```fortran
      REAL*8 SCHG(5,MAXSYST,MAXCRYS)


C GET ANV, AMV AND SCHMID TENSOR IN MACRO AXES


      SQR2=DSQRT(2.D0)
      SQR3=DSQRT(3.D0)
      DO 10 ICRYS=1,NCRYS
         DO 15 I=1,3
         DO 15 J=1,3
15          A(I,J)=QG(I,J,ICRYS) !rotation matrix for each crystal
      DO 20 IS=1,NSYST
               DO 30 I=1,5
            SCH(I,IS) = 0.D0
30          CONTINUE
             DO 170 J=1,3
                  DNSA(J,IS)=0.D0
                  DBSA(J,IS)=0.D0
                  DO 180 K=1,3
                    DNSA(J,IS)=DNSA(J,IS)+A(J,K)*ANV(K,IS)
                    DBSA(J,IS)=DBSA(J,IS)+A(J,K)*AMV(K,IS)
180               CONTINUE
170          CONTINUE
       SCH(1,IS)=(DNSA(2,IS)*DBSA(2,IS)-DNSA(1,IS)*DBSA(1,IS))/SQR2
      SCH(2,IS)=DNSA(3,IS)*DBSA(3,IS)*SQR3/SQR2
      SCH(3,IS)=(DNSA(2,IS)*DBSA(3,IS)+DNSA(3,IS)*DBSA(2,IS))/SQR2
      SCH(4,IS)=(DNSA(1,IS)*DBSA(3,IS)+DNSA(3,IS)*DBSA(1,IS))/SQR2
      SCH(5,IS)=(DNSA(1,IS)*DBSA(2,IS)+DNSA(2,IS)*DBSA(1,IS))/SQR2
                DO 25 I=1,5
                   SCHG(I,IS,ICRYS)=SCH(I,IS) !assigns a 5-vector to each system of
                      !each crystal, in global coords
25 CONTINUE
                DO 26 I=1,3
      DNSAG(I,IS,ICRYS)=DNSA(I,IS) !normals in global coords
      DBSAG(I,IS,ICRYS)=DBSA(I,IS) !slip directions in global coords
26 CONTINUE
20 CONTINUE !done for all available systems
```

```
10 CONTINUE !done for all crystals

RETURN

END


C ORIENT


SUBROUTINE ORIENT(DTIME,T,A)

IMPLICIT REAL*8(A-H,O-Z)

PARAMETER(MAXCRYS = 3000, MAXSYST = 5)

COMMON/VARIABLES/AMV(3,MAXSYST),ANV(3,MAXSYST),QG(3,3,MAXCRYS),

     +   SMATC(5,MAXSYST),DBAR(5),SBAR(5),NSYST,NCRYS,

     +   TGAMI(MAXSYST,MAXSYST),SALPHT(MAXSYST,MAXCRYS),

     +   PAVINV(5,5),WBAR(3,3),SSTAR(5,MAXCRYS),

     +   D(5,MAXCRYS),DGAMMA(MAXSYST,MAXCRYS)


COMMON/MATPLAS/GDOTO,AM,HO,R1,R2,R3,STILDE,AHARD,

     +   QL,CRYSDIA,G,WIDTH

       REAL*8 A(3,3),T(3,3),C(3,3),TH2(3,3),V(3),VBAR(3),TH(3,3)

REAL*8 ROT(3,3),ANEW(3,3)


C T IS THE DISTORSION TENSOR, WE FIRST TAKE THE SKEW SYMMETRIC PART OF IT, C, AND

C BUILD THE ORTHOGONAL ROTATION TENSOR BASED ON RODRIGUEZ FORMULA.


PI=4.D0*DATAN(1.D0)

SQR2=DSQRT(2.D0)

SQR3=DSQRT(3.D0)

DO 10 I=1,3

DO 10 J=1,3

   C(I,J)=(WBAR(I,J)-(T(I,J)-T(J,I))/2.D0)*DTIME

10 CONTINUE

V(1)=C(3,2)

V(2)=C(1,3)

V(3)=C(2,1)

SNORM=DSQRT(V(1)*V(1)+V(2)*V(2)+V(3)*V(3))

SNORM1=DTAN(SNORM/2.D0)
```

```fortran
      IF(SNORM.GT.1.D-08) GO TO 97
      SNORM=1.D0
97    DO 20 I=1,3
         VBAR(I)=SNORM1*V(I)/SNORM
20    CONTINUE
      SNORM=VBAR(1)*VBAR(1)+VBAR(2)*VBAR(2)+VBAR(3)*VBAR(3)
      TH(3,2)=VBAR(1)
      TH(1,3)=VBAR(2)
      TH(2,1)=VBAR(3)
      TH(2,3)=-VBAR(1)
      TH(3,1)=-VBAR(2)
      TH(1,2)=-VBAR(3)
      DO 40 I=1,3
40       TH(I,I)=0.D0
      DO 30 I=1,3
      DO 30 J=1,3
         TH2(I,J)=0.D0
         DO 50 K=1,3
            TH2(I,J)=TH2(I,J)+TH(I,K)*TH(K,J)
50       CONTINUE
30    CONTINUE
      DO 60 I=1,3
      DO 60 J=1,3
      ROT(I,J)=(I/J)*(J/I)+2.D0*(TH(I,J)+TH2(I,J))/(1.D0+SNORM)
60    CONTINUE
      DO 70 I=1,3
      DO 70 J=1,3
         ANEW(I,J)=0.D0
         DO 80 K=1,3
            ANEW(I,J)=ANEW(I,J)+ROT(I,K)*A(K,J)
80       CONTINUE
70    CONTINUE
      DO 90 I=1,3
      DO 90 J=1,3
         A(I,J)=ANEW(I,J)
90    CONTINUE
```

```
RETURN

END


C FUNC


SUBROUTINE FUNC(DTIME,LD,TR1,TR2,STRAINRATE,R,SCHG,TEST2)


C GIVEN A RATIO R=L11/L22 THIS SUBROUTINE RETURNS

C TEST2=DABS(SDEV(TR1,TR1)-SDEV(TR2,TR2))


IMPLICIT REAL*8 (A-H,O-Z)

PARAMETER(MAXCRYS = 3000, MAXSYST = 5)

COMMON/VARIABLES/AMV(3,MAXSYST),ANV(3,MAXSYST),QG(3,3,MAXCRYS),

     +   SMATC(5,MAXSYST),DBAR(5),SBAR(5),NSYST,NCRYS,

     +   TGAMI(MAXSYST,MAXSYST),SALPHT(MAXSYST,MAXCRYS),

     +   PAVINV(5,5),WBAR(3,3),SSTAR(5,MAXCRYS),

     +   D(5,MAXCRYS),DGAMMA(MAXSYST,MAXCRYS)

COMMON/MATPLAS/GDOTO,AM,HO,R1,R2,R3,STILDE,AHARD,

     +   QL,CRYSDIA,G,WIDTH

      INTEGER LD,TR1,TR2

REAL*8  LBARDOT(3,3),DB3(3,3),PAV(5,5)

      REAL*8 SSTAV(5),SDEV(3,3),SCHG(5,MAXSYST,MAXCRYS)

CALL ZEROM(LBARDOT,3)

LBARDOT(LD,LD)=STRAINRATE

LBARDOT(TR1,TR1)=-STRAINRATE/(1+R)

LBARDOT(TR2,TR2)=-(R*STRAINRATE)/(1+R)

DO 10 I=1,3

DO 10 J=1,3

        DB3(I,J)=(LBARDOT(I,J)+LBARDOT(J,I))/2.DO

        WBAR(I,J)=(LBARDOT(I,J)-LBARDOT(J,I))/2.DO

10 CONTINUE

CALL MATVEC(DB3,DBAR)

CALL SOLVCRYS(DTIME,SCHG,SSTAV,PAV)

CALL MULTMV(PAVINV,SSTAV,SBAR,5)

CALL VECMAT(SBAR,SDEV)

TEST2=DABS(SDEV(TR1,TR1)-SDEV(TR2,TR2))
```

127

```
2 FORMAT(5(2X,F10.6))
RETURN
END


C MNBRAK


SUBROUTINE MNBRAK(DTIME,LD,TR1,TR2,STRAINRATE,SCHG,
    + AX,BX,CX)


C GIVEN DISTINCT INITIAL POINTS FOR R (AX AND BX) THIS SUBROUTINE
C BRACKETS THE MINIMUM OF TEST2 AND RETURNS NEW POINTS AX, BX, AND CX.
C ALSO, THE VALUE OF TEST2 AT THESE POINTS FA, FB, AND FC.


IMPLICIT REAL*8 (A-H,O-Z)
PARAMETER(MAXCRYS = 3000, MAXSYST = 5)
PARAMETER(GOLD=1.618034D0,GLIMIT=100.D0,TINY=1.E-20)
COMMON/VARIABLES/AMV(3,MAXSYST),ANV(3,MAXSYST),QG(3,3,MAXCRYS),
    + SMATC(5,MAXSYST),DBAR(5),SBAR(5),NSYST,NCRYS,
    + TGAMI(MAXSYST,MAXSYST),SALPHT(MAXSYST,MAXCRYS),
    + PAVINV(5,5),WBAR(3,3),SSTAR(5,MAXCRYS),
    + D(5,MAXCRYS),DGAMMA(MAXSYST,MAXCRYS)
COMMON/MATPLAS/GDOTO,AM,HO,R1,R2,R3,STILDE,AHARD,
    + QL,CRYSDIA,G,WIDTH
    INTEGER LD,TR1,TR2
    REAL*8 SCHG(5,MAXSYST,MAXCRYS)
AX=0.D0
BX=1.D0
CALL FUNC(DTIME,LD,TR1,TR2,STRAINRATE,AX,SCHG,FA)
CALL FUNC(DTIME,LD,TR1,TR2,STRAINRATE,BX,SCHG,FB)
IF(FB.GT.FA)THEN
DUM=AX
AX=BX
BX=DUM
DUM=FB
FB=FA
FA=DUM
```

```
ENDIF

CX=BX+GOLD*(BX-AX)

CALL FUNC(DTIME,LD,TR1,TR2,STRAINRATE,CX,SCHG,FC)

1 IF(FB.GE.FC)THEN

R=(BX-AX)*(FB-FC)

Q=(BX-CX)*(FB-FA)

U=BX-((BX-CX)*Q-(BX-AX)*R)/

     + (2.DO*SIGN(MAX(DABS(Q-R),TINY),Q-R))

       ULIM=BX+GLIMIT*(CX-BX)

       IF((BX-U)*(U-CX).GT.0.DO)THEN

       CALL FUNC(DTIME,LD,TR1,TR2,STRAINRATE,U,SCHG,FU)

       IF(FU.LT.FC)THEN

       AX=BX

       FA=FB

       BX=U

       FB=FU

       RETURN

ELSE IF(FU.GT.FB)THEN

CX=U

FC=FU

RETURN

ENDIF

U=CX+GOLD*(CX-BX)

CALL FUNC(DTIME,LD,TR1,TR2,STRAINRATE,U,SCHG,FU)

ELSE IF((CX-U)*(U-ULIM).GT.0.DO)THEN

CALL FUNC(DTIME,LD,TR1,TR2,STRAINRATE,U,SCHG,FU)

IF(FU.LT.FC)THEN

BX=CX

CX=U

U=CX+GOLD*(CX-BX)

FB=FC

FC=FU

CALL FUNC(DTIME,LD,TR1,TR2,STRAINRATE,U,SCHG,FU)

ENDIF

ELSE IF((U-ULIM)*(ULIM-CX).GE.0.DO)THEN

U=ULIM
```

```
CALL FUNC(DTIME,LD,TR1,TR2,STRAINRATE,U,SCHG,FU)
ELSE
U=CX+GOLD*(CX-BX)
CALL FUNC(DTIME,LD,TR1,TR2,STRAINRATE,U,SCHG,FU)
ENDIF
AX=BX
BX=CX
CX=U
FA=FB
FB=FC
FC=FU

GO TO 1
ENDIF
RETURN
END


C GOLDEN


SUBROUTINE GOLDEN(DTIME,LD,TR1,TR2,STRAINRATE,SCHG,
     + AX,BX,CX,TOL,XMIN,GOLE)


C THIS SUBROUTINE PERFORMS GOLDEN SECTION SEARCH FOR THE MINIMUM OF
C FUNC, ISOLATING IT TO A FRACTIONAL PRECISION OF ABOUT TOL

IMPLICIT REAL*8 (A-H,O-Z)
PARAMETER(MAXCRYS = 3000, MAXSYST = 5)
PARAMETER(R=0.61803399D0,C=1.D0-R)
COMMON/VARIABLES/AMV(3,MAXSYST),ANV(3,MAXSYST),QG(3,3,MAXCRYS),
     + SMATC(5,MAXSYST),DBAR(5),SBAR(5),NSYST,NCRYS,
     + TGAMI(MAXSYST,MAXSYST),SALPHT(MAXSYST,MAXCRYS),
     + PAVINV(5,5),WBAR(3,3),SSTAR(5,MAXCRYS),
     + D(5,MAXCRYS),DGAMMA(MAXSYST,MAXCRYS)


COMMON/MATPLAS/GDOTO,AM,HO,R1,R2,R3,STILDE,AHARD,
     + QL,CRYSDIA,G,WIDTH
```

```fortran
      INTEGER LD,TR1,TR2
      REAL*8 SCHG(5,MAXSYST,MAXCRYS)
      ITRIAL=0
      X0=AX
      X3=CX
      IF(DABS(CX-BX).GT.DABS(BX-AX))THEN
      X1=BX
      X2=BX+C*(CX-BX)
      ELSE
     X2=BX
      X1=BX-C*(BX-AX)
      END IF
      CALL FUNC(DTIME,LD,TR1,TR2,STRAINRATE,X1,SCHG,F1)
      CALL FUNC(DTIME,LD,TR1,TR2,STRAINRATE,X2,SCHG,F2)
1 IF(DABS(X3-X0).GT.TOL*(DABS(X1)+DABS(X2)))THEN
IF(F2.LT.F1)THEN
X0=X1
X1=X2
X2=R*X1+C*X3
F1=F2
CALL FUNC(DTIME,LD,TR1,TR2,STRAINRATE,X2,SCHG,F2)
ELSE
X3=X2
X2=X1
X1=R*X2+C*X0
F2=F1
CALL FUNC(DTIME,LD,TR1,TR2,STRAINRATE,X1,SCHG,F1)
ENDIF
ITRIAL=ITRIAL+1
GOTO 1
ENDIF
WRITE(*,*)'# OF TRIALS IS:',ITRIAL
IF(F1.LT.F2)THEN
XMIN=X1
GOLE=F1
ELSE
```

```fortran
      XMIN=X2
      GOLE=F2
      END IF
      RETURN
      END


C UTILITIES SUBROUTINES:


C MULTMV


      SUBROUTINE MULTMV(A,V,VNEW,N)
      IMPLICIT REAL*8(A-H,O-Z)
      REAL*8 A(N,N),V(N),VNEW(N)


C THIS SUBROUTINE TRANSFORMS VECTOR V TO VECTOR VNEW
C BY MULTIPLYING BY MATRIX A.


      DO 10 I=1,N
      VNEW(I)=0.DO
      DO 15 J=1,N
15    VNEW(I)=VNEW(I)+A(I,J)*V(J)
10    CONTINUE
      RETURN
      END


C MATVEC


      SUBROUTINE MATVEC(A,V)
      IMPLICIT REAL*8(A-H,O-Z)
      REAL*8 A(3,3),V(5)


C TRANSFORMS A 3X3 SYMM. TRACELESS MATRIX TO A 5-VECTOR


      SQR2=DSQRT(2.DO)
      SQR3=DSQRT(3.DO)
      V(1)=(A(2,2)-A(1,1))/SQR2
```

```fortran
      V(2)=A(3,3)*SQR3/SQR2
      V(3)=A(2,3)*SQR2
      V(4)=A(1,3)*SQR2
      V(5)=A(1,2)*SQR2
      RETURN
      END


C VECMAT


      SUBROUTINE VECMAT(V,A)
      IMPLICIT REAL*8(A-H,O-Z)
      REAL*8 A(3,3),V(5)


C TRANSFORMS A 5-VECTOR TO A 3X3 SYMM. TRACELESS MATRIX


      SQR2=DSQRT(2.DO)
      SQR3=DSQRT(3.DO)
      A(3,3)=V(2)*SQR2/SQR3
      A(2,2)=(V(1)/SQR2)-V(2)/(SQR2*SQR3)
      A(1,1)=-A(2,2)-A(3,3)
      A(1,2)=V(5)/SQR2
      A(2,1)=A(1,2)
      A(1,3)=V(4)/SQR2
      A(3,1)=A(1,3)
      A(2,3)=V(3)/SQR2
      A(3,2)=A(2,3)
      RETURN
      END


C MATMUL


C THIS SUBROUTINE MULTIPLIES MATRIX A BY MATRIX B TO GIVE MATRIX C

SUBROUTINE MATMUL(A,IA,B,IB,C,IC,L,M,K)
IMPLICIT REAL*8(A-H,O-Z)
REAL*8 A(IA,IA),B(IB,IB),C(IC,IC)
```

```fortran
      DO 10 I=1,L
      DO 10 J=1,K
       C(I,J)=0.D0
       DO 20 II=1,M
20     C(I,J)=C(I,J)+A(I,II)*B(II,J)
10       CONTINUE
      RETURN
      END


C ONEM


C THIS SUBROUTINE STORES THE 3X3 IDENTITY MATRIX IN MATRIX [A]


      SUBROUTINE ONEM(A)
      REAL*8 A(3,3)
      DO 1 I = 1,3
      DO 1 J = 1,3
          IF (I.EQ.J) THEN
              A(I,J) = 1.D0
          ELSE
              A(I,J) = 0.D0
          END IF
       1 CONTINUE
      RETURN
      END


C ROTMAT


      SUBROUTINE ROTMAT(TH,PHI,OM,Q)
      IMPLICIT REAL*8(A-H,O-Z)
      REAL*8 Q(3,3)


C INITIALIZE


          CALL ONEM(Q)
          STH = DSIN(TH)
```

```
       CTH = DCOS(TH)

       SPH = DSIN(PHI)

       CPH = DCOS(PHI)

       SOM = DSIN(OM)

       COM = DCOS(OM)

       Q(1,1) = CPH*COM-SPH*SOM*CTH

       Q(1,2) = SPH*COM+CPH*SOM*CTH

       Q(1,3) = SOM*STH

       Q(2,1) = -CPH*SOM-SPH*COM*CTH

       Q(2,2) = -SPH*SOM+CPH*COM*CTH

       Q(2,3) =   COM*STH

       Q(3,1) = SPH*STH

       Q(3,2) = -CPH*STH

       Q(3,3) = CTH

RETURN

END


C EULANG


SUBROUTINE EULANG(Q,N,TH,PHI,OM,ICRYS)

IMPLICIT REAL*8(A-H,O-Z)

REAL*8 Q(N,N)

PI = 4.D0*DATAN(1.D0)

ICHK=0

IF(DABS(Q(3,3))-1.0.GT.1.0D-6)THEN !why the 1.0?

         WRITE(9,*)'Q',((Q(I,J),J=1,3),I=1,3)

PAUSE 'Q(3,3) > 1.0'

ENDIF

DO 10 I = 1,3

DO 10 J = 1,3

10   IF(DABS(Q(I,J)).LT.1.0D-6)Q(I,J)=0.D0

IF(DABS(DABS(Q(3,3))-1.0).LT.1.0D-6)THEN !why the 1.0?

         CALL CHECK1(Q,3,TH,PHI,OM,ICHK)

  IF(ICHK.NE.1)GO TO 20

  RETURN

ENDIF
```

```fortran
TH = DACOS(Q(3,3))
STH = DSIN(TH)
OM = DATAN2(Q(1,3)/STH,Q(2,3)/STH)
PHI = DATAN2(Q(3,1)/STH,-Q(3,2)/STH)
CALL CHECK(Q,3,TH,PHI,OM,ICHK)
IF(ICHK.EQ.1)RETURN
TH = 2.D0*PI-TH
STH = DSIN(TH)
OM = DATAN2(Q(1,3)/STH,Q(2,3)/STH)
PHI = DATAN2(Q(3,1)/STH,-Q(3,2)/STH)
CALL CHECK(Q,3,TH,PHI,OM,ICHK)
20 IF(ICHK.NE.1)THEN
   WRITE(9,*)'ICRYS = ',ICRYS
   WRITE(9,*)'Q',((Q(J,K),K=1,3),J=1,3)
            PAUSE 'FAILED TO FIND EULER ANGLES'
ENDIF
RETURN
END


C CHECK1


        SUBROUTINE CHECK1(Q,N,TH,PHI,OM,ICHK)
        IMPLICIT REAL*8(A-H,O-Z)
        REAL*8 Q(N,N)
TOL=1.0D-3
Q(3,3) = 1.0*Q(3,3)/DABS(Q(3,3)
TH = DACOS(Q(3,3))
IF(DABS(Q(1,3)).GT.TOL)RETURN
IF(DABS(Q(2,3)).GT.TOL)RETURN
IF(DABS(Q(3,1)).GT.TOL)RETURN
IF(DABS(Q(3,2)).GT.TOL)RETURN
IF(Q(3,3).EQ.1.0)THEN !why the 1.0?
   IF(DABS(Q(1,1)-Q(2,2)).GT.TOL)RETURN
   IF(DABS(Q(1,2)+Q(2,1)).GT.TOL)RETURN
ELSE
   IF(DABS(Q(1,1)+Q(2,2)).GT.TOL)RETURN
```

```
      IF(DABS(Q(1,2)-Q(2,1)).GT.TOL)RETURN
ENDIF
PHI = DATAN2(Q(1,2),Q(1,1))
OM = 0.DO
ICHK = 1
RETURN
END


C CHECK


      SUBROUTINE CHECK(Q,N,TH,PHI,OM,ICHK)
      IMPLICIT REAL*8(A-H,O-Z)
      REAL*8 Q(N,N)
TOL=1.0D-3
A = DCOS(PHI)*DCOS(OM)-DSIN(PHI)*DSIN(OM)*DCOS(TH)
B = -DSIN(OM)*DCOS(PHI)-DCOS(OM)*DSIN(PHI)*DCOS(TH)
C = DCOS(OM)*DSIN(PHI)+DSIN(OM)*DCOS(PHI)*DCOS(TH)
D = -DSIN(PHI)*DSIN(OM)+DCOS(PHI)*DCOS(OM)*DCOS(TH)
      IF(DABS(A-Q(1,1)).LT.TOL.AND.DABS(B-Q(2,1)).LT.TOL.
     +    AND.DABS(C-Q(1,2)).LT.TOL.AND.DABS(D-Q(2,2)).LT.TOL)ICHK=1
RETURN
END


C MATINV


      SUBROUTINE MATINV(A,N,NP,Y)
IMPLICIT REAL*8 (A-H,O-Z)
      DIMENSION A(NP,NP),Y(NP,NP),INDX(NP)


C Set up the identity matrix


DO 12 I=1,N
DO 11 J=1,N
Y(I,J)=0.DO
11 CONTINUE
Y(I,I)=1.DO
```

```fortran
12 CONTINUE

C Decompose the matrix just once (LU Decomposition)

CALL LUDCMP(A,N,NP,INDX,D)

C Find the inverse by columns. It is necessary to recognize
C that FORTRAN stores two dimensional matrices by column, so
C so that Y(1,J) is the address of the Jth column of Y.

DO 13 J=1,N
    CALL LUBKSB(A,N,NP,INDX,Y(1,J))
13 CONTINUE
RETURN
END


C LUDCMP


        SUBROUTINE LUDCMP(A,N,NP,INDX,D)
IMPLICIT REAL*8 (A-H,O-Z)
PARAMETER (NMAX=100,TINY=1.0E-20)
DIMENSION A(NP,NP),INDX(N),VV(NMAX)
D=1.D0
DO 12 I=1,N
        AAMAX=0.D0
        DO 11 J=1,N
          IF (DABS(A(I,J)).GT.AAMAX) AAMAX=DABS(A(I,J))
11      CONTINUE
        IF (AAMAX.EQ.0.D0) PAUSE 'Singular matrix.'
        VV(I)=1.D0/AAMAX
12 CONTINUE
DO 19 J=1,N
        IF(J.GT.1)THEN !where did that come from?
          DO 14 I=1,J-1
            SUM=A(I,J)
            IF(I.GT.1)THEN !where did that come from?
```

138

```
          DO 13 K=1,I-1
            SUM=SUM-A(I,K)*A(K,J)
13          CONTINUE
          A(I,J)=SUM
        ENDIF !where did that come from?
14      CONTINUE
      ENDIF !where did that come from?
      AAMAX=0.D0
      DO 16 I=J,N
        SUM=A(I,J)
        IF(J.GT.1)THEN !where did that come from?
          DO 15 K=1,J-1
            SUM=SUM-A(I,K)*A(K,J)
15          CONTINUE
          A(I,J)=SUM
        ENDIF !where did that come from?
        DUM=VV(I)*DABS(SUM)
        IF(DUM.GE.AAMAX)THEN
          IMAX=I
          AAMAX=DUM
        ENDIF
16 CONTINUE
      IF(J.NE.IMAX)THEN
        DO 17 K=1,N
          DUM=A(IMAX,K)
          A(IMAX,K)=A(J,K)
          A(J,K)=DUM
17        CONTINUE
        D=-D
        VV(IMAX)=VV(J)
      ENDIF
      INDX(J)=IMAX
      IF(A(J,J).EQ.0.D0)A(J,J)=TINY
      IF(J.NE.N)THEN !that was the other way around
        DUM=1.D0/A(J,J)
        DO 18 I=J+1,N
```

```fortran
          A(I,J)=A(I,J)*DUM
18        CONTINUE
        ENDIF
19 CONTINUE
RETURN
END


C LUBKSB


        SUBROUTINE LUBKSB(A,N,NP,INDX,B)
IMPLICIT REAL*8 (A-H,O-Z)
DIMENSION A(NP,NP),INDX(N),B(N)
        II=0
        DO 12 I=1,N
         LL=INDX(I)
         SUM=B(LL)
         B(LL)=B(I)
         IF (II.NE.0)THEN
           DO 11 J=II,I-1
             SUM=SUM-A(I,J)*B(J)
11         CONTINUE
         ELSE IF(SUM.NE.0.DO)THEN
           II=I
         ENDIF
         B(I)=SUM
12      CONTINUE
        DO 14 I=N,1,-1
         SUM=B(I)
         IF(I.LT.N)THEN !where did that come from
           DO 13 J=I+1,N
             SUM=SUM-A(I,J)*B(J)
13         CONTINUE
         ENDIF !where did that come from
         B(I)=SUM/A(I,I)
14      CONTINUE
        RETURN
```

```
      END


C EQUIVS


      SUBROUTINE EQUIVS(S,SB)


C THIS SUBROUTINE CALCULATES THE EQUIVALENT TENSILE STRESS SB
C CORRESPONDING TO A 3X3 STRESS MATRIX [S]


      REAL*8 S(3,3),SDEV(3,3),SDOTS,SB
      SB = 0.D0
      SDOTS = 0.D0
      CALL DEVM(S,SDEV)
      CALL DOTPM(SDEV,SDEV,SDOTS)
      SB = DSQRT(1.5D0* SDOTS)
      RETURN
      END


C DEVM


      SUBROUTINE DEVM(A,ADEV)


C THIS SUBROUTINE CALCULATES THE DEVIATORIC PART OF A 3X3 MATRIX [A]


      REAL*8 A(3,3),TRA,ADEV(3,3),IDEN(3,3)
      CALL TRACEM(A,TRA)
      CALL ONEM(IDEN)
      CALL ZEROM(ADEV,3)
      DO 1 I = 1,3
      DO 1 J = 1,3
          ADEV(I,J) = A(I,J) - (1.D0/3.D0)*TRA*IDEN(I,J)
    1 CONTINUE
      RETURN
      END


C TRACEM
```

```
SUBROUTINE TRACEM(A,TRA)


C THIS SUBROUTINE CALCULATES THE TRACE OF A 3X3 MATRIX [A] AND STORES
C THE RESULT IN THE SCALAR TRA


REAL*8 A(3,3),TRA
TRA = A(1,1) + A(2,2) + A(3,3)
RETURN
END


C DOTPM


SUBROUTINE  DOTPM(A,B,C)


C THIS SUBROUTINE CALCULATES THE SCALAR PRODUCT OF TWO
C 3 BY 3 MATRICES [A] AND [B] AND STORES THE RESULT IN THE
C SCALAR C.


REAL*8 A(3,3),B(3,3),C
C= 0.D0
DO 1 I = 1,3
DO 1 J = 1,3
    C = C + A(I,J)*B(I,J)
 1 CONTINUE
RETURN
END


C ZEROM


      SUBROUTINE ZEROM(A,N)


C THIS SUBROUTINE SETS ALL ENTRIES OF A N BY N MATRIX TO 0.D0


      REAL*8 A(N,N)
      DO 1 I=1,N
```

```fortran
      DO 1 J=1,N
          A(I,J) = 0.D0
  1 CONTINUE
RETURN
END


C MDET


SUBROUTINE MDET(A,DET)


C   THIS SUBROUTINE CALCULATES THE DETERMINANT OF A 3X3 MATRIX [A].


REAL*8  A(3,3),DET
DET = A(1,1)*A(2,2)*A(3,3)
    + + A(1,2)*A(2,3)*A(3,1)
    + + A(1,3)*A(2,1)*A(3,2)
    + - A(3,1)*A(2,2)*A(1,3)
    + - A(3,2)*A(2,3)*A(1,1)
    + - A(3,3)*A(2,1)*A(1,2)
RETURN
END
```